Charge Transfer through Chiral Organic and Peptide Nucleic Acid (PNA) Molecules

by

Amit Paul

B. Sc, Jadavpur University, Calcutta, India, 2001

M. Sc, IIT Bombay, Mumbai, India, 2003

Submitted to the Graduate Faculty of

Arts and Sciences in partial fulfillment

Of the requirements for the degree of

Doctor of Philosophy

University of Pittsburgh

2008

UNIVERSITY OF PITTSBURGH

FACULTY OF ARTS AND SCIENCES

This dissertation was presented

by

Amit Paul

It was defended on

October 1, 2008

and approved by

Dr. Shigeru Amemiya, Assistant Professor, Department of Chemistry, University of Pittsburgh

Dr. Steve Weber, Professor, Department of Chemistry, University of Pittsburgh

Dr. Catalina Achim, Associate Professor, Department of Chemistry, Carnegie Mellon University

Dr. David H. Waldeck, Professor, Department of Chemistry, University of Pittsburgh
Dissertation Director

CHARGE TRANSFER THROUGH CHIRAL ORGANIC AND PEPTIDE NUCLEIC ACID MOLECULES

Amit Paul, PhD

University of Pittsburgh, 2008

Abstract

The quest for miniaturization of electronic devices has caused a surge in research to find bottom-up alternatives for electronic circuit design and from this need, molecular electronics has emerged as a new field of study. For the development of "molecular-wire", it is very important to understand the flow of charge through molecular bridge systems that can be used to manipulate the flow of charge through these systems. Charge transfer (CT) through chiral organic molecules has been investigated by photoelectrochemistry through chiral molecular bridges. The study showed that the charge transfer through a chiral molecular bridge has a preference for circularly polarized light whose sense of rotation is either left or right. CT study through single stranded (ss) and double stranded (ds) peptide nucleic acid (PNA) films have been performed also. CT studies through PNA films show that at short distance the CT exponentially falls of with increasing distance, which is consistent with a super-exchange mediated tunneling mechanism, but at longer distance the decay is shallow, indicating that the CT follows a different mechanism called "hopping" mechanism. The experimentally determined mechanism switchover point from tunneling to hopping has been found to be in good agreement with a tight-binding model proposed earlier. Further, it has been found that CT through PNA is primarily controlled by nucleobases and CT can be manipulated by changing nucleobase or nucleobase pair sequence.

TABLE OF CONTENTS

LIST OF TABLES

LIST OF FIGURES

LIST OF SCHEMES

DEDICATION

This thesis is dedicated to my father. This work is the realization of his dream. This thesis is also dedicated to my late father in law who suddenly left us in 2007.

Acknowledgements

I wish to acknowledge an immeasurable dept of gratitude to many individuals for their support and encouragement during my graduate studies. First of all, I owe my most sincere gratitude to my supervisor, Dr. David H. Waldeck. No word will be sufficient to express my respect for him. His knowledge and commitment motivated me throughout my graduate study. Whenever I needed help, he was always there to provide it. His encouragement and critical analysis helped me to shape as a better scientist.

I am also grateful to Prof. Catalina Achim. Not only did her research group synthesize all of the PNA molecules but also her advice and guidance in these difficult years taught me how to become a better researcher. It was my great pleasure to learn synthesis in her laboratory. My deep gratitude goes to Prof. Ron Naaman. Some people come into one's life for very short period of time but change it completely. Ron did that for me. Life goes on but we cannot forget some people. Prof. Ron Naaman will hold a special position in my heart forever. I want to thank my other collaborators; Prof. Chris Schafmeister, Prof. David Beratan, Prof. Marcela Madrid and Prof. Eric Borguet. Furthermore, I want to thank my committee members Prof. Shigeru Amemiya and Prof. Steve Weber for their time and advice to complete this work.

I want to thank Paul Lund, Silvia Bezer and Dr. Gregory Bird for synthesizing the molecules for me. My special thanks go to Dr. Richard M. Watson for helping me by not only synthesizing PNA molecules but also for teaching me PNA synthesis and for working with me to solve problems. No matter how many times I called him in a given week, he was always patient and welcomed me with his helping heart.

I want to thank Dr. Jianjun Wei and Dr. Hongjun Yue, from whom I learned all the electrochemistry techniques. They were extremely patient and insightful during my learning periods. My sincere thanks go to Dr. Andrew M. Napper. I never met him personally yet he is someone special in my life. His single email helped me to solve the most important problem of my research life. I am grateful to Kathryn Davis, Yangjun Xing, Dr. Yufan He, and Dr. Emil Wierzbinski with whom I worked on the PNA project. I feel lucky to have great lab mate like Dr. Palwinder Kaur who helped me to overcome frustrating time periods of the research life. I feel lucky to have some excellent lab mates; Dr. Leela Mohan Reddy, Subhasis Chakrabarti, Lei Wang, Mingyang Wu, Daniel Lamont, Matt Kofke, Alexander Clemmens, and Dr. Min Liu.

I want to express my appreciation to the machine shop staff and the electronic shop staff for their assistance on various occasions during the last five years.

I owe my loving thanks to my parents for their constant support and encouragement in all my professional endeavors. Especially, I would like to thank my father, as he is the key inspiration of my life. He was among those millions of persons who suffered due to the political turmoil in the Indian subcontinent during the 1970s and so, was unable to complete his education. Still he did not stop dreaming and always hoped his son would get the education that he could not. This thesis is essentially an effort to fulfill his dream. I would like to thank my late father-in-law who passed away in 2007. It was unfortunate that I was not able to stay with him during his last breaths on this earth. I hope this thesis will make his soul happy and I ask his blessings from the heaven. I wish to express my deepest gratitude to my better half, Kakoli for her unconditional love and support through

all these years. Finally I want to thank my sister, mother-in-law, other family members and all friends for their love and support.

Chapter 1: Introduction

1.1 An Overview

Electron transfer (ET) or charge transfer (CT) plays a key role for chemical and biological systems. For the past 50 years, people have been conducting research on CT, in both homogeneous and heterogeneous systems. Within a unifying framework of donor-bridge-acceptor charge transfer it is well known that the spacer between the electron donor and acceptor plays a key role in determining the electron transfer reaction rate. For short molecules it is well accepted that CT falls off exponentially with increasing distance between donor and acceptor; commonly expressed as:

$$k = k_0 \exp(-\beta d) \qquad (1\text{-}1)$$

where d is the distance between electron donor and acceptor, and β is a decay parameter. At short distances, β has a value ranging from about 0.6 to 1.5 $Å^{-1}$. This exponential decay with distance corresponds to an "electron tunneling" (nonresonant) charge transfer mechanism. Interestingly at longer distance it has been found that the rate constant scales as 1/d for many different systems such as conjugated organic molecules, DNA, peptide etc. This length dependence corresponds to one-dimensional diffusion and is describe through a "hopping" mechanism. A transition from the "tunneling" mechanism to a "hopping" mechanism has been found for different systems and theoretical work is also available to understand this switch over. For the development of "molecular wires", it is very important to understand how the flow of charge through a molecular bridge changes from short distance to long distance.

Self-assembly techniques have been widely used to control the molecular bridge length and regulate the separation between a redox species and an electrode. Peptide nucleic acid or organic molecules can covalently attach on gold surfaces in solution using a gold-sulfur covalent bond and spontaneously form a self-assembled monolayer (SAM) film. A redox species can be covalently attached at the other end of the molecule. By applying a voltage on a SAM modified gold electrode, the gold electrode can acts as an electron donor or acceptor and ET can be monitored between the gold and the redox probe.

This thesis investigates electron transfer through self-assembled molecular films of peptide nucleic acid (PNA) and chiral organic molecules on metal electrodes. In this chapter, I provide a brief overreview of Peptide Nucleic Acid (PNA), self-assembled monolayer (SAM) films, electron transfer theory, chirality effects on charge transfer, and the hopping mechanism of charge transfer.

1.2 Introduction to Peptide Nucleic Acid (PNA)

Peptide Nucleic Acids (PNAs) are analogues of Deoxyribonucleic Acid (DNA) in which a 2-aminoethyl-glycine based pseudo-peptide backbone replaces the phosphodiester backbone (Figure 1.1).[1-4] Similar to DNA, PNA contains the nucleobases, guanine (G), cytosine (C), adenine (A), and thymine (T) (Figure 1.1). PNA oligomers are

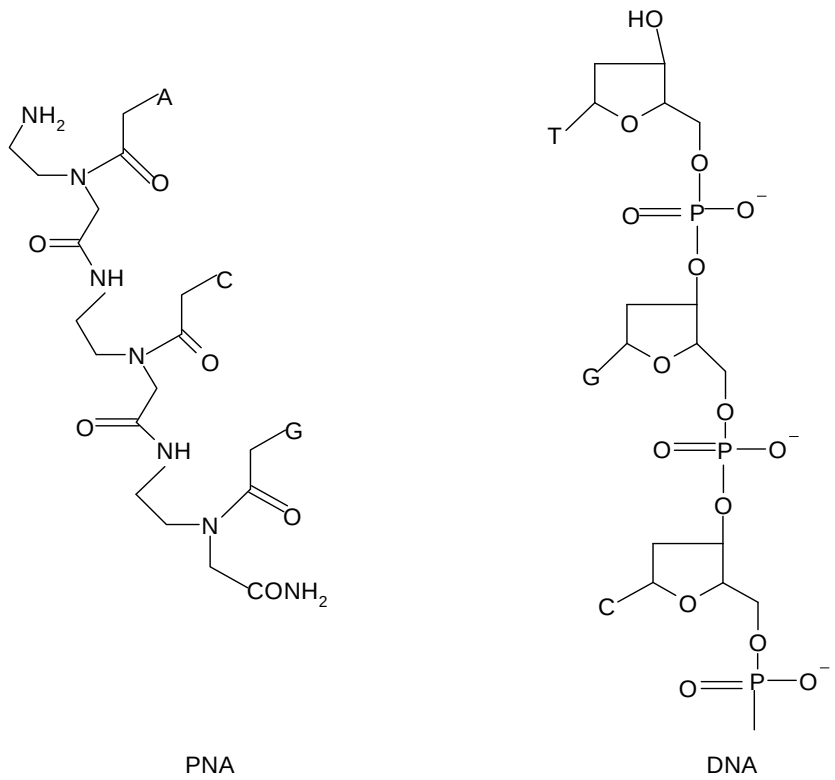

Figure 1.1 Chemical structure of PNA (left) and DNA (right).

able to form stable duplex structures with Watson-Crick base pairing between two complementary strands.[5] PNA not only forms duplexes with itself but also with complementary sequences of DNA or ribonucleic acid (RNA) oligomers. PNA's backbone is neutral and hence the solubility of PNA is poor in water. Although PNAs solubility is poor, the introduction of a polar group, such as lysine, can improve its solubility significantly. PNA has many biological applications and is used as a molecular tool in molecular biology and biotechnology.[6,7] PNA is the lead compound for the development of gene-targeted drugs applying antigene or antisense strategy.[8] PNA can be used for diagnostic purposes, development of biosensors[9] and the improvement of supramolecular constructs.[10]

The neutral character of the PNA backbone is an important feature. For this reason, the binding between complementary PNA and DNA strands is stronger than that between complementary strands of DNA, at low ionic strength. This increased stability is attributed to the lack of charge repulsion. Interestingly, not only the affinity is higher for PNA/ DNA duplexes, but the specificity is also higher. PNA/ PNA duplexes adopts a helical structure termed P-type, which has a large pitch with 18 bases/ turn, a diameter of 28 Å, and a 3.2-3.4 Å rise/ base pair.[11-13] Because PNA is made of an achiral backbone unmodified PNA does not have a preferred handedness, but a preferred handedness can be induced in PNA by incorporating a chiral group such as lysine or cysteine at the N-terminal ends.[14]

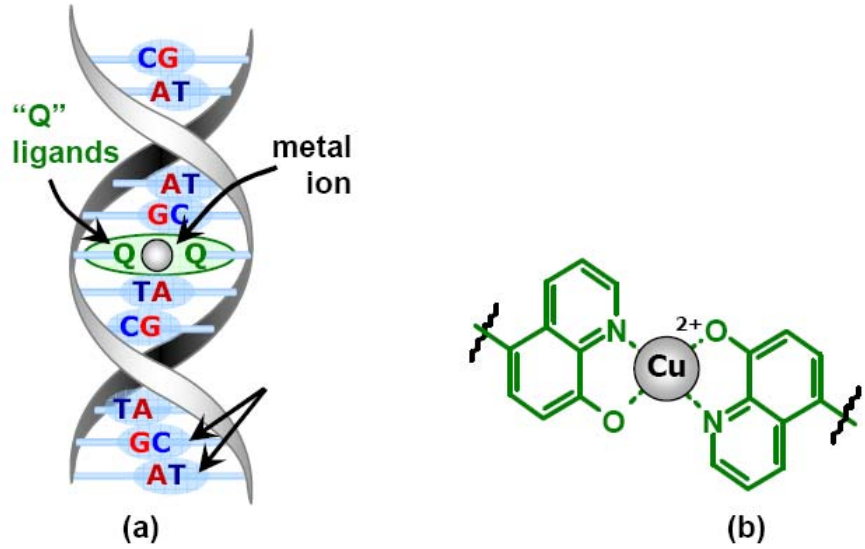

Figure 1.2 (a) Cartoon representation of a PNA duplex that includes metal mediated alternative base pairs. (b) Square planar complex formed between Q ligands and Cu^{+2}. This figure is taken from reference 18.

Another important feature of PNA is that metal ions can be incorporated into the core of its helix.[15-18] In Figure 1.2, a representative ligand-modified PNA duplex structure is shown. Such modified PNAs can be used for incorporation of different metal ions such

as Cu^{+2}, Ni^{+2}, Co^{+2}. Metal-containing PNAs could have major applications in the field of molecular electronics and nanotechnology towards which this PhD is targeted.

1.3 A Brief Review of Self-Assembled Monolayers (SAMs)

A self-assembled monolayer (SAM) is a single molecular layer adsorbed spontaneously on a substrate (metal or semiconductor) through physical or chemical absorption and is obtained by putting the substrate in a chemical solution or exposing it to vapor.[19] Langmuir-Blodgett (LB) film formation and self-assembly in solution are the most common methods of monolayer preparation.[19] To prepare a self-assembled monolayer of PNA, or another molecule, on gold, the typical route is to incubate a clean gold surface in a low concentration solution of the molecules for a certain period of time.

A well ordered SAM formed on a substrate provides a structure for experimental testing and has many potential applications. In protective coatings, the SAM plays a key role in preventing corrosion by blocking the access of molecules to the metal surface.[20] SAMs are used to adjust the wetting of a surface by changing the end-group (hydrophilic or hydrophobic). This property can be used in friction or lubrication control.[21,22] SAMs are promising in the context of microcontact printing (μCP),[23] microelectronics and micro-optical-electronics.[24] The electronic properties of SAMs can have a profound effect on the electron transfer of molecules, which is an aspect of molecular electronics. In the biomedical field, SAMs are used as an interface-layer to fabricate sensors or biosensors. Biomaterials can be immobilized on a SAM to mimic the interaction with biological interfaces.[25]

In the past two decades, a large number of research groups have tried to understand the formation of alkanethiol monolayers. However, much less effort has been

spent on PNA monolayer formation. Recently, Martin-Gago's research group tried to understand the mechanism of PNA SAM formation. They found that the mechanism for alkanethiol and PNA SAM formation is similar. Below I discuss the mechanism of PNA SAM formation according to Martin-Gago's group.[26-28]

The structure and growth of SAMs have been evaluated by many techniques, such as X-ray photoelectron spectroscopy (XPS), atomic force microscopy (AFM), X-ray absorption near-edge spectroscopy (XANES), and reflection-absorption infrared spectroscopy (RAIRS).[26-28] They studied Cys-O-O-AATCCCCGCAT ss-PNA molecule ("O" spacer unit is a molecule of 8-amino-3,6-dioxaoctanoic acid), at concentrations ranging from 0.01 μM to 10 μM. Experimental results show that the self-assembly occurs in two steps. The first step is very fast and lasts for a few minutes. In this first step, molecules condense on the surface and are adsorbed on surface as "lying-down" molecules. The second step is slower and lasts for several hours before a final stable structure is formed. In this step, the layer undergoes a phase transition and the molecular backbone realigns perpendicular to the surface. Although PNA is a large molecule, compact monolayer formation is still favored because of lack of charges in the backbone of PNA which avoids electrostatic repulsions either among neighboring molecules or among the solvent counter ions. Martin-Gago's group has found that PNA SAM formation is concentration dependent. Their studies investigated how the realignment of the PNA depends on the concentration of PNA solution and found that at least 1 μM concentration is required for compact PNA SAM formation. Lower concentrations of PNA results in a strong chain-surface interaction and hence the molecules do not reorient from the lying down to the standing-up phase. At higher concentration, attractive

interactions between adjacent chain increases and hence reorientation from “lying-down” to “standing-up” takes place.

1.4 Electron Transfer (ET) Theory[29-38]

Electron transfer refers to the charge separation process between a Donor (D) and Acceptor (A) complex, which is represented in scheme 1.1. Based on the strength of the interaction between D and A, electron transfer reactions can be classified into two categories, inner-sphere ET and outer-sphere ET. In the inner-sphere ET, there is a strong interaction between D and A, and properties of D and A in a DA complex differ from those of its free precursors. In the outer-sphere ET, only a weak interaction occurs between D and A, and the properties of D and A in the DA complex can be treated as the same as those of their precursors.

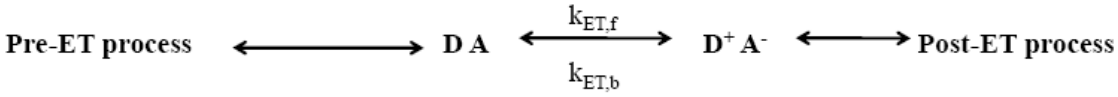

Scheme 1.1 Schematic representation of the electron transfer in donor-acceptor complex.

1.4.1 Classical Marcus Theory

The kinetics of electron transfer (ET) can be understood by Marcus Theory.[9] Based on transition state theory, classical Marcus theory assumes a reaction coordinate for an electron transfer reaction that corresponds to polarization changes in the medium. The polarization changes by nuclear motions, such as the orientation of the dipole of solvent molecules and the stretching of certain chemical bonds. Figure 1.3 shows the Gibbs free energy surfaces for the reactant and product as a function of the polarization coordinate. The Marcus theory assumes a quadratic shape for the potentials with the same force constant. The potential surfaces cross each other at point C. The coordinate q_R and q_P

refer to the equilibrium state of the product and the reactant. By thermal fluctuations, reactant molecules reach point C, the transition state where electron transfer occurs. The electron transfer rate constant k_{ET} may be written as

$$k_{ET} = \kappa_{el} \nu_n \exp(-\frac{\Delta G^*}{k_B T}) \qquad (1\text{-}2)$$

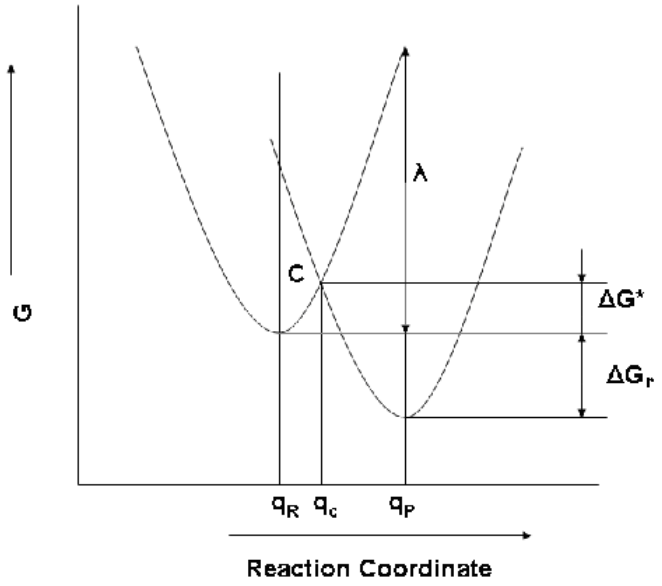

Figure 1.3 The free energy surface for an electron transfer reaction

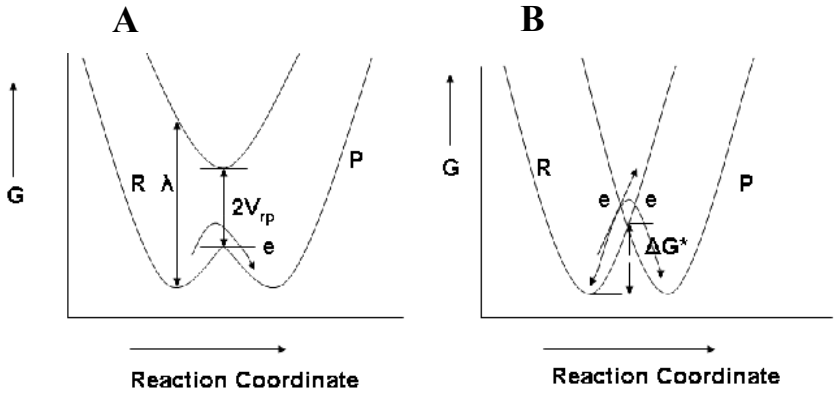

Figure 1.4 Schematic diagrams for adiabatic (A, strong coupling) and nonadiabatic (B, weak coupling) electron transfer reactions.

where κ_{el} is the electronic transmission coefficient, ν_n is the frequency of passage (nuclear motion) through the transition state corresponding to point C, ΔG^* is the activation energy, k_B is the Boltzmann constant, and T is the temperature. An electron transfer reaction is classified as either "adiabatic" or "nonadiabatic" according to the strength of the coupling V_{rp} (Figure 1.4). For an adiabatic ET reaction, κ_{el} =1, which means that every passage through the transition state leads to electron transfer. For a nonadiabatic electron transfer reaction, κ_{el} <<1, and just a small fraction of passages through the transition state lead to electron transfer.

If the quadratic energy surfaces have the same force constant, the ΔG^* can be calculated from the free energy of reaction ΔG_r and the reorganization energy λ by the following Equation 1-3,

$$\Delta G^* = \frac{(\lambda + \Delta G_r)^2}{4\lambda} \qquad (1\text{-}3)$$

The reorganization energy λ is defined as the energy required to transfer the electron from the bottom of the energy profile of the reactant state up to the product state at same nuclear configuration as the energy minimum of the reactant state. In Figure 1.3, the reorganization energy of the reactant state has been shown. Both the inner (λ_{in}) and outer (λ_{out}) reorganization energy contribute to λ, such that

$$\lambda = \lambda_{in} + \lambda_{out} \qquad (1\text{-}4)$$

In the harmonic approximation, the inner reorganization energy λ_{in} is given by

$$\lambda_{in} = \frac{1}{2}\sum_i \overline{f_i}(r_R^{eq} - r_P^{eq})^2 \qquad (1\text{-}5)$$

where r_R^{eq} and r_p^{eq} are the equilibrium bond lengths in the reactant and product states respectively. $\overline{f_i}$ is a reduced force constant of the i^{th} vibrational mode. The outer

reorganization energy λ_{out} is correlated to the orientation and polarization of solvent molecules near the DA complex. In a two-sphere dielectric continuum model, the reorganization energy is given by

$$\lambda_{out} = \frac{e^2}{8\pi\varepsilon_0 r}\left(\frac{1}{\varepsilon_{op}} - \frac{1}{\varepsilon_s}\right) \qquad (1\text{-}6)$$

where ε_0 is the permittivity of vacuum, r is the radius of the redox species, ε_{op} and ε_S are the optical and static dielectric constants respectively.

1.4.2 Quantum Mechanical approach to Electron Transfer:

The classical Marcus theory works well in many cases. However it must be extended to account for quantum mechanical aspects, in particular to account for the high frequency nuclear modes and to obtain the transmission coefficient κ_{el} for nonadiabatic ET. In quantum mechanics, the electron donor and acceptor are treated as an ensemble. It is common to use time-dependent perturbation theory, the Fermi "Golden rule" expression, to calculate the transmission rate constant Γ_j from the level j of the reactant state to a set product state i as

$$\Gamma_j = \frac{2\pi}{\hbar}\left|V_{rp}\right|^2 \sum_i \left\langle \varphi_{p,i} \middle| \chi_{r,j} \right\rangle^2 \delta(\varepsilon_{p.i} - \varepsilon_{r,j}) \qquad (1\text{-}7)$$

where $\left|V_{rp}\right|$ is the electronic coupling between reactant and product states. $\chi_{r,j}$ and $\varphi_{p,i}$ are the vibrational wave functions for the equilibrium reactant level j and product level i, $\varepsilon_{r,j}$ and $\varepsilon_{p,i}$ are the corresponding energies of level j and i, and $\delta(x)$ is the Dirac delta function that ensures the transmission meet the requirement of energy conservation. The electronic coupling, $|V_{rp}|$ is commonly assumed to have an exponential dependence on the distance between donor and acceptor,

$$\left|V_{rp}\right| = \left|V_{rp}^{0}\right| \exp(-\frac{\beta}{2} d) \tag{1-8}$$

where β is the tunneling decay coefficient, d is the distance between the donor and acceptor, and $|V_{rp}^{0}|$ is the electronic coupling at d=0.

For thermal distributions, more than one reactant state can be the initial state of the transmission. The overall rate constant is the sum over all reactant's vibrational levels, weighted by some distribution law $\rho(\varepsilon_j)$, such as the Boltzmann distribution.

$$k_{ET} = \frac{2\pi}{\hbar}\left|V_{rp}\right|^2 \sum_j \sum_i \left\langle \varphi_{p,i} \middle| \chi_{r,j} \right\rangle^2 \rho(\varepsilon_j)\delta(\varepsilon_{p,i} - \varepsilon_{r,j}) \tag{1-9a}$$

or more compactly

$$k_{ET} = \frac{2\pi}{\hbar}\left|V_{rp}\right|^2 FCWD \tag{1-9b}$$

where FCWD is called the Franck-Condon weighted density-of-states.

Several approximations are used in the treatment of FCWD and result in different expressions for k_{ET}. In the "high-temperature limit" of Marcus theory, the vibrations can be described classically and the electron transfer rate follows equation 1-10

$$k_{ET} = \frac{2\pi}{\hbar}\left|V_{rp}\right|^2 (4\pi\lambda k_B T)^{-1/2} \exp\left(-\frac{(\lambda + \Delta G_r)^2}{4\lambda k_B T}\right) \tag{1-10}$$

By introducing an "adiabaticity" factor g, an expression that changes smoothly between the adiabatic and nonadiabatic limit for the ET rate constant is given as:

$$k_{ET} = \frac{2\pi}{\hbar}\left|V_{rp}\right|^2 (4\pi\lambda k_B T)^{-1/2} \left(\frac{1}{1+g}\right) \exp\left(-\frac{(\lambda + \Delta G_r)^2}{4\lambda k_B T}\right) \tag{1-11}$$

and

$$g = \frac{\pi^2 k_B T \left|V_{rp}\right|^2 \tau_{eff}}{\hbar\lambda} \tag{1-12}$$

where τ_{eff} is the effective dielectric relaxation time. When g<<1, the electron transfer is in the nonadiabatic limit and equation 1-11 is transformed into equation 1-10. When g>>1, one obtains equation 1-13 for adiabatic ET rate constant:

$$k_{ET} = \frac{1}{\tau_{eff}} \sqrt{\frac{\lambda}{\pi^3 k_B T}} \exp\left(-\frac{(\lambda + \Delta G_r)^2}{4\lambda k_B T} \right) \qquad (1\text{-}13)$$

1.4.3 Electron Transfer on Electrode Surface

On a metallic electrode surface, the redox species and the electrode form the donor and acceptor system. In a cathodic reaction, the electrode is the donor and electron transfer proceeds from a filled electronic state of the metal to a vacant electronic state of the redox species whose population has a Gaussian distribution centered at E=λ_{ox} (Figure 1.5), and the molecule is reduced. For an anodic reaction, electron transfer proceeds from filled electronic states of the redox species, which have a Gaussian distribution centered at E= λ_{red}, to vacant electronic states of the metal, and the molecule is oxidized.

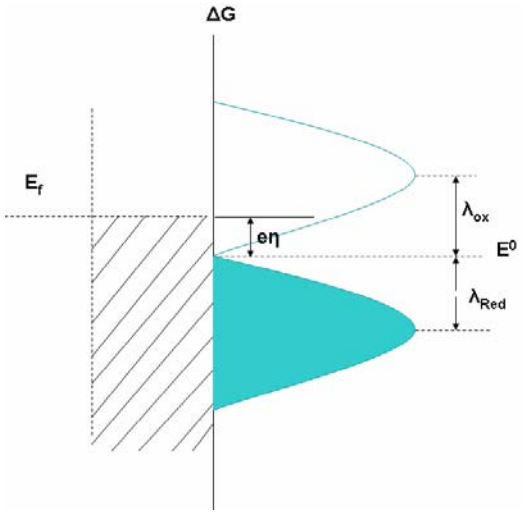

Figure 1.5 Schematic diagram of the density of metallic electronic states, E_f is the Fermi energy, and E^0 is the free energy corresponding to the formal potential.

The Gibbs energy of this reaction can be expressed as:

$$\Delta G_r = (\varepsilon_f - \varepsilon) + e\eta \qquad (1\text{-}14)$$

Combining equations 1-14 and equation 1-10, the electron transfer rate constant of transmission from one metallic level to a redox species is given as:

$$k_{RED} = \frac{2\pi}{\hbar}\left|V_{rp}\right|^2 (4\pi\lambda k_B T)^{-1/2} \exp\left(-\frac{(\lambda + (\varepsilon_f - \varepsilon) + e\eta)^2}{4\lambda k_B T}\right) \qquad (1\text{-}15)$$

The overall reaction rate is the properly weighted sum over all the ET rate constants relating to these levels because the metal electrode has more than one electronic state available. Therefore the rate constant is:

$$k_{RED} = \frac{2\pi}{\hbar}\left|V_{rp}\right|^2 (4\pi\lambda k_B T)^{-1/2} \int_{-\infty}^{\infty} \rho(\varepsilon) P(\varepsilon) \exp\left(-\frac{(\lambda + (\varepsilon_f - \varepsilon) + e\eta)^2}{4\lambda k_B T}\right) d\varepsilon \qquad (1\text{-}16)$$

where ρ(ε) is the density of electronic states of the metallic electrode, and P(ε) is the Fermi-Dirac distribution law:

$$P(\varepsilon) = \frac{1}{1 + \exp\left(\frac{\varepsilon - \varepsilon_f}{k_B T}\right)} \qquad (1\text{-}17)$$

The oxidation rate constant can be obtained in a similar way

$$k_{OX} = \frac{2\pi}{\hbar}\left|V_{rp}\right|^2 (4\pi\lambda k_B T)^{-1/2} \int_{-\infty}^{\infty} \rho(\varepsilon)(1 - P(\varepsilon)) \exp\left(-\frac{(-\lambda + (\varepsilon_f - \varepsilon) + e\eta)^2}{4\lambda k_B T}\right) d\varepsilon \qquad (1\text{-}18)$$

1.4.4 Kinetic Studies of Electron Transfer on Electrodes

Kinetic studies of electron transfer on electrodes can be performed by using several electrochemistry techniques, such as chronoamperometry, cyclic voltammetry, square-pulse voltammetry, and AC cyclic voltammetry. Cyclic voltammetry is simple and straightforward in kinetic studies. In this technique, a linear time dependent potential is applied to a working electrode at a certain sweeping speed in a cyclic way. The current-voltage curve is recorded and contains kinetic information. At slow scan rate, the

separation between oxidation and reduction peaks is small and at higher scan rate it increases. It is straightforward to extract kinetic parameters for a redox system from a voltammogram, which can be done by fitting experimental data to a model. Marcus theory is used for the determination of kinetic parameters. In this method, the experimental peak separation/ scan rate data is fitted by the theoretical prediction. The standard electrochemical rate constant k^0 can be determined from the fitting of experimental data with the theoretical curve.

1.5 Chirality Effects in Electron Transfer

Chapter 2 of this thesis deals with the effect of molecular chirality on electron transmission, explored by photoelectrochemistry. In that chapter, the dependence of the photocurrent on the polarization of the light field will be discussed. In this section, I discuss spin polarization of light, electronic excitation and helicity of porphyrin chromophores, and the interaction of electron helicity with molecular chirality.

1.5.1 Spin Polarization of Light

Photons have an intrinsic angular momentum, spin, and the "spin axis" of a photon is always parallel to its direction of motion, pointing either forward or backward since photons travel at the speed (c). These two spin states correspond to an electric field that is rotating either counterclockwise or clockwise about the propagation axis. If electrons are excited by the photon absorption then the angular momenta from the circular polarized light (with coherent spin, left or right), will generate an electron orbital momentum and the excited state will be polarized.

1.5.2 Electronic Excitation and Helicity of Porphyrins

Properties of porphyrins have been studied intensively[39] and refined continuously.[40,41] The theoretical models for the electronic structure of the porphyrins have been developed and understood, in terms of their spectroscopy. The basic porphyrin ring has a conjugated ring of 16 inner C-atoms with 18 π electrons, which are responsible for the porphyrin optical spectra. By treating the 16 atom cyclic polyene distorted by 4 pyrrole nitrogen atoms with simple extended Hückel molecular model, Gauterman and coworkers[42] have successfully, and the first time quantitatively, developed a 4-orbital model to describe the relative intensities of the two lowest energy $\pi \rightarrow \pi^*$ electronic transitions in porphyrin complexes. This model explains the absorption spectrum of porphyrin rings. The transition between the lowest energy excited singlet state and the electronic ground state Q(0,0) corresponds to the Q band, which typically lies between 500 nm and 650 nm; whereas the transition between the second excited singlet state and the ground state corresponds to the B bands (or Soret bands), typically located between 380 nm and 420 nm. Changes in porphyrin centers results in a variety in electronic and optical properties. Early studies[43] have found the two-banded (1Q,1B) visible spectrum observed from most metal or di-proton centered porphyrin complexes, distinctly different from the four-banded (2Q, 2B) visible absorption spectrum in free base porphyrins, because the centered two free base protons or metal center reduce the porphyrin ring symmetry from D_{4h} to D_{2h}. A shoulder may show up on the high energy side (blue) of the Soret band due to one mode of vibrational excitiation B(1-0). Other bands with higher energy and much smaller intensities, N, L, and M bands, occur.

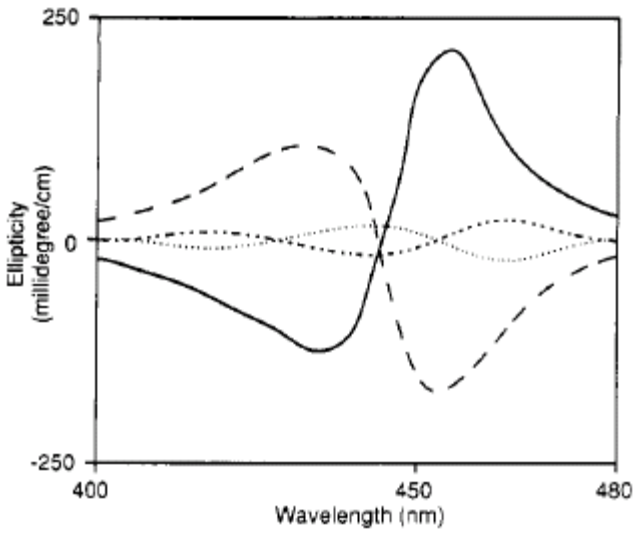

Figure 1.6 An induced circular dichroism spectra of 5 uM free base porhyrin aggregate (trans-bis(N-methylpyridinium-4-yl)-diphenylporphine) in the presence of 50 μM polypeptides at pH4.5. Solid curve: poly-D-glutamate with 0.1 M NaCl, dashed curve: poly poly-S-glutamate with 0.1 M NaCl. This figure is taken from reference 48.

Light induced electronic polarization in porphyrin complexes is an important optical property, and has been widely studied by using time resolved electron paramagnetic resonance spectroscopy (EPR),[44,45] time dependent fluorescence anisotropy,[40,41,46,47] and circular dichroism.[40,48,49] In the early 1980's, Gibbs and coworkers[50] found large induced circular dichroism signals in the Soret (B) region of supramolecualr porphyrin-nucleic acid (DNA) structures. Later, circular dichroism was observed in many bis-porphyrin derivatives[40,47] and peptide-porphyrin complexes or porphyrin aggregates.[48] Figure 1.6 shows an example of induced CD signals of free base porphyrin aggregates (*trans*-bis(N-methylpyridinium-4-yl)-diphenylporphine) in the presence of poly-Lglutamate or poly-D-glutamate peptide, which was reported to have a helical structure.[51,52] A much weaker CD signal was observed from the porphyrin monomers in the solution (the dotted curve in Figure 1, no NaCl is added). The added

NaCl generates porphyrin aggregates. The phases of the induced CD signal of the porphyrins is reversed for the D versus L helical forms of the peptide, indicating the electronic helicity of excitation at the Soret region.

Given that the porphyrin monomer is not optically active, the electronic helicity can be ascribed to the long range coupling of transition dipole moments of porphyrin molecules (aggregate) orienting on the helical scaffold structure. An exciton model, described by Kasha[53] for molecular aggregates, was developed to understand porphyrin complex derivatives.[40,54,55] In this model, the B band is described as a combination of two mutually perpendicular oscillators, and they are considered degenerate in the metal (or deprotonated) porphyrin (with D_{4h} symmetry) or free base porphyrin (D_{2h} symmetry). In other words, the Soret band (B band) of a porphyrin monomer has two components of absorption arising from B(0,0) and B(1,0). The B(0,0) is due to the excitation from ground state to the second excited singlet state whereas B(1,0), which is higher in energy, is due to the addition of one mode of vibrational excitation,[42] so that the single intense band at Soret band is a combination of both B(0,0) and B(1,0). These two B bands have polarizations perpendicular to each other. In the porphyrin aggregate, the exciton interaction can split these two B bands, since these two bands have polarizations perpendicular to each other and hence they can display circular dichroism (CD).

As a summary, one can expect to obtain nonequilibrium electron polarization in the excitation at Soret band if a circular polarized light (left or right) illuminates to porphyrin complex with interporphyrin helicity.

1.5.3 The Interaction of Electron Helicity with Molecular Chirality

There is an asymmetry in the interaction of chiral molecules with spin polarized electrons. Kessler and coworkers[56,57] observed the spin-dependence of electron beams transmitted through metal-centered chiral molecules in the gas phase with an asymmetry factor of 10^{-4}. In a photoemission experiment, Ray et al.[58] measured a larger asymmetry factor of 10^{-1} from multiple pure well-oriented chiral Langmuir-Blodgett films. Recently, Lischke and coworkers[59] investigated the asymmetry in angle-resolved photoelectron emission from unoriented chiral molecules and found an asymmetry of up to several percent, which varied as a function of the orbital binding energy. Other than these experimental studies, the corresponding theoretical [60-64] for the asymmetries in the collision of the polarized electron and chiral centers for both the oriented or unoriented molecules through electron scattering or photoemission are available.

General formulae allow people to disentangle the physical and orientation contributions to the experimental investigation of the asymmetries in collisions between the electrons and oriented chiral molecules.[60-64] For a given molecule system (M) (orientation defined by Euler angles αβγ), the asymmetry factor in cross section for elastic collisions between the molecules and electrons is defined as:

$$A = \frac{M(\sigma+) - M(\sigma-)}{M(\sigma+) + M(\sigma-)} \qquad (1\text{-}19)$$

where the electron spin is up (σ+) or down (σ-), Whereas the asymmetry factor for collision between different isomers (molecular M and its optical enantiomer M') and electrons with definite helicity (spin up or down) is defined as:

$$\eta = \frac{M(\sigma+) - M'(\sigma+)}{M(\sigma+) + M'(\sigma+)} \tag{1-20}$$

In an unoriented molecular system, the two asymmetry factors should be the same due to the symmetry requirements. For oriented molecule systems, the A and η can be different, and η can be much larger than A. Kessler[56,57] has measured the asymmetry A, while Ray et al.[58] have measured η.

A theoretical approach in terms of so-called "steric factors"[61] has shown that the asymmetry *A* may depend on the molecular orientation during the elastic collision (electronic scattering) between electron helicity with the oriented chiral molecules, and the asymmetry factor can be one to two orders of magnitude larger than the unoriented chiral molecules.[60] Figure 17 provide an example of some numerical results for the asymmetry factor A that is obtained through the theoretical approach. In this figure, α=β=0º, the C-Cl bond is parallel to the incoming beam axis. The molecule is rotated around z=Z, then the γ is changing, and A is shown as a function of γ. The results show that the left-handed electrons for M, the right-handed electrons for M' are scattered preferentially, and the asymmetry is about one order larger than the result from unoriented molecules. The studies on electron scattering in the gas phase or electron photoemission through oriented chiral molecules both experimentally and theoretically have demonstrated that the transmission efficiency of electrons through a target of chiral molecules may depend on the helicity of the electron (electron spin polarization or spin coherence). The larger asymmetry when the spin polarized electron transmits through assemblies of oriented chiral molecules may result from the electron's wavefunction interacting with many chiral molecules in the organized structure.[58]

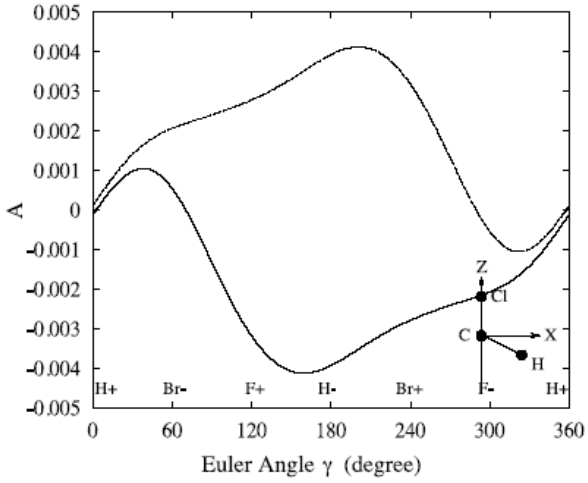

Figure 1.7 A simulation of geometry dependent asymmetry A for CHBrClF in electron scattering. Electron energy 5.0 eV, α=0º, β=0º incoming electron bean orientation: θ=20º; Solid curve: molecule M, and dashed curve: enantiomer M'. This figure is taken from reference 61.

Electron transfer through helical supramolecular structures has been intensively studied by using DNA, polypeptide, polymers or anologs, but the chirality effect has been investigated or exploited scarcely. Pujols-Ayala et al.[65] studied the role of peptide bonds in electron transfer. Kimura group[66,67] measured the large dipole moment caused by a helical peptide in the photoinduced electron transfer. Schenning and coworkers[68] have realized well-defined chiral fibers incorporating donor and acceptor chromophores by self-assembly and measured the electron transfer rate constant, but no chiral effects were addressed. Hence, a combined study of chirality and electron helicity in electron transfer through helical structures would be of great interesting for addressing the fundamentals of electron spin-chirality coupling or spin coherence transfer through supramolecules and biomolecules and for possible exploitation in applications in the molecular recognition, chirality discrimination, quantum information processing and so on. In Chapter 2, the results of polarized electrons transferring through a self-assembled helical scaffold on a gold surface are reported, including the scaffold monolayer preparation, characterization,

asymmetry measurements and hypothesized mechanism of the coupling between electron helicity and molecular chirality, etc.

1.6 Hopping Mechanism

In 1962, Eley and Spivey[69] first proposed that π- π interactions between stacked base pairs in double stranded DNA could provide a pathway for rapid, one-dimensional charge separation. Later on Barton and her colleagues[70-75] found almost distance-independent charge transfer in DNA. They proposed that "DNA behaves like a molecular wire where orbitals of stacked bases form a π-way for radical cation migration". But later on Lewis,[76] Tanaka[77] and Giese[78] groups performed charge transfer measurements in DNA at short distance and found a decay constant (β) in the range of 0.6-1.5 $Å^{-1}$, which was in dramatic conflict with Barton's results. Research of these groups showed the validity of the Marcus-Levich-Jortner[79-84] description for DNA, which predicts an exponential distance dependence and can be written as equation (1-21)

$$k = \frac{2\pi}{\hbar} V_0^2 F \exp(-\beta R) \qquad (1\text{-}21)$$

where F is the thermally-averaged nuclear Franck-Condon density, and the electronic coupling (V) is

$$V = V_0 \exp[-(\frac{\beta}{2} R)] \qquad (1\text{-}22)$$

where, R is the distance between donor and acceptor. Interestingly, research of Giese[85-89] and Schuster[89-94] groups showed a weak distance dependence at long distance with; $\beta \leq 0.1$ $Å^{-1}$. The above discussion leads to the unambiguous conclusion that at short distance charge transfer follows (i) the two-center unistep super-exchange mediated charge transfer described by equation (1-21), whereas at long distance, (ii) electron/ hole follows

a multistep charge "hopping" transport via bases in the DNA. This thesis work finds a similar result for PNA. Chapter 4 of this thesis shows the validity of these two mechanisms in PNA. The open question will be "at what distance the super-exchange mechanism will switchover to the hopping mechanism". In chapter 4, one of the theoretical models in this regard will be discussed and experimental results of PNA will be compared with theoretical predictions.

Although it is well accepted that the "hopping" mechanism is the mechanism of long range charge transport in DNA, the exact mechanistic picture of this transport remains elusive. Jortner proposed an "incoherent, random-walk, multi-step hopping" mechanism,[95] whereas Schuster proposed a "phonon-assisted polaron-like hopping" mechanism.

1.6.1 Incoherent random-walk multi-step hopping mechanism[95]

Electron/hole transfer in Donor (D)-Bridge (B_j, j=1, 2, 3--N)-Acceptor (A) structures occurs by off–resonance coupling between the electronic origin and low vibronic states of the initial state D{B_j}A state with all of the $D^+\{B_j\}^-A$ vibronic manifolds with a large energy gap $\delta E \rangle\rangle 0$ (Figure 1.8 (A)). This mechanism is known as super-exchange charge transfer and follows Equation (1-23). On the other hand, electron/hole transport can occur through resonant coupling ("hopping transport"), when three energetic conditions are satisfied simultaneously (Figure 1.8 (B)): (i) resonant coupling between the electronic origin and low vibronic levels of the initial D{B_j}A state with the vibronic manifolds of the primary ion pair $D^+B_1^-B_2...B_NA$, i.e., δE<0; (ii) near degeneracy of the vibronic manifolds of the ion pair states $D^+B_1^-B_2...B_NA$, $D^+B_1B_2^-...B_NA$ and $D^+B_1B_2...B_N^-A$; and (iii) degeneracy of the vibronic manifolds of the

base ion pairs state $D^+B_1B_2...B_N^-A$ and the ion pair state $D^+B_1B_2...B_NA^-$. The resonant coupling (i) results in the charge injection of the hole/electron into the appropriate B_1 base of DNA; the near degeneracy (ii) then will induce charge hopping between the $\{B_j\}(j=1,\ldots N)$ bases while the degeneracy (iii) will result in charge (hole/electron) trapping at the acceptor center.

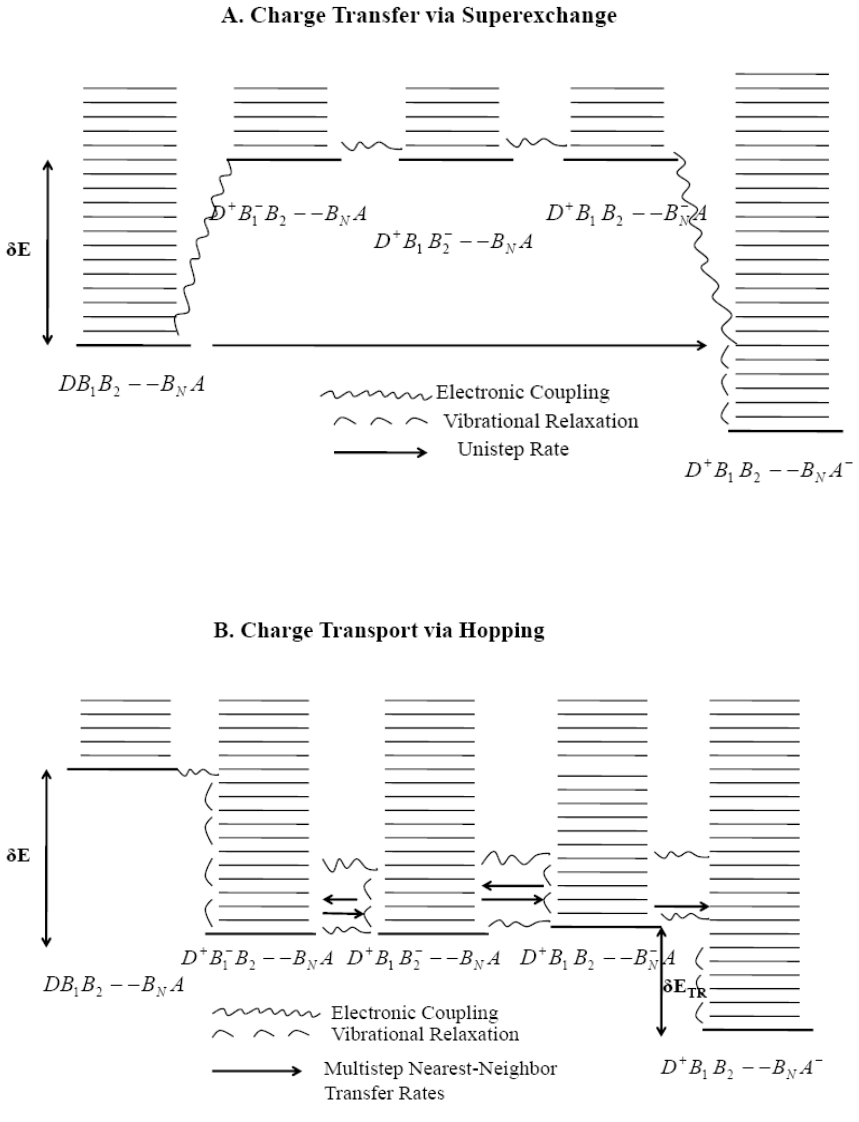

Figure 1.8 Vibronic level scheme for the two distinct charge migration mechanisms in DNA. (A) Unistep charge transfer via superexchange. (B) Multistep charge transport via hopping and trapping.

The charge hopping rate (k_{Hop}) for symmetric electron transfer ($\Delta G=0$) is given by equation (1-23)

$$k_{Hop} = \frac{2\pi}{\hbar} t^2 F_{Hop} \qquad (1\text{-}23)$$

where F_{Hop} is the Franck-Condon density and t is the exchange coupling between adjacent bases.

The multi-step hopping charge transport process constitutes a series of individual charge transfer processes between adjacent units in the system. This stepwise mechanism can be described by a diffusion model. Hence, a diffusional coefficient (D)[96,97] for the hopping transport can be defined by equation 1-24

$$D \approx k_{Hop} (r_0)^2 \qquad (1\text{-}24)$$

where, r_0 is the distance between the two nearest bridge sites. The time scale τ for the charge diffusion over the donor-acceptor spatial distance R, as characterized by the diffusion process, is given by

$$R = (2D\tau)^{1/2} \qquad (1\text{-}25)$$

Making contact between the time scale for diffusive hopping and the number of constituents in the chain $N=R/r_0$, a weak distance (N) dependence of the charge separation is obtained, i.e.

$$\tau = \frac{N^2 (r_0)^2}{2D} = \frac{N^2}{2k_{Hop}} \qquad (1\text{-}26)$$

A characteristic lifetime (τ_{COM}) for competitive charge depletion can be incorporated, so that yield for charge transport (Y) is,

$$Y = \tau^{-1}(\tau^{-1} + \tau_{COM}^{-1})^{-1} = (1 + \delta N^2)^{-1} \qquad (1\text{-}27)$$

where $\delta = (2k_{Hop}\tau_{COM})^{-1}$

According to the "hopping mechanism" of Equation 1-27, the decay of charge transport follows weak (algebraic) distance dependence with respect to N, i.e. charge transport will decrease as the number of hopping steps increases. The hopping mechanism will follow equation 1-28

$$\ln(Y) \propto -2\ln(N) \qquad (1\text{-}28)$$

It should be noted that equation 1-27 is valid only for an unbiased hopping process. For a biased hopping process equation 1-27 should be replaced by equation 1-29

$$Y = (1 + \delta N^{\eta})^{-1} \qquad (1\text{-}29)$$

and hence equation 1-28 will be replaced by equation 1-30

$$\ln(Y) \propto -\eta \ln(N) \qquad (1\text{-}30)$$

The parameter (η) (i) for acceptor biased random walk will be $1 \leq \eta \leq 2$. (ii) For donor direction biased random walk η will be greater than 2, whereas for unbiased charge hopping η will be 2.

1.6.2 Phonon-Assisted Polaron Like Hopping Mechanism[89,92]

Schuster and coworkers proposed a different hopping mechanism which is known as the "phonon assisted polaron like hopping mechanism". A polaron is a radical ion self-trapped by a structural distortion of its medium. The polaron can migrate by phonon assisted (thermally activated) hopping. This model is based on an understanding of the dynamical structure of DNA in solution. The fundamental assumption of this model is that the introduction of a base radical cation into DNA will be accompanied by a consequent structural change that lowers the energy for the system. A base radical cation

is a highly electron-deficient species: it will be stabilized and the energy of the system will be reduced by changes in the average orientations of nearby bases, counter ions and solvent molecules that provide additional electron density to the radical cation. This process will delocalize the radical cation and cause a local distortion of the DNA structure so that, on average, it is no longer in the standard form. This distortion may not extend over many base pairs because the stabilization gained by delocalization must be balanced by the energy required to distort the average DNA structure. In this view, radical cations in DNA are self-trapped species that are delocalized over several base pairs contained within a distorted local structure, which is the definition of a small polaron.

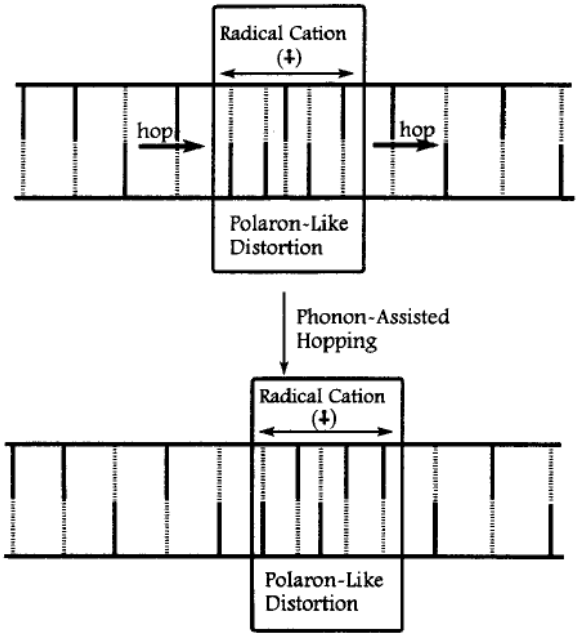

Figure 1.9 Symbolic representation of a polaron-like distortion in duplex DNA. Vertical line represents DNA base (solid for purines and dashed for pyrimidines). The polaron like distortion is contained within the rectangle symbolized by a decrease if base pair distance. The radical cation charge and free radical density of the polaron is portrayed as delocalized throughout its structure. Hopping of the polaron, in this case with a step size of 1 base pair joining the structure (on the right) and one leaving (on the left). This figure is taken from reference 92.

Figure 1.9 shows schematic representations of possible polaron-like species in DNA. In the figure, the DNA bases are represented as a series of vertical lines (dashed for the purines and solid for the pyrimidines) distributed between horizontal lines that represent the sugar-phosphate backbone. The box within this representation portrays the distortion of the polaron by placing the base pairs closer together in this region. This distortion of the DNA structure from its normal B-form average results in the delocalization of the radical cation among the bases included in the distortion. The polaron-like distortion is considered to hop through the DNA duplex, a process may either increase or reduce the number of base pairs in the polaron; the size of the hopping step will be controlled by the sequences of the bases that make up the polaron and by those surrounding it.

Polaron hopping permits the reduced effect of specific base sequence on radical cation migration efficiency. According to this model, the barrier for each hopping step of the polaron is approximately the same height, independent of base sequence. The height of the barrier is the difference between the energy of a polaron and the transition state that separates it from the next.

If a strand of DNA is composed of sequential adenines or guanine (An or Gn), comparable stablilization of the polaron would likely involve fewer bases than is a segment having mixed sequences of purines and pyrimidines. However, the relative energies of the two polarons could be averaged to a similar value even though they extend over a different number of bases having different sequences. The energy of the transition state that separates two polarons may also become less dependent on specific base sequence by averaging. There is no requirement that the number of bases in a hop from one location to the next to be constant. If the hopping length is somehow dependent

upon the identity of the bases separating the polarons, the energy of the transition state is averaged by different hopping lengths.

In the following chapters, I will discuss results obtained for self-assembled monolayers of PNA and chiral organic molecules. Chapter 2 deals with the effects of molecular chirality and electron spin polarization in the electron tunneling. A molecule of chiral structure and terminated with a chromophore (porphyrin) was prepared as a SAM on a gold surface. The photocurrent produced by irradiation with 435 nm light gives rise to a noticeable chiral asymmetry in the photocurrent.

Chapters 3 through 5 describe our studies of charge transfer through PNA self-assembled monolayer films. In Chapter 3 the charge transfer through SAMs composed of different single stranded thymine containing PNA molecules is described. In these studies, the length of the molecule was varied by varying the number of nucleobases. Among the four common nucleobases thymine (T) and cytosine (C) have the highest oxidation potential and are hardest to oxidize. As a result, the tunneling mechanism is likely to be operative at longer distance for thymine containing ss-PNA molecules than for G or A ss-PNA molecules. In this part of the work, the monolayer formation has been monitored by cyclic voltammetry (CV) and the charge transfer rate through ss-T-PNA has been determined. The tunneling decay constant (β) is determined for ss-T-PNA.

Chapter 4 deals with charge transfer mechanism switchover from "tunneling" to "hopping" in PNA. CT through three different types of PNA molecules, namely single stranded thymine containing PNA (ss-T-PNA), single stranded adenine containing PNA (ss-A-PNA) and double stranded adenine-thymine PNA (ds-(A-T)-PNA) are studied. This study directly observes the CT mechanism switchover from tunneling to hopping for

different types of PNA molecules and provides insight into the nature of the long range CT through PNA. The experimental work is compared with the predictions of previously published theoretical models.

Chapter 5 describes studies that consider the role of nucleobases on the CT through PNA molecules. In this study, oligomers of seven nucleobases (or base pairs) were studied for both single stranded and double stranded PNA molecules. In each case, six of the bases were T (or A-T for the duplex) and the fourth nucleobase (or base pair) was replaced with all possibilities. This work shows that the identity of the nucleobase controls the rate of the CT through the PNA; i.e, the nucleobase or base pairs can be used to manipulate the flow of charge through the molecular bridge.

Chapter 6 summarizes all the CT systems examined in this thesis work and provides a brief perspective comments.

1.7 References

(1) Egholm, M.; Buchardt, O.; Christensen, L.; Behrens, C.; Freier, S. M.; Driver, D. A.; Berg, R. H.; Kim, S. K.; Norden, B.; Nielsen, P. E. *Nature* **1993**, *365*, 566-568.

(2) Egholm, M.; Nielsen, P. E.; Buchardt, O.; Berg, R. H. *J. Am. Chem. Soc.* **1992**, *114*, 9677-9678.

(3) Ray, A.; Norden, B. *FASEB J.* **2000**, *14*, 1041-1060.

(4) Uhlmann, E.; Peyman, A.; Breipohl, G.; Will, D. W. *Angew. Chem. Int. Ed.* **1998**, *37*, 2796-2823.

(5) Nielsen, P. E. *Peptide Nucleic Acids: Protocols and Applications;* Horizon Bioscience, Wymondham,UK, 2004.

(6) Misra, H. S.; Pandey, P. K.; Modak, M. J.; Vinayak, R.; Pandey, V. N. *Biochemistry* **1998**, *37*, 1917-1925.

(7) Koppitz, M.; Nielsen, P. E.; Orgel, L. E. *J. Am. Chem. Soc.* **1998**, *120*, 4563-4569.

(8) Good, L.; Nielsen, P. E. *Nat. Biotech.* **1998**, *16*, 355-358.

(9) Nielsen, P. E. *Current Opinion in Biotechnology* **1999**, *10*, 71-75.

(10) Corey, D. R. *Trends in Biotechnology* **1997**, *15*, 224-229.

(11) Petersson, B.; Nielsen, B. B.; Rasmussen, H.; Larsen, I. K.; Gajhede, M.; Nielsen, P. E.; Kastrup, J. S. *J. Am. Chem. Soc.* **2005**, *127*, 1424-1430.

(12) Rasmussen, H.; Kastrup, J. S.; Nielsen, J. N.; Nielsen, J. M.; Nielsen, P. E. *Nat. Struct. Biol.* **1997**, *4*, 98-101.

(13) Rasmussen, H.; Liljefors, T.; Petersson, B.; Nielsen, P. E.; Kastrup, J. S. *J. Biomol. Struct. Dyn.* **2004**, *21*, 495-502.

(14) Wittung, P.; Eriksson, M.; Lyng, R.; Nielsen, P. E.; Norden, B. *J. Am. Chem. Soc.* **1995**, *117*, 10167-10173.

(15) Franzini, R. M.; Watson, R. M.; Patra, G. K.; Breece, R. M.; Tierney, D. L.; Hendrich, M. P.; Achim, C. *Inorg. Chem.* **2006**, *45*, 9798-9811.

(16) Popescu, D. L.; Parolin, T. J.; Achim, C. *J. Am. Chem. Soc.* **2003**, *125*, 6354-6355.

(17) Watson, R. M.; Skorik, Y. A.; Patra, G. K.; Achim, C. *J. Am. Chem. Soc.* **2005**, *127*, 14628-14639.

(18) Watson, R. M. *PhD Thesis, Carnegie Mellon University* **2008**.

(19) Finklea, H. O. *Encyclopedia of Analytical Chemistry;* John Wiley & Sons Ltd, Chichester, 2000, 1-26.

(20) Scherer, J.; Vogt, M. R.; Magnussen, O. M.; Behm, R. J. *Langmuir* **1997**, *13*, 7045-7051.

(21) Xiao, X.; Hu, J.; Charych, D. H.; Salmeron, M. *Langmuir* **1996**, *12*, 235-237.

(22) Kim, H. I.; Graupe, M.; Oloba, O.; Koini, T.; Imaduddin, S.; Lee, T. R.; Perry, S. S. *Langmuir* **1999**, *15*, 3179-3185.

(23) Nuzzo, R. G. *Proc. Natl. Acad. Sci.* **2001**, *98*, 4827-4829.

(24) Fendler, J. H. *Chem. Mater.* **2001**, *13*, 3196-3210.

(25) Prime, K. L.; Whitesides, G. M. *Science* **1991**, *252*, 1164-1167.

(26) Briones, C.; Mateo-Marti, E.; Gomez-Navarro, C.; Parro, V.; Roman, E.; Martin-Gago, J. A. *Phys. Rev. Lett.* **2004**, *93*, 208103.

(27) Briones, C.; Mateo-Marti, E.; Gomez-Navarro, C.; Parro, V.; Roman, E.; Martin-Gago, J. A. *J. Mol. Catal. A: Chem.* **2005**, *228*, 131-136.

(28) Mateo-Marti, E.; Briones, C.; Roman, E.; Briand, E.; Pradier, C. M.; Martin-Gago, J. A. *Langmuir* **2005**, *21*, 9510-9517.

(29) Barbara, P. F.; Meyer, T. J.; Ratner, M. A. *J. Phys. Chem.* **1996**, *100*, 13148-13168.

(30) Bard, A. J.; Faulkner, L. R. *Electrochemical Methods; Fundamental and Applications;* Wiley, New York, 1980.

(31) Chidsey, C. E. D. *Science* **1991**, *251*, 919-922.

(32) Finklea, H. O. *In Electroanalytical Chemistry;* Bard, A. J., Rubinstein, I., Eds. Marcel Dekker Inc.: New York, 1996, 19, 109.

(33) Khoshtariya, D. E.; Dolidze, T. D.; Zusman, L. D.; Waldeck, D. H. *J. Phys. Chem. A* **2001**, *105*, 1818-1829.

(34) Marcus, R. A. *J. Chem. Phys.* **1956**, *24*, 966-978.

(35) Marcus, R. A. *J. Chem. Phys.* **1965**, *43*, 679-701.

(36) Miller, C. J. *Physical Electrochemistry: Principles, Methods and Applications.* Rubinstein, I, Ed. Marcel Dekker, Inc., New York, 1995, 27.

(37) Napper, A. M.; Liu, H.; Waldeck, D. H. *J. Phys. Chem. B* **2001**, *105*, 7699-7707.

(38) Wei, J.; Liu, H.; Dick, A. R.; Yamamoto, H.; He, Y.; Waldeck, D. H. *J. Am. Chem. Soc.* **2002**, *124*, 9591-9599.

(39) Kadish, K. M.; Smith, K. M.; Guilard, R. *The Porphyrin Handbook, Academic Press*.

(40) Pescitelli, G.; Gabriel, S.; Wang, Y.; Fleischhauer, J.; Woody, R. W.; Berova, N. *J. Am. Chem. Soc.* **2003**, *125*, 7613-7628.

(41) Guo, H.; Jiang, J.; Shi, Y.; Wang, Y.; Liu, J.; Dong, S. *J. Phys. Chem. B* **2004**, *108*, 10185-10191.

(42) Gouterman, M. J. *In the Porphyrins, Dolphin, D. Edt.; Academic Press;* New York, Vol 3, Part A Ch. 1, and reference therein.

(43) Craig, R. P.; Davidson, N. *J. Am. Chem. Soc.* **1951**, *73*, 1951-1954.

(44) van der Est, A.; Asano-Someda, M.; Ragogna, P.; Kaizu, Y. *J. Phys. Chem. A* **2002**, *106*, 8531-8542.

(45) Asano-Someda, M.; van der Est, A.; Kruger, U.; Stehlik, D.; Kaizu, Y.; Levanon, H. *J. Phys. Chem. A* **1999**, *103*, 6704-6714.

(46) Shediac, R.; Gray, M. H. B.; Uyeda, H. T.; Johnson, R. C.; Hupp, J. T.; Angiolillo, P. J.; Therien, M. J. *J. Am. Chem. Soc.* **2000**, *122*, 7017-7033.

(47) Kumble, R.; Palese, S.; Lin, V. S. Y.; Therien, M. J.; Hochstrasser, R. M. *J. Am. Chem. Soc.* **1998**, *120*, 11489-11498.

(48) Borovkov, V. V.; Lintuluoto, J. M.; Fujiki, M.; Inoue, Y. *J. Am. Chem. Soc.* **2000**, *122*, 4403-4407.

(49) Pasternack, R. F.; Giannetto, A.; Pagano, P.; Gibbs, E. J. *J. Am. Chem. Soc.* **1991**, *113*, 7799-7800.

(50) Gibbs, E. J.; Tinoco, J. I.; Maestre, M. F.; Ellinas, P. A.; Pasternack, R. F. *Biochem. Biophys. Res. Commun.* **1988**, *157*, 350-358.

(51) Idelson, M.; Blout, E. R. *J. Am. Chem. Soc.* **1958**, *80*, 4631-4634.

(52) Stryer, L.; Blout, E. R. *J. Am. Chem. Soc.* **1961**, *83*, 1411-1418.

(53) Kasha, M. *Radiat. Res.* **1963**, *20*, 55-70.

(54) Osuka, A.; Maruyama, K. *J. Am. Chem. Soc.* **1988**, *110*, 4454-4456.

(55) Ohno, O.; Ishikawa, N.; Matsuzawa, H.; Kaizu, Y.; Kobayashi, H. *J. Phys. Chem.* **1989**, *93*, 1713-1718.

(56) Mayer, S.; Kessler, J. *Phys. Rev. Lett.* **1995**, *74*, 4803.

(57) Mayer, S.; Nolting, C.; Kessler, J. *J. Phys. B: At. Mol. Opt. Phys.* **1996**, *29*, 3497-3511.

(58) Ray, K.; Ananthavel, S. P.; Waldeck, D. H.; Naaman, R. *Science* **1999**, *283*, 814-816.

(59) Lischke, T.; Böwering, N.; Schmidtke, B.; Müller, N.; Khalil, T.; Heinzmann, U. *Phys. Rev. A* **2004**, *70*, 022507.

(60) Smith, I. M.; Busalla, A.; Thompson, D. G.; Blum, K. *J. Phys. B: At. Mol. Opt. Phys.* **1998**, *31*, 4029.

(61) Musigmann, M.; Busalla, A.; Blum, K.; Thompson, D. G. *J. Phys. B: At. Mol. Opt. Phys.* **1999**, *32*, 4117-4128.

(62) Musigmann, M.; Blum, K.; Thompson, D. G. *J. Phys. B: At. Mol. Opt. Phys.* **2001**, *34*, 2679-2696.

(63) Musigmann, M.; Busalla, A.; Blum, K.; Thompson, D. G. *J. Phys. B: At. Mol. Opt. Phys.* **2001**, *32*, L79-L85.

(64) Blum, K.; Thompson, D. G. *Adv. At. Mol. Opt. Phys.* **1997**, *38*, 39.

(65) Pujols-Ayala, I.; Sacksteder, C. A.; Barry, B. A. *J. Am. Chem. Soc.* **2003**, *125*, 7536-7538.

(66) Morita, T.; Kimura, S. *J. Am. Chem. Soc.* **2003**, *125*, 8732-8733.

(67) Morita, T.; Kimura, S.; Kobayashi, S.; Imanishi, Y. *J. Am. Chem. Soc.* **2000**, *122*, 2850-2859.

(68) Schenning, A. P. H. J.; v. Herrikhuyzen, J.; Jonkheijm, P.; Chen, Z.; Wurthner, F.; Meijer, E. W. *J. Am. Chem. Soc.* **2002**, *124*, 10252-10253.

(69) Eley, D. D.; Spivey, D. I. *Trans. Faraday. Soc.* **1962**, *58*, 611-615.

(70) Murphy, C. J.; Arkin, M. R.; Jenkins, Y.; Ghatlia, N. D.; Bossmann, S. H.; Turro, N. J.; Barton, J. K. *Science* **1993**, *262*, 1025-1029.

(71) Stemp, E. D. A.; Arkin, M. R.; Barton, J. K. *J. Am. Chem. Soc.* **1995**, *117*, 2375-2376.

(72) Holmlin, R. E.; Stemp, E. D. A.; Barton, J. K. *J. Am. Chem. Soc.* **1996**, *118*, 5236-5244.

(73) Stemp, E. D. A.; Arkin, M. R.; Barton, J. K. *J. Am. Chem. Soc.* **1997**, *119*, 2921-2925.

(74) Dandliker, P. J.; Holmlin, R. E.; Barton, J. K. *Science* **1997**, *275*, 1465-1468.

(75) Arkin, M. R.; Stemp, E. D. A.; Holmlin, R. E.; Barton, J. K.; Hormann, A.; Olson, E. J. C.; Barbara, P. F. *Science* **1996**, *273*, 475-480.

(76) Lewis, F. D.; Wu, T.; Zhang, Y.; Letsinger, R. L.; Greenfield, S. R.; Wasielewski, M. R. *Science* **1997**, *277*, 673-676.

(77) Fukui, K.; Tanaka, K. *Angew. Chem. Int. Ed.* **1998**, *37*, 158-161.

(78) Meggers, E.; Kusch, D.; Spichty, M.; Wille, U.; Giese, B. *Angew. Chem. Int. Ed.* **1998**, *37*, 460-462.

(79) Marcus, R. A. *Annu. Rev. Phys. Chem.* **1964**, *15*, 155-196.

(80) Kestner, N. R.; Logan, J.; Jortner, J. *J. Phys. Chem.* **1974**, *78*, 2148-2166.

(81) Newton, M. D.; Sutin, N. *Annu. Rev. Phys. Chem.* **1984**, *35*, 437-480.

(82) Efrima, S.; Bixon, M. *Chem. Phys.* **1976**, *13*, 447-460.

(83) Ulstrup, J.; Jortner, J. *J. Chem. Phys.* **1975**, *63*, 4358-4368.

(84) Jortner, J. *J. Chem. Phys.* **1976**, *64*, 4860-4867.

(85) Bernd Giese, S. W. *Angew. Chem.* **2000**, *39*, 3490-3491.

(86) Giese, B. *Annu. Rev. Biochem.* **2002**, *71*, 51-70.

(87) Giese, B.; Amaudrut, J.; Kohler, A.-K.; Spormann, M.; Wessely, S. *Nature* **2001**, *412*, 318-320.

(88) Meggers, E.; Michel-Beyerle, M. E.; Giese, B. *J. Am. Chem. Soc.* **1998**, *120*, 12950-12955.

(89) Schuster, G. B. *Long-Range Charge Transfer in DNA;* Top. Curr. Chem. Vols 236 and 237; Springer: New York, 2004.

(90) Barnett, R. N.; Cleveland, C. L.; Joy, A.; Landman, U.; Schuster, G. B. *Science* **2001**, *294*, 567-571.

(91) Conwell, E. M.; Rakhmanova, S. V. *Proc. Natl. Acad. Sci.* **2000**, *97*, 4556-4560.

(92) Henderson, P. T.; Jones, D.; Hampikian, G.; Kan, Y.; Schuster, G. B. *Proc. Natl. Acad. Sci.* **1999**, *96*, 8353-8358.

(93) Rakhmanova, S. V.; Conwell, E. M. *J. Phys. Chem. B* **2001**, *105*, 2056-2061.

(94) Schuster, G. B. *Acc. Chem. Res.* **2000**, *33*, 253-260.

(95) Jortner, J.; Bixon, M.; Langenbacher, T.; Michel-Beyerle, M. E. *Proc. Natl. Acad. Sci.* **1998**, *95*, 12759.

(96) Sommer, B.-S.; Jortner, J. *J. Chem. Phys.* **1968**, *49*, 3919-3928.

(97) Levine, M.; Jortner, J.; Szoke, A. *J. Chem. Phys.* **1966**, *45*, 1591-1604.

Chapter 2 Molecular Chirality and Charge Transfer through Self-Assembled Scaffold Monolayers

This work has been published as J. J. Wei, C. Schafmeister, G. Bird, A. Paul, R. Naaman, D. H. Waldeck, *J. Phys. Chem. B.* **2006**, *110*, 1301-1308

2.1 Abstract

The effect of molecular chirality on electron transmission is explored by photoelectrochemistry. Thiol-terminated chiral scaffold molecules containing a porphyrin chromophore were self-assembled on gold surfaces to form a monolayer. Incorporation of the SAM-coated gold into an electrochemical cell and illumination with visible light generated a cathodic photocurrent. When using circularly polarized light, the photocurrent displayed an asymmetry (different magnitude of photocurrent for right versus left polarization) that changed with the molecular chirality (left or right handedness of the scaffold). A symmetry constraint on the electronic coupling between the porphyrin and the organic scaffold is proposed as a possible mechanism for the photocurrent asymmetry.

2.2 Introduction

The primary process of electron transfer underlies many chemical and biological reactions and is of primary importance in many technologies. Consequently, the nature of electron transfer (its dependence on energetics, nuclear degrees of freedom, and electronic coupling) has been under experimental and theoretical study for many years.[1,2] Despite these efforts, little attention has focused on the influence of molecular chirality on electron transfer. This work examines the effect of molecular chirality on the

photocurrent of film coated electrodes. On a fundamental level, spin-polarized electrons have been used to perform chemistry and are implicated in the origin of chiral selectivity in biology.[3] On a technological level, molecular chirality can be used to introduce a new control parameter for spin-sensitive devices.

Naaman reported the first investigation of spin dependent electron transmission through thin chiral films of stearoylysine[4] and more recently observed an asymmetry for electron transmission through monolayers of L (or D) polyalanine films.[5] The magnitude of the effect is 10^3 to 10^4 times larger than the chiral selectivity found for the interaction of polarized electrons with molecules that are not organized into two-dimensional arrays.[6-17]

In photoemission through an organic monolayer film, the electron wavefunction can be delocalized among many chiral molecules in the film, whereas tunneling electrons are more localized. Hence, it is interesting to ask if such large effects are possible for electron tunneling. Spin polarized tunneling has been observed in Metal-Oxide-GaAs (MOS) structures with an asymmetry of the order of 1%.[18] In those studies the polarized distribution of carriers is generated in the GaAs by circularly polarized light and tunneling occurs through a thin Al_2O_3 (2 to 20 nm) on Al. In recent work spin polarized electrons were selectively transmitted between two quantum dots through organic molecule.[19] Those findings show that it is possible to create the polarized distribution of charge carriers and observe asymmetry in electron tunneling.

This study investigates the photocurrent, induced by circular polarized light, through organic monolayer films on Au electrodes that are immersed in an electrochemical cell. The films are composed of a chiral scaffold molecule, which is

linked to the Au by a cysteine moiety, and presents a porphyrin chromophore to the solution. Although related systems have been studied previously (*e.g.*, Morita et al.[20] placed helical peptides containing a carbazolyl chromophore on gold electrodes), the effects of molecular chirality and light polarization were not explored. Under photoexcitation of the porphyrin, an electron is transferred to an acceptor (*e.g.*, methylviologen), and the resulting cation of the porphyrin is reduced by the gold electrode. By measuring the dependence of the photocurrent on the polarization of the light field and correlating it with the scaffold's chirality, a preference for electron tunneling of one handedness is indicated.

2.3 Experimental

Reagents and Materials Preparation: Scheme 2.1 shows the chiral scaffold molecules (L-Cys-(pro4(2S4S))$_4$-Porph (**S1**), D-Cys-(pro4(2R4R))$_4$-Porph (**R1**)) with their covalently linked porphyrin chromophore. The compounds were prepared in the manner reported previously.[21]

Solid phase synthesis was performed in a 1.5 mL disposable polypropylene reaction column, connected to a three-way valve equipped with vacuum and argon for mixing. Dichloromethane (DCM) used in coupling reactions was distilled over calcium hydride. Dry grade of dimethylformamide (DMF) from Aldrich was used for coupling. Diisopropylamine (DIPEA) was distilled under nitrogen sequentially from ninhydrin and potassium hydroxide and stored over molecular sieves. *O*-(7-azabenzotriazol-1-yl)-*N,N,N',N'*-tetramethyluronium hexafluorphospate (HATU) was obtained from Acros. All solid phase reactions were mixed by bubbling argon up through the reactor, allowing for mixing and an inert atmosphere over the reaction. HPLC analysis was performed

using a Hewlett-Packard Series 1050 instrument equipped with a Varian Chrompack Microsorb 100 C_{18} column (5μm packing, 4.6 mm x 250 mm) or a Hewlett-Packard Series 1100 instrument equipped with a Waters Xterra MS C_{18} column (3.5μm packing, 4.6 mm x 100 mm) and a diode-array detector.

The HPLC purified product was collected and characterized spectroscopically. The ES-MS displayed a mass to charge ratio of 1345.5 for both enantiomers. Circular dichroism spectroscopy was used to characterize the configuration of the scaffold molecules in solution. Room temperature circular dichroism spectra were obtained from a JASCO J-715 Spectrometer using a cell with a 1 cm optical path length.

Film and Electrode Preparation: The molecules were self-assembled to form a monolayer thick film on evaporated gold slides (purchased from EMF Corp.). The Au

Scheme 2.1

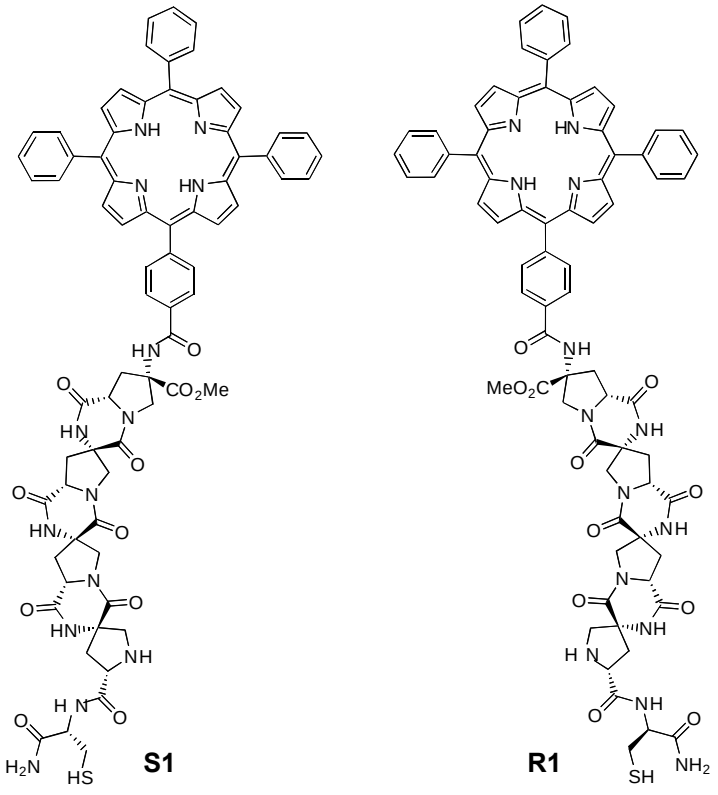

Table 2.1 Summary of contact angle and thickness of the scaffold porphyrin derivatives SAMs at gold electrodes. Errors are one-standard deviation.

	SAMs of **S1**	SAMs of **R1**
Contact Angle (degree)	78 ± 5	76 ± 5
Thickness (nm)	2.7 ± 0.5	3.2 ± 0.4

slides were 0.7 inch x 0.7 inch x 0.062 inch in size and consisted of 100 nm Au on top of a 50 nm thick Ti binder layer on float glass. The gold slides were cleaned by immersion into "piranha" solution (1:3 of H_2O_2 and 98% H_2SO_4) (**caution: this solution is dangerous**) for a few minutes, then rinsed by a large amount of deionized water (18MΩ), followed by ethanol, and subsequently dried under an argon gas stream. For adsorption, the molecules were dissolved in a solution with 80%ACN/20%H_2O/0.1%TFA acid at a concentration of about 100 μM. The gold slides were incubated for 1-2 days for pure monolayer preparation at room temperature. These SAM coated gold slides were rinsed with 80%ACN/20%H_2O/0.1%TFA acid solvent before use. To prepare a mixed SAM of the scaffold/porphyrin and an alkanethiol $C_{12}(HS(CH_2)_{11}CH_3)$, the pure scaffold SAM gold slide was immersed in a 80%ACN/20%H_2O/0.1%TFA solution with 1 mM concentration of C_{12} alkanethiol for a few (2-6) hours.

Table 2.1 reports the static contact angles (measured by Gaertner L-117 Null ellipsometer) formed with pure water and the ellipsometrically determined thickness of SAMs composed of the 4-mer chiral scaffold porphyrin SAMs. The SAM coated gold surfaces are more hydrophobic than the bare gold slide's contact angle (60±5º), presumably because of the hydrophobic nature of the terminal porphyrin. No difference in hydrophobicity with the chirality of the scaffold could be detected. The ellipsometric

thicknesses for the films, 2.7± 0.5 nm for the 4-mer SS and 3.2± 0.4 nm for the 4-mer RR scaffold, are less than the length (3.1 nm) of optimized (energy minimized) 4-mer scaffold porphyrins. It was found that the thickness of the scaffold SAM increased if it was incubated in a 1 mM C_{12} alkanethiol at 80%ACN/20%H_2O/0.1%TFA solution for a few hours. For example, the thickness of a pure 4-mer SS scaffold SAM (2.8 nm) increased to 3.2 nm after 6 hours in a 1 mM C_{12} alkanethiol at 80%ACN/20%H_2O/0.1%TFA solution, and the contact angle of water increased from 80º to 92º. These results suggest that the scaffold molecules may not be compactly assembled at the surface, perhaps because of steric hindrance around the porphyrins.[22]

The UV-visible absorption spectra of the free porphyrin and the porphyrin-scaffolds (**S1** and **R1**) were measured with an Agilent 8435 single beam UV-visible spectrometer. The surface UV-visible absorption spectroscopy was performed by placing a gold coated (200 Å on glass, EMF Corp.) transparent slide in the light beam pathway and measuring the transmission.

Electrochemical Measurements: The compactness of the monolayer films was probed by investigating how well they block faradaic current of a solution redox couple. A CHI 618B potentiostat was used for the cyclic voltammetry of electrodes modified with the porphyrin SAMs. The three electrode cell was composed of a platinum spiral counter electrode, an Ag/AgCl (3 M NaCl) reference electrode, and a porphyrin modified Au slide as a working electrode. The blocking behavior of the SAM modified electrodes were performed in a 0.5 M KCl and 1mM of $[Fe(CN)_6]^{3-/4-}$ solution.[23] While the bare gold electrode displayed a typical faradaic response, the coated gold electrodes showed a reduced current, which is typical of insulating SAM coated electrodes and indicates that

the films inhibit the penetration of the ferricyanide and ferrocyanide redox species to the metal surface (see Supporting Information). A better blocking behavior was observed from the **R1** coated electrodes than the **S1** coated electrodes, implying a more tightly packed **R1** film than **S1** film.

The porphyrin coverage on the electrodes was estimated by performing cyclic voltammetry in 0.1 M of n-Bu_4NPF_6 in CH_2ClCH_2Cl or CH_2Cl_2 solution bubbled with argon gas and integrating the area under the faradaic peak to obtain the total charge.

Photocurrent measurements of the porphyrins were performed using a CHI 618B potentiostat. The same three electrode cell was used for the current measurement and the potential applied on the working electrode was controlled. For cathodic photocurrent measurements, the electrochemical cell contained a 0.1 M Na_2SO_4 aqueous electrolyte solution with 10 mM MV^+ and ambient oxygen as electron acceptors. For anodic photocurrent measurements, 0.1 M Na_2SO_4, 0.1% TFA aqueous solution with bubbled argon gas was used as an electrolyte solution and contained 50 mM TEOA as an electron donor. For the wavelength dependent photocurrent measurements, a tungsten-halogen lamp of 25 mW was used as a light source and band pass filters were used to control the wavelength from 200 nm to 800 nm. The energy of irradiation was measured by a power/energy meter (Newport Research Corporation (USA), Model 1825C).

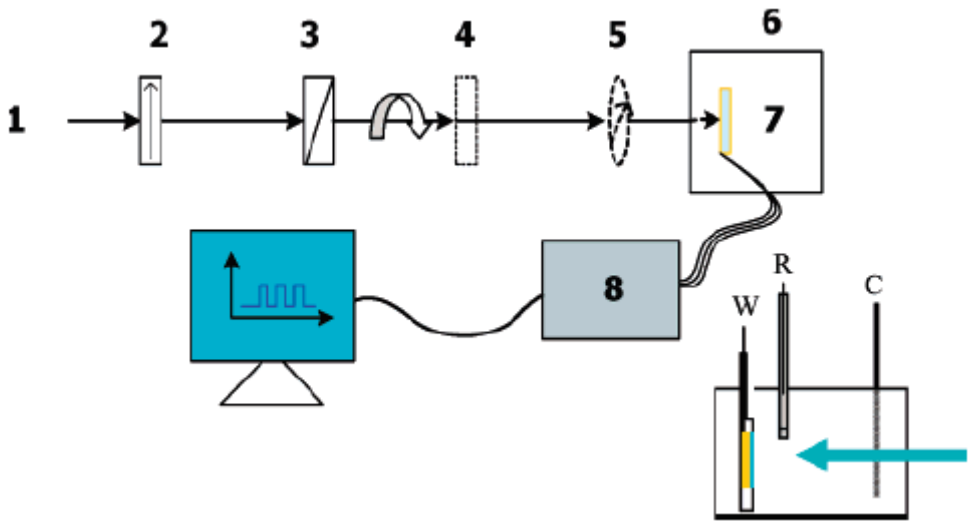

Figure 2.1 Schematic diagram showing the apparatus for measuring the photocurrent with different light polarization. The components are (1) the He-Cd laser source, (2) a linear polarizer, (3) a tilted quarter wave plate as circular polarizer, (4) a linear polarizer, if needed in the control experiments, (5) an optical power meter, (6) a Faraday cage, (7) an electrochemical cell, and (8) a potentiostat. Number 7 is a three-electrode cell as shown, W is a working electrode, R is the reference electrode, Ag/AgCl, and C is the counter electrode, Pt wire.

For the polarization studies, a He-Cd laser (Omnichrome) source with wavelength 435 nm was used for excitation, by way of a window in the electrochemical cell that was directly opposite to the gold slide electrode (see inset of Figure 2.1). The optical arrangement applied excitation with left/right circular polarized light or linear polarized light through use of a tilted quarter-wave plate (Alphalas Gmbh, Germany) behind a linear polarizer.[24,25] For each measurement, the average power was measured and recorded before and after the photocurrent measurement. Between measurements, the power meter was used to block the light beam. The photocurrent was recorded by a PC through a CHI 618B potentiostat.

2.4 Results

Spectra of Scaffold Molecules: Figure 2.2A shows the absorption spectra of the **S1** and **R1** compounds in 80%ACN/20%H_2O/0.1%TFA acid solution. No significant peak shift

is found in the Soret bands (λ_{max}=435 nm) and Q bands (649 nm for original porphyrin and 650 nm for scaffold porphyrins) in comparison to the free porphyrin (H_2TPP). This result suggests no significant change of the porphyrin electronic structure in **S1** and **R1**. These results are consistent with previous semiempirical calculations[26] and experiments.[27]

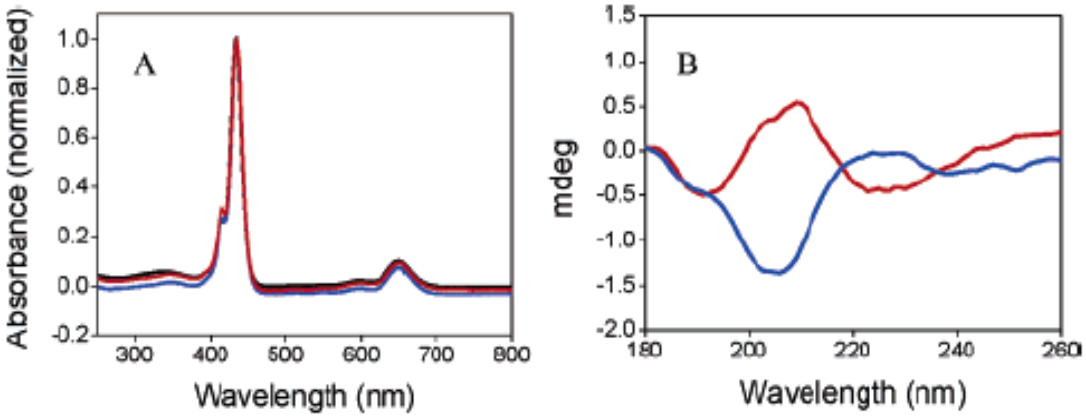

Figure 2.2 (A) Absorption spectra of porphyrin only (black), R1 (red), and S1 (blue) scaffold with porphyrins attached in 80%ACN/20%H_2O/0.1%TFA acid solvent. (B) CD spectra of chiral scaffold molecules: (a) red (S1, SS scaffold) and (b) blue (R1, RR scaffold). The UV-vis absorbance is normalized to the Soret band.

Figure 2.2B shows CD spectra of the two porphyrin scaffolds in the far UV region (180-260 nm). It is well known that the transitions in a polypeptide involve the nonbonding electrons on the oxygen of the carbonyl group and the nearest nitrogen atoms. These transitions are n →π* and π →π*. Normally, the n →π* transition occurs at lower energy and depends on the extent of hydrogen bonding to the oxygen lone pairs, whereas the π →π* transition is dominated by the carbonyl π-bond and occurs at higher energies, ranging from 190 to 210 nm with change in conformation.[28,29] Hence the transition at 225 nm is assigned to the n →π* transitions in the scaffold chain, and the

peak centered at 205 nm is assigned to the $\pi \rightarrow \pi^*$ transitions.[28,29] The complementary signals of the **R1** and **S1** scaffold reflect the different chirality of these bridges.

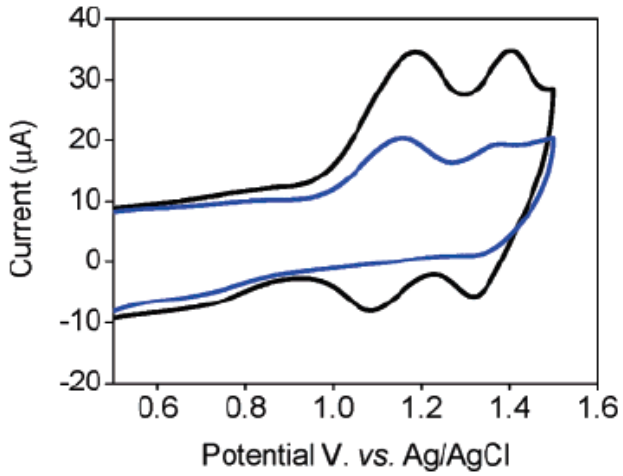

Figure 2.3 Cyclic voltammograms of porphyrin scaffold (**R1**) film on a gold slide electrode; the experiment was carried out in n-Bu_4NPF_6/CH_2Cl_2 solution with saturated argon gas. The scan rate is 0.4 V/sec (black) and 0.2 V/sec (blue), Pt is the counter electrode, and Ag/AgCl is the reference electrode.

Voltammetry of SAMs: Figure 2.3 shows voltammograms for the porphyrin SAMs that were obtained at a scan rate of 0.4 V/sec and 0.2V/sec in a 0.2 M n-Bu_4NPF_6/CH_2Cl_2 solution. The porphyrin displays two strong oxidation peaks near 1.12 V and 1.36 V vs Ag/AgCl reference electrode at a smaller scan rate (0.2 V/sec). These two oxidation peaks are a characteristic signature for the porphyrin. The lack of reduction peaks at low scan rates arises from the instability of the oxidized porphyrin radicals in the solution.[30] If multiple scans are performed at a slow scan rate the two oxidation peaks become significantly weaker after about 30 minutes and finally disappear, implying desorption or an inactivity of the resultant scaffold porphyrins. Similar voltammetry was observed from both **S1** and **R1** films (exposure area is 0.3 cm^2).

The surface concentration (electrochemical active species) of porphyrin was estimated by the amount of charge in the first oxidation peak and by the relationship between the peak current and the scan rate.[23] The two methods gave compatible results. Integration of the current peaks provide coverages (after correcting for surface roughness factor 1.2) of 4.6± 0.2 $\times 10^{-11}$mol/cm^2 for **S1** and 6.7±0.15 $\times 10^{-11}$ mol/cm^2 for **R1**, almost the same as the coverage of alkane linked porphyrin on ITO[31] and gold electrodes.[32] This coverage is a lower bound, since not all porphyrins at the surface are necessarily electrochemically active, but is consistent with STM images of the film (see Supporting Informations). Assuming that the porphyrin is in a planar conformation and has a circular shape with a 17.0 Å diameter,[32] each porphyrin has an area of about 2.26 nm^2. For a compact porphyrin monolayer, the calculated coverage should be about 7.3×10^{-11}mol/cm^2. These results indicate that the **R1** material has a slightly more compact monolayer structure than the **S1** film (90% versus 60% of a close packed film), consistent with the ellipsometric thickness measurements. The reason for this difference in coverage was not identified.

Action Spectrum of SAMs: The action spectrum of scaffold porphyrins at gold electrodes was obtained by measuring the cathodic photocurrent under irradiation with light, whose wavelength was selected with bandpass filters. Figure 2.4 shows the photocurrent action spectrum of an **R1** SAM, and the inset shows its absorbance spectra under different conditions. The greatest photocurrent is observed in the wavelength range of 400 to 450 nm, the Soret band region. The inset shows the spectrum of the porphyrin in 80%ACN/20%H_2O/0.1%TFA acid solvent (black curve), and the spectrum of the **R1** SAM in contact with the 80%ACN/20%H_2O/0.1%TFA acid solvent (blue curve). The

films display a broadened Soret band (compared to the solution porphyrin). The photocurrent action spectrum and the absorption spectrum of scaffold porphyrins at the gold surface demonstrate that the porphyrin is the photoactive species responsible for the photocurrent generation.

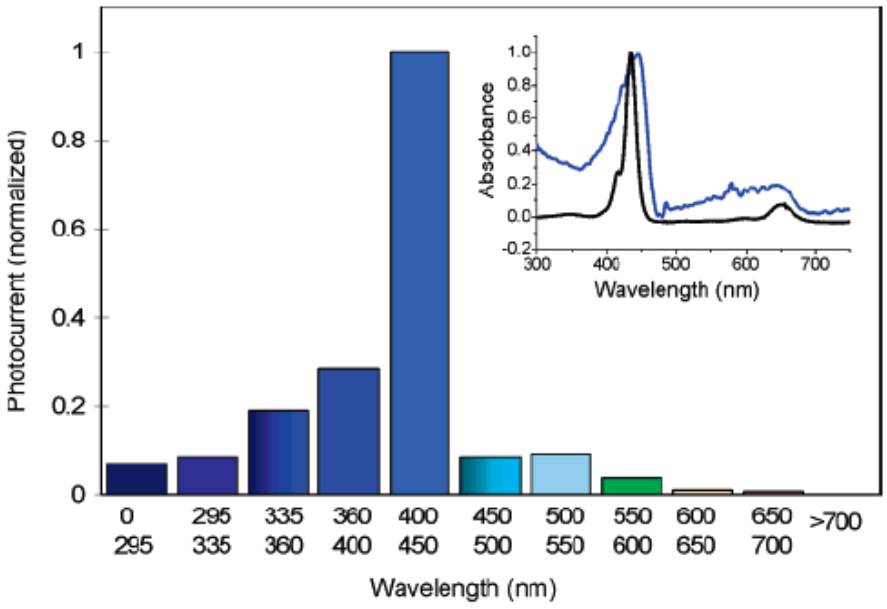

Figure 2.4 A photocurrent action spectrum; the photocurrent is normalized to the maximum magnitude. The inserted graphic is the UV-visible spectra of scaffold porphyrins (R1) in 80%ACN/20%H_2O/0.1%TFA acid solvent (black curve), the scaffold assembled at a gold coated transparent slide in a transmission mode in 80%ACN/20%H_2O/0.1%TFA acid solvent (blue curve), The spectra are normalized to the Soret band absorbance for comparison; the actual absorbance of the surface spectra is about 0.05 at surface.

The broadened Soret band of the porphyrins in the SAMs may have a number of possible origins, such as incomplete protonation of the free tetraphenylporphyrins[26,27] or interactions between porphyrins in the layer, either side-by-side (J aggregation, red shift) or face-to-face (H aggregation, blue shift).[33-36] The Soret band (447) nm of the porphyrin scaffold films in 80%ACN/20%H_2O/0.1%TFA acid solvent is shifted to the red by about 12 nm, and is broadened compared to the spectra in solution. This red shift suggests a

strong side by side interaction between porphyrins and the broadened peak suggests the presence of both aggregates and porphyrin monomers in the monolayer, which have been reported by others.[37]

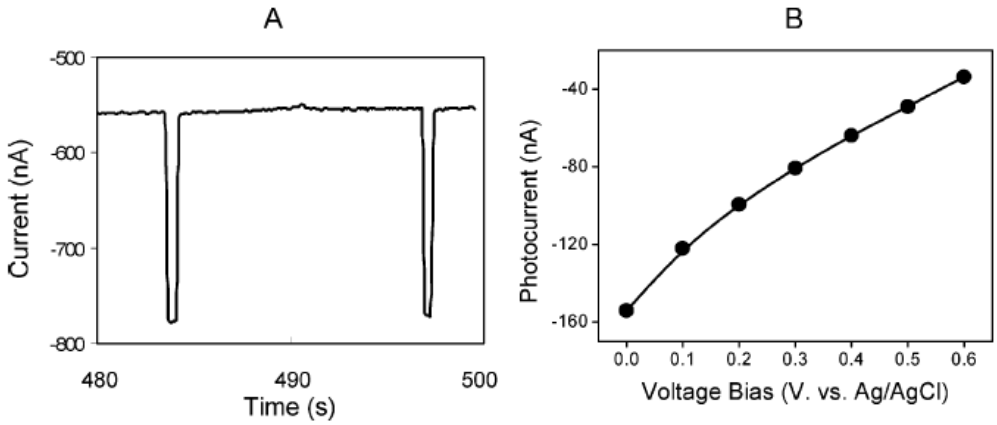

Figure 2.5 (A) Representative photoelectrochemical responses from the SS scaffold porphyrin SAM modified Au electrode at an applied voltage bias of 0.0 V in a three-electrode cell (counter electrode: Pt, reference electrode: Ag/AgCl). (B) The voltage bias dependent photocurrents for the Au-Porphyrin/$MV^{+/2+}$/Pt system. The excitation wavelength is 435 nm and the average power is 1.35 mW. The photocurrent in panel B is defined as $I_{photo}=I_{on}-I_{off}$

Photoelectrochemical Characterization: Photoelectrochemical measurements were performed in a 0.1 M Na_2SO_4 aqueous electrolyte solution containing 10 mM methyl viologen (MV^+) and saturated oxygen as electron acceptors. A cathodic photocurrent from the porphyrin modified gold electrode was observed immediately upon irradiation by a 435 nm laser beam with a power of 1.35 mW at an applied voltage bias of 0.0 V versus Ag/AgCl (3.0 M KCl) reference electrode. A time profile of the raw photocurrent for the **S1** SAM is shown in Figure 2.5A. The dark current in cathodic photocurrent measurements changes positively with the voltage bias change from 0 to 0.6 V, indicating that the **S1** SAM is not so compact. Nevertheless, the magnitude of photocurrent was stable, reproducible, and consistent with analogous systems reported earlier.[37] The

photocurrent was linear in light intensity for laser powers <3.0 mW. Figure 2.5B shows the voltage dependence of the photocurrent, which decreases monotonically with increasing positive bias. These results demonstrate that the electron flows from the gold electrode to the electrolyte through the scaffold porphyrin SAMs.

Similar wavelength responses and voltage dependencies were found for the **R1** and **S1** SAMs at gold electrodes. In addition, no photocurrent was observed from the bare gold electrodes under the irradiation. The photoelectrochemical characterization confirms that excitation of the porphyrin is responsible for photocurrent generation.

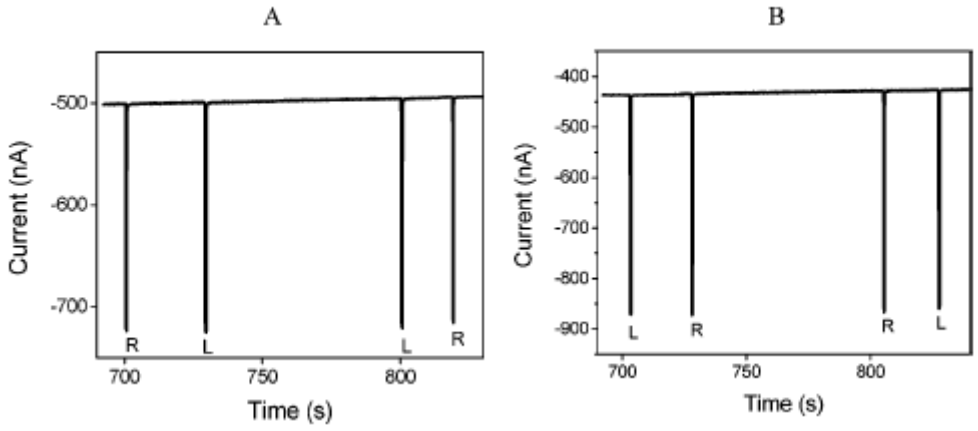

Figure 2.6 Representative photocurrent signals generated under circular polarized light for (A) **S1** and (B) **R1** scaffold porphyrins at gold electrodes. R and L represent right circularly polarized (RCP) excitation and left circularly polarized excitation (LCP), respectively. The voltage bias is 0.0 V; the incident power is between 1.3 and 1.4 mW.

Asymmetry of Photocurrent: To study the effect of molecular chirality and electron helicity on the electron transfer, photocurrent generated under irradiation with circularly polarized light (either right circularly polarized light, RCP, or left circularly polarized light, LCP) was examined for both **S1** and **R1** SAMs. Figure 2.6 shows representative photocurrents generated under illumination with circular polarized light for the two chiral scaffold pophyrins at gold electrodes. The RCP or LCP polarizations were obtained by

rotating a λ/4 wave plate at a specific tilt angle (see experimental section for details). The incident light intensity was measured for every illumination. For the **S1** scaffold porphyrins, the magnitude of photocurrent under LCP irradiation is slightly larger than that under RCP irradiation as shown in Figure 2.6A. In contrast, the **R1** scaffold porphyin film has a larger photocurrent under RCP irradiation than that under LCP irradiation. Although the preference is small, less than 1%, it was highly reproducible for a given sample and stable over a period of many hours. In some cases, measurements were performed over more than one day on the same electrode and found to be reproducible.

About ten electrodes for each sample type (**R1** and **S1**) were studied under the same conditions and the propensities of the asymmetry in photocurrents were measured. Control experiments, using a linearly polarized laser beam, showed no asymmetry.

Asymmetry Factor Determination: An asymmetry factor *A* for the photocurrent was defined as

$$A = \frac{j(\sigma+) - j(\sigma-)}{j(\sigma+) + j(\sigma-)} \tag{2.1}$$

in which *j(σ+)* and *j(σ-)* are photocurrents (normalized to light power) for RCP and LCP illumination at the same electrode, respectively. The asymmetry factor was calculated for each RCP and LCP irradiation pair. The **S1** scaffold (4-mer) gave an average asymmetry factor of -0.0048, and the **R1** scaffold (4-mer) gave an average asymmetry factor of +0.0054.

Figure 2.7 plots the asymmetry factor obtained for all of the experiments. Panels a and b show the distribution (a descending sort) of asymmetry factors for **R1** and **S1** films, respectively. The asymmetry factors of the **R1** scaffold range from -0.017 to 0.034 and

most of them are positive values, whereas the asymmetry factor of the **S1** scaffold range from –0.033 to 0.012 and most of them are negative values. Panels c and d show a histogram (bin size of 0.001) for the asymmetry factors. A Gaussian function (solid curve in c and d) is fit to the distribution. This fit yields an average value of 0.004 and a standard deviation of 0.006 for the asymmetry factor of the **R1**

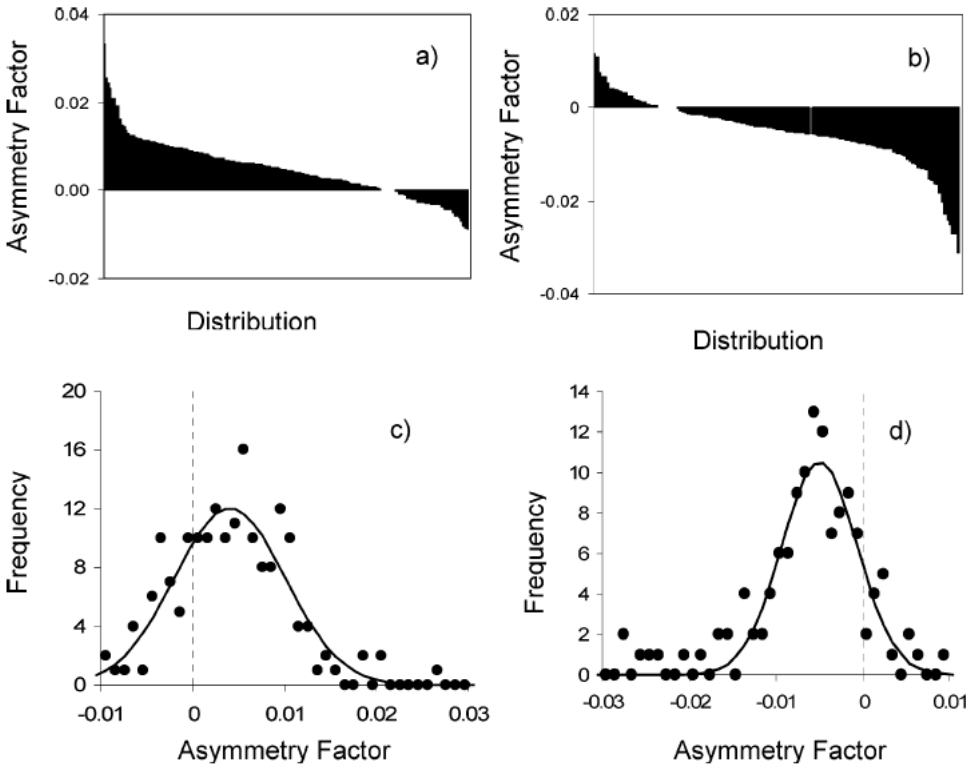

Figure 2.7 Distributions of asymmetry factors and statistical analysis of the helicities. Panels a and b present the distributions of the asymmetry factors in a descending sort for **R1** and **S1** scaffold porphyrin electrodes, respectively, while panels c and d are the histograms of the number of observations vs the observed ranges of asymmetry factors, corresponding to a and b respectively.

scaffold, and it yields an average value of -0.005 and a standard deviation of 0.004 for the **S1** scaffold. This analysis gives an average asymmetry factor of 0.004±0.002 for the **R1**

scaffold and -0.005±0.001 for the **S1** scaffold, in which the error in the mean value is the 95% confidence limit.[38]

2.5 Discussion

Mechanism of Photocurrent Generation and Electron Transfer: The action spectrum (Figure 2.4) demonstrates that the photocurrent is generated by illumination of the porphyrin Soret band. The mechanism of photocurrent generation from the porphyrin at gold electrodes was established by Imahori et al.,[30,37] and the current findings are consistent with that mechanism.

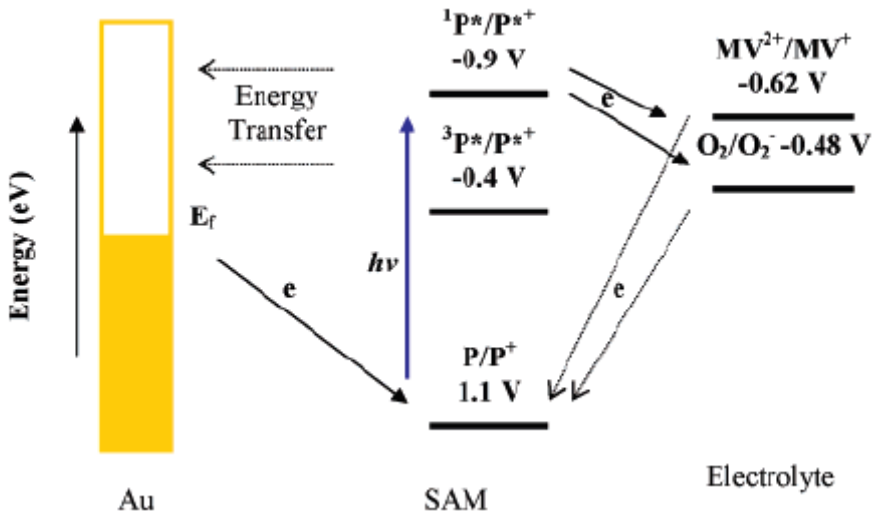

Figure 2.8 Diagram showing the mechanism of cathodic photocurrent; P represents the porphyrin attached.

Figure 2.8 summarizes the mechanism for cathodic photocurrent generation. Approximating the excited singlet and triplet state energies (relative to the ground state) of porphyrin at the gold surface by their solution values, their redox potentials are estimated to be -0.9 V for ^{1}TPP*/TPP$^+$ and -0.4 V for ^{3}TPP*/TPP$^+$, using a potential of 1.1 V versus Ag/AgCl for the ground state. In the cathodic photocurrent measurements,

the electron acceptors, methyl viologen (MV^{2+}/MV^{+}) and oxygen (O_2/O_2^{-}), have redox potentials of -0.62 V and -0.48 V, respectively. Thus the photoinduced electron transfer only occurs from the excited singlet porphyrin to MV^{2+} and/or O_2. The reduced acceptors, MV^{+} and O_2^{-}, can either reduce the porphyrin cation radicals or diffuse to the Pt counter electrode to generate a cathodic photocurrent. Those cation radicals that do not undergo recombination with the electron acceptors are reduced by electrons from the gold electrode. This phenomenon explains why the magnitude of the cathodic photocurrent depends on the applied voltage.

In addition to the efficiency of charge transfer to the electron acceptor and its subsequent escape, the magnitude of the photocurrent depends on the efficiency of electron tunneling through the scaffold linker[39-41] and energy transfer quenching of the excited singlet porphyrin,[30,37] by the metal electrode or nearby porphyrin. Previous studies of H_2TPP, both in various organic solvents[42,43] and surfaces,[37,44,45] indicate that the lifetime of the excited singlet state of H_2TPP is tens of picoseconds when linked by an alkanethiol to the metal surface, compared to 10 nanoseconds in bulk solvents. The lifetime of excited singlet electrons may play an important role, not only in the photocurrent generation, but also the relative importance of the interaction between the 'helicity' of the porphyrin excited state and the scaffold's chirality. In particular, the fast population relaxation of the porphyrin means that the photocurrent arises from short-lived excited states that may retain significant polarization from the exciting light field. Possible mechanisms for the photocurrent's dependence on the electron helicity relative to the bridge chirality are discussed below.

Mechanism for Asymmetry: The mechanism for photocurrent generation does not explain the mechanism for the photocurrent asymmetry. Because the asymmetry is measured for a particular film coated electrode, be it composed of an **R** or an **S** bridge, variations in the film coverage and compactness between the bridge types alone cannot explain the asymmetry. Even though the SS film is more open than the RR film, the asymmetry factors are similar in magnitude (although shifted in sign) implying that defects in the film or access to the metal surface by the viologen is not important for the asymmetry. In addition, linear polarization studies reveal no asymmetry, which implies that the orientation distribution of the chromophores on the surface is isotropic in the plane of the layer (at least on the length scale probed by the excitation light), implying that geometric/ steric constraints on the access to porphyrin moieties do not determine the asymmetry. Two possible explanations for the asymmetry: (1) dependence of tunneling probability on wavefunction symmetries and (2) induced circular dichroism from packing in the layer.

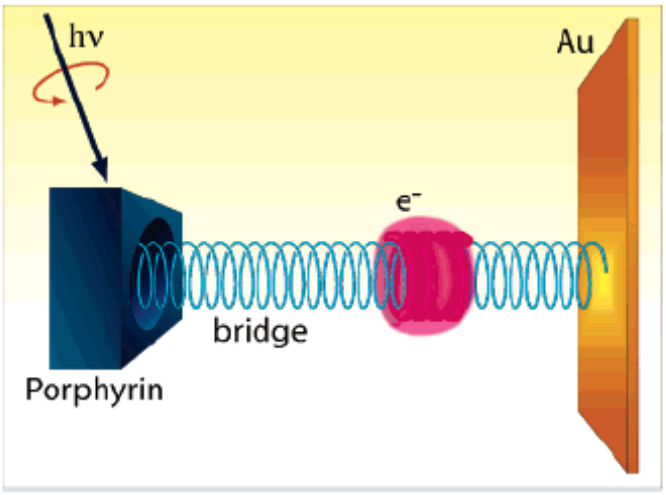

Figure 2.9 The schematic diagram illustrates the mechanism for photocurrent asymmetry. The light field creates a polarized electron distribution on the porphyrin, and this polarization affects the electron transfer probability to the electrode because the insulating bridge is chiral.

1) Electronic Helicities of Excited Porphyrins: If a molecule is electronically excited by absorption of a photon, the molecules angular momentum changes because the photon carries angular momentum.[46] The transfer of the light field's circular polarization to the ensemble of excited molecules is well established, e.g., circular polarized molecular fluorescence[47,48] and circular dichroism spectroscopy. Other work has demonstrated the generation of electron spin polarization by circularly polarized light in photoemission at surfaces,[49] electron scattering from molecules in the gas phase,[50,51] and other fundamental studies.[52-54] In this work, the asymmetry of photocurrent, generated by irradiation of porphyrin chromophores with circular polarized light, could arise from electron transfer (electron tunneling) that depends on the charge carrier (electron or hole) polarization. Figure 2.9 illustrates the essential idea that the circularly polarized light excites the porphyrin molecule, promoting an electron to the LUMO with given handedness, or polarization. Hence, an electron with the same handedness can be transferred from the gold substrate to fill the hole in the porphyrin HOMO. When the electron handedness and the chirality of the bridge match, the electron transfer is more efficient.

Electron helicity can be defined as:

$$C = 0.5\frac{\sum_{\ell} P(m_{\ell^+})}{\sum_{\ell} P(m_{\ell^+}) + \sum_{\ell} P(m_{\ell^-})} + 0.5\frac{P(m_{S^+})}{P(m_{S^+}) + P(m_{S^-})} \qquad (2.2)$$

in which P(m_{ℓ^+})and P(m_{ℓ^-}) are the population in the m_ℓ angular momentum states with positive sign or negative sign respectively, and P(m_{S^+}) and P(m_{S^-}) are the population of spin ½ and spin -½ states respectively. If the spin-orbit coupling is significant, the relevant populations are of the states m_{j^+} and m_{j^-}, related to j states (j=ℓ+s) with positive

or negative sign respectively. For the free porphyrin, the spin-orbit coupling is not expected to be so important.

When the porphyrin is excited with circular polarized light, the orbital that is depopulated, hole, is polarized and its polarization, characterized by an m_ℓ state $|m_\ell\rangle$, depends on the circular polarization of the photon. The probability that the photogenerated hole is filled by a tunneling electron will depend on the symmetry of the electron wavefunction. When the electron tunnels through a chiral bridge, the chiral structure of the bridge ensures that certain electron helicities tunnel more efficiently than others, hence the electron wave is polarized and characterized by certain electron helicity, C. In the absence of spin-orbit coupling, the electron wave can be described as: $\Phi = \sum_\ell a_\ell |m'_\ell\rangle$ in which the coefficients a_ℓ for the $|m'_\ell\rangle$ states depend on the handedness of the bridge. In the idealized case the left-handed bridge will only transmit m'_ℓ of one sign, and a right-handed bridge the opposite sign. The probability for an electron to be transferred from the metal to the hole state on the acceptor depends on the overlap, *F*, between the hole state and Φ. Therefore, $F = \langle m_\ell | \Phi \rangle = \left\langle m_\ell \left| \sum_\ell a_\ell m'_\ell \right. \right\rangle$. For the currently studied case, the axis of quantization is not the same for the two subsystems (chiral bridge and porphyrin ring) and therefore one must account for the projection of $|m_\ell\rangle$ on the axis of the chiral bridge.

The above considerations should apply if one assumes that spin-orbit coupling is negligible in this system. In the case that it cannot be ignored, one has to consider $j=\ell+s$ as the valid quantum number.

2) Circular Dichroism in the Film: Although the Soret bands (B bands) for the **S1** and **R1** porphyrins do not display a CD signal in solution, their arrangement in a close packed film could induce a dichroism. The broadened and red shifted Soret band suggests a side by side interaction between porphyrins in the film. In porphyrin dimers, an exciton interaction can split the B bands and they display circular dichroism. Because of the different chirality of the scaffolds, the porphyrin-porphyrin interaction may have a different "sense" that arises from the geometry of packing, giving rise to a circular dichrosim. This kind of induced electronic "helicity" has been reported from porphyrin assemblies on DNA,[55-57] a helical cyanine dye J-aggregate induced by DNA-templates,[58] and other chiral induced systems.[59,60]

If environmentally induced dichroism of the porphyrin Soret band occurs in the SAM film, then the differential absorption of the circularly polarized exciting light could give rise to differential excited state populations. This dichroism could then give rise to the asymmetry in the photocurrent measurements. Circular dichroism spectra of the monolayer films of **R1** and **S1** were collected. No significant CD signal was observed; the maximum possible asymmetry was calculated to be less than 1 part in 10^4. Well below the asymmetry observed in the photocurrent experiment; 5 parts in 10^3.

An important caveat to consider is that a different propensity for photocurrent generation could exist for the aggregates of different helicity. In particular, the access of the viologen to the chromophore could be different in the two cases so that the asymmetry one observes in a photocurrent measurement is enhanced over that one may find in an absorption measurement. The fact that the **R** and **S** films had similar

asymmetries, while having somewhat different coverage, discounts this explanation somewhat.

2.6 Conclusions

Porphyrins on chiral scaffolds have been assembled on gold electrodes, and the effect of molecular chirality and light helicity on the photocurrent generation have been studied. The photocurrent displays an asymmetry when the chiral monolayer is irradiated by left and right circularly polarized light. The average asymmetry factor obtained for a right-handed monolayer is 0.004±0.002 and for a left-handed monolayer is -0.005±0.001, with confidence limits of 95%. Experimental and theoretical studies on the coupling of electron helicity and molecular chirality in the gas phase have shown asymmetry factors to be 10^{-3}-10^{-4} for oriented molecules and 10^{-4}-10^{-5} for unoriented molecules.[61-64] The asymmetry factors obtained in this work with the oriented chiral chain are one order of magnitude greater than those found from electron scattering[13,14] in gas phase but less than that of the photoemission through chiral Langmuir-Blodgett assemblies.[5]

The explanation proposed for the phenomenon is that the magnitude of the superexchange coupling through the chiral scaffold depends on the orbital polarization of the excited porphyrin; hence the tunneling probability depends on the light polarization. The relaxation of the orbital polarization should affect the importance of electron helicity on the coupling to the chiral bridge. If the orbital polarization relaxes rapidly, the nonequilibrium distribution will become depolarized and the influence of molecular chirality will be weak. In the limit of fast relaxation, the value of asymmetry factors would be small. To better understand the mechanism of the observation, further theoretical and experimental work is needed.

2.7 Acknowledgement

We acknowledge support from the U.S. National Science Foundation (CHE-0111435 and CHE-0348823 respectively).

2.8 References and Notes

(1) Jortner, J.; Bixon, M.; Eds. *Electron Transfer from Isolated Molecules to Biomolecules;* Advances in Chemical Physics, Vols. 106 and 107; Wiley: New york, 1999.

(2) Kuznetsov, A. M. *Charge Transfer in Physics, Chemistry and Biology;* Gordon & Breach: New York, 1995.

(3) Avalos, M.; Babiano, R.; Cintas, P.; Jimenez, J. L.; Palacios, J. C.; Barron, L. D. *Chem. Rev.* **1998**, *98*, 2391-2404.

(4) Ray, K.; Ananthavel, S. P.; Waldeck, D. H.; Naaman, R. *Science* **1999**, *283*, 814-816.

(5) Carmeli, I.; Skakalova, V.; Naaman, R.; Vager, Z. *Angew. Chem. Int. Ed.* **2002**, *41*, 761.

(6) Beerlage, M. J. M.; Farago, P. S.; Vanderwiel, M. J. *J. Phys. B: At. Mol. Opt. Phys.* **1981**, *14*, 3245.

(7) Blum, K.; Thompson, D. G. *Adv. At. Mol. Opt. Phys.* **1997**, *38*, 39.

(8) Bonner, W. A. *Chirality* **2000**, *12*, 114-126.

(9) Bonner, W. A.; Dort, M. A. V.; Yearian, M. R. *Nature* **1975**, *258*, 419-421.

(10) Hegstrom, R. A.; Rein, D. W.; Sandars, P. G. H. *J. Chem. Phys.* **1980**, *73*, 2329-2341.

(11) Johnston, C.; Blum, K.; Thompson, D. *J. Phys. B: At. Mol. Opt. Phys.* **1993**, *26*, 965.

(12) Mayer, S.; Kessler, J. *Phys. Rev. Lett.* **1995**, *74*, 4803.

(13) Mayer, S.; Nolting, C.; Kessler, J. *J. Phys. B* **1996**, *29*, 3497.

(14) Nolting, C.; Mayer, S.; Kessler, J. *J. Phys. B: At. Mol. Opt. Phys.* **1997**, *30*, 5491.

(15) Smith, I. M.; Thompson, D. G.; Blum, K. *J. Phys. B: At. Mol. Opt. Phys.* **1998**, *31*, 4029.

(16) Thompson, D. G.; Kinnin, M. *J. Phys. B: At. Mol. Opt. Phys.* **1995**, *28*, 2473.

(17) Ulbricht, T. L. V.; Vester, F. *Tetrahedron* **1962**, *18*, 629-637.

(18) Prins, M. W. J.; van Kempen, H.; de Groot, R. A.; van Roy, W.; De Beeck, J. *J. Phys. Condens. Matter* **1995**, *7*, 9447.

(19) Ouyang, M.; Awschalom, D. D. *Science* **2003**, *301*, 1074-1078.

(20) Morita, T.; Kimura, S.; Kobayashi, S.; Imanishi, Y. *J. Am. Chem. Soc.* **2000**, *122*, 2850-2859.

(21) Levins, C. G.; Schafmeister, C. E. T. *J. Am. Chem. Soc.* **2003**, *125*, 4703.

(22) Imahori, H.; Norieda, H.; Ozawa, S.; Ushida, K.; Yamada, H.; Azuma, T.; Tamaki, K.; Sakata, Y. *Langmuir* **1998**, *14*, 5335-5338.

(23) Wei, J.; Liu, H.; Dick, A. R.; Yamamoto, H.; He, Y.; Waldeck, D. H. *J. Am. Chem. Soc.* **2002**, *124*, 9591-9599.

(24) Hecht, E. *Optics, 2nd Ed.;* Addison-Wesley Publishing Co.: Reading, MA, 1987.

(25) Yariv, A.; Yeh, P. *Optical Waves in Crystals;* John Wiley and Sons: New York, 1984.

(26) Vitasovic, M.; Gouterman, M.; Linschitz, H. *J. Porphyrins Phthalocyanines* **2001**, *5*, 191.

(27) Wasbotten, I. H.; Conradie, J.; Ghosh, A. *J. Phys. Chem. B* **2003**, *107*, 3613-3623.

(28) Fasman, G. D.; Ed. *Circular Dichroism and the Conformational Analysis of Biomolecules;* Plenum: New York, 1996.

(29) Rodger, A.; Norden, B. *Circular Dichroism and Linear Dichroism;* Oxford University Press: Oxford, UK, 1997; Chapters 2 and 6.

(30) Yamada, H.; Imahori, H.; Nishimura, Y.; Ahn, T. K.; Kim, S. K.; Kim, D.; Fukuzumi, S. *J. Am. Chem. Soc.* **2002**, *124*, 9129.

(31) Hasobe, T.; Imahori, H.; Yamada, H.; Sato, T.; Ohkubo, K.; Fukuzumi, S. *Nano Lett.* **2003**, *3*, 409-412.

(32) Boeckl, M. S.; Bramblett, A. L.; Hauch, K. D.; Sasaki, T.; Ratner, B. D.; Rogers, J. W. *Langmuir* **2000**, *16*, 5644-5653.

(33) Akins, D. L.; Ozcelik, S.; Zhu, H. R.; Guo, C. *J. Phys. Chem.* **1996**, *100*, 14390-14396.

(34) Khairutdinov, R. F.; Serpone, N. *J. Phys. Chem. B* **1999**, *103*, 761-769.

(35) Maiti, N. C.; Mazumdar, S.; Periasamy, N. *J. Phys. Chem. B* **1998**, *102*, 1528-1538.

(36) Osuka, A.; Maruyama, K. *J. Am. Chem. Soc.* **1988**, *110*, 4454-4456.

(37) Imahori, H.; Norieda, H.; Nishimura, Y.; Yamazaki, I.; Higuchi, K.; Kato, N.; Motohiro, T.; Yamada, H.; Tamaki, K.; Arimura, M.; Sakata, Y. *J. Phys. Chem. B* **2000**, *104*, 1253-1260.

(38) Taylor, J. R. *An Introduction to Error Analysis, 2nd ed.;* University Science Books: Sausalito, CA, 1997.

(39) Khoshtariya, D. E.; Wei, J.; Liu, H.; Yue, H.; Waldeck, D. H. *J. Am. Chem. Soc.* **2003**, *125*, 7704-7714.

(40) Napper, A. M.; Liu, H.; Waldeck, D. H. *J. Phys. Chem. B* **2001**, *105*, 7699-7707.

(41) Wei, J. J.; Liu, H. Y.; Khoshtariya, D. E.; Yamamoto, H.; Dick, A.; Waldeck, D. H. *Angew. Chem. Int. Ed.* **2002**, *41*, 4700-4703.

(42) Chirvony, V. S.; van Hoek, A.; Galievsky, V. A.; Sazanovich, I. V.; Schaafsma, T. J.; Holten, D. *J. Phys. Chem. B* **2000**, *104*, 9909-9917.

(43) Gentemann, S.; Medforth, C. J.; Forsyth, T. P.; Nurco, D. J.; Smith, K. M.; Fajer, J.; Holten, D. *J. Am. Chem. Soc.* **1994**, *116*, 7363-7368.

(44) Dick, H. A.; Bolton, J. R.; Picard, G.; Munger, G.; Leblanc, R. M. *Langmuir* **1988**, *4*, 133-136.

(45) Imahori, H.; Norieda, H.; Yamada, H.; Nishimura, Y.; Yamazaki, I.; Sakata, Y.; Fukuzumi, S. *J. Am. Chem. Soc.* **2001**, *123*, 100-110.

(46) Meier, F.; Zakharchenya, B. P. *Optical Orientation: Modern Problems in Condensed Matter Sciences;* North-Holland: Amsterdam, The Netherlands, 1984; Vol. 8.

(47) Fiederling, R.; Keim, M.; Reuscher, G.; Ossau, W.; Schmidt, G.; Waag, A.; Molenkamp, L. W. *Nature* **1999**, *402*, 787-790.

(48) Green, A. S.; Gallup, G. A.; Rosenberry, M. A.; Gay, T. J. *Phys. Rev. Lett.* **2004**, *92*, 093201.

(49) Starke, K.; Kaduwela, A. P.; Liu, Y.; Johnson, P. D.; Van Hove, M. A.; Fadley, C. S.; Chakarian, V.; Chaban, E. E.; Meigs, G.; Chen, C. T. *Phys. Rev. B* **1996**, *53*, R10544.

(50) Heinzmann, U.; Schönhense, G.; Kessler, J. *Phys. Rev. Lett.* **1979**, *42*, 1603.

(51) Schönhense, G.; Eyers, A.; Friess, U.; Schäfers, F.; Heinzmann, U. *Phys. Rev. Lett.* **1985**, *54*, 547.

(52) Borovkov, V. V.; Hembury, G. A.; Inoue, Y. *Acc. Chem. Res.* **2004**, *37*, 449-459.

(53) Ivchenko, E. L.; Pikus, G. E. *Superlattices and Other Heterostrructures Symmetry and Optical Phenomena;* Springer: Berlin, Germany, 1997.

(54) Prinz, G. A. *Phys. Today* **1995**, *48*, 58.

(55) Gibbs, E. J.; Maurer, M. C.; Zhang, J. H.; Reiff, W. M.; Hill, D. T.; Malicka-Blaszkiewicz, M.; McKinnie, R. E.; Liu, H. Q.; Pasternack, R. F. *Journal of Inorg. Biochem.* **1988**, *32*, 39-65.

(56) Gibbs, E. J.; Tinoco, J. I.; Maestre, M. F.; Ellinas, P. A.; Pasternack, R. F. *Biochem. Biophys. Res. Commun.* **1988**, *157*, 350-358.

(57) Pasternack, R. F.; Brigandi, R. A.; Abrams, M. J.; Williams, A. P.; Gibbs, E. J. *Inorg. Chem.* **1990**, *29*, 4483-4486.

(58) Wang, M.; Silva, G. L.; Armitage, B. A. *J. Am. Chem. Soc.* **2000**, *122*, 9977-9986.

(59) Hirschberg, J. H. K. K.; Brunsveld, L.; Ramzi, A.; Vekemans, J. A. J. M.; Sijbesma, R. P.; Meijer, E. W. *Nature* **2000**, *407*, 167-170.

(60) Matsui, H.; Kushi, S.; Matsumoto, S.; Akazome, M.; Oguro, K. *Bull. Chem. Soc. Jpn.* **2000**, *73*, 991.

(61) Campbell, D. M.; Farago, P. S. *J. Phys. B* **1987**, *21*, 5133.

(62) Musigmann, K.; Blum, K.; Thompson, D. G. *J. Phys. B: At. Mol. Opt. Phys.* **2001**, *34*, 2679.

(63) Musigmann, M.; Bussalla, A.; Blum, K.; Thompson, D. G. *J. Phys. B: At. Mol. Opt. Phys.* **1999**, 4117.

(64) Rich, A.; Van House, J.; Hegstrom, R. A. *Phys. Rev. Lett.* **1982**, *48*, 1341.

2.9 Supporting Information

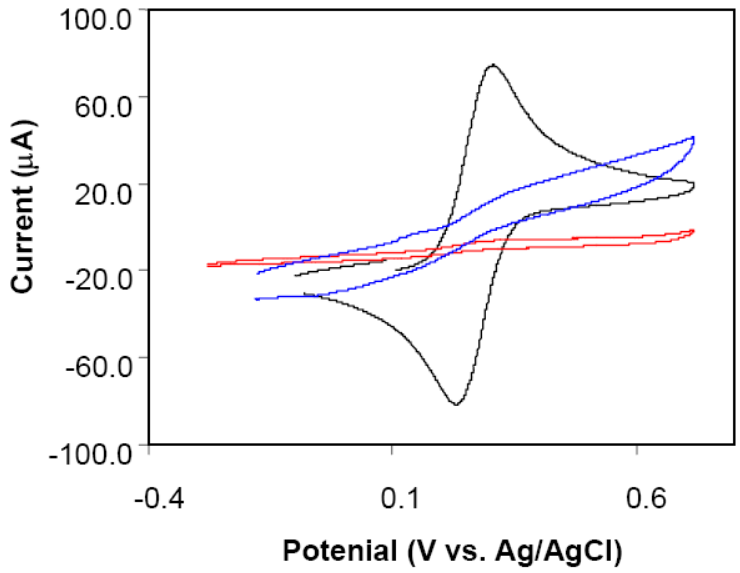

Figure 2.10 Voltammograms are shown for three different electrodes in contact with an equimolar (1 mM) $Fe(CN)_6^{3-/4-}$ solution (black is bare gold electrode; blue is 4-mer-SS-porphyrin-film electrode; red is 4-mer-RR-porphyrin-film electrode).

Microscopy

Scanning Tunneling Microscopy (STM) was used to directly image the structures of the scaffold porphyrins at the gold surface. Figure 2.11 panel A, shows a topographic image for an electrode that has a pure film of the scaffold porphyrin adsorbed on the surface. Panel B shows the features of a cross-section through a domain in the image. The bright spot (domain) analyzed here is typical and has a width of 3-4 nm and a height of 2.2 nm. The vertical/ height length scale is shown here for the images are compressed over the actual physical height. These dimensions imply an aggregate of about two scaffold porphyrin molecules. A statistical analysis of the image in Figure 2.11 gives domain coverage of 70% (very rough), similar to the coverage estimated from cyclic voltammetry. It is evident from the image that the scaffold porphyrin forms aggregates

(nano-domains) but its dependence on preparation and solvent conditions has not yet been investigated.

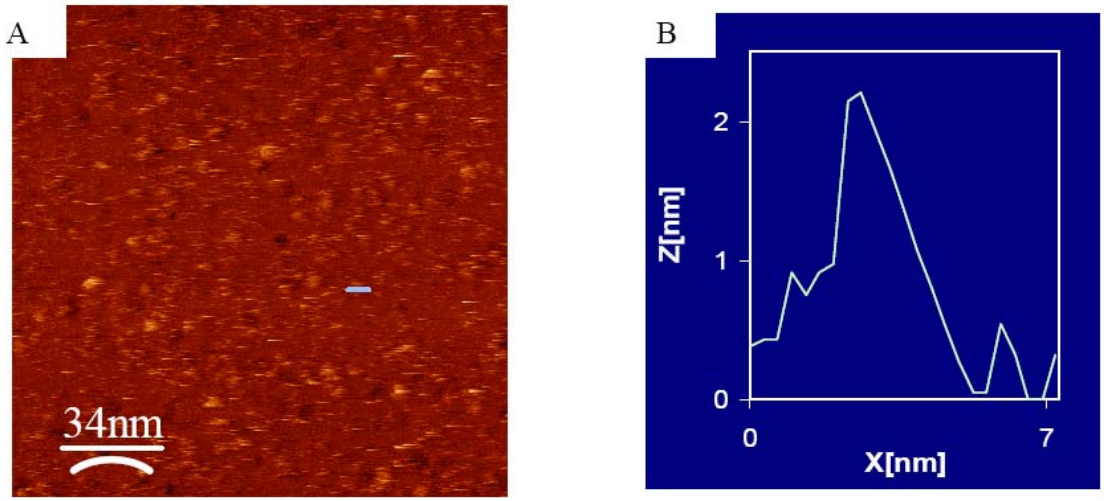

Figure 2.11 STM images for pure scaffold (4-mer SS) porphyrin SAMs at gold surface. Panel A shows an actual topographic image for an electrode that has scaffold porphyrin adsorbed on the surface; Panel B shows the feature of a cross section

Chapter 3 Charge Transfer through Single Stranded Peptide Nucleic Acid Composed of Thymine Nucleotides

This work has been published as Amit Paul, Richard M. Watson, Paul Lund, Yangjun Xing, Kathleen Burke, Yufan He, Eric Borguet, Catalina Achim, David H. Waldeck, *J. Phys. Chem. C*. **2008**, *112*, 7233-7240

3.1 Abstract

Self-assembled monolayers (SAMs) of single stranded peptide nucleic acids (PNAs) containing three to seven thymine (T) nucleotides, a C-terminal cysteine, and an N-terminal ferrocene group were formed on gold electrodes. The existence of two redox environments for the ferrocene was detected by cyclic voltammetry and was attributed to the presence of 'lying-down' and 'standing-up' PNA molecules. By exploiting the chemical instability of the ferrocenium ion, electrochemical cycling was used to destroy the ferrocene of 'lying-down' molecules while keeping the ferrocene in the 'standing-up' molecules intact. Electrochemical measurements were used to determine the electron transfer rate through the 'standing-up' PNA molecules. The tunneling decay constant for these SAMs was determined to be about 0.9 $Å^{-1}$.

3.2 Introduction

The interest in self-assembled monolayers (SAMs)[1,2] of nucleic acids has increased recently, largely because of their potential applications in molecular electronics,[3] materials science,[4] molecular recognition,[5] biotechnology and biosensor development.[6-8] An understanding of the charge transport (CT) through such SAMs is needed to realize their potential in molecular electronics and biosensing. The past decade has seen progress in understanding charge transfer through deoxyribonucleic acid (DNA), which is believed

to occur through either a superexchange mechanism,[9-19] which dominates at short distances, or a hopping mechanism,[20-25] which dominates at large distances.

The weak distance dependence of the charge hopping mechanism and its prevalence in duplex DNA systems has motivated the exploration of charge transfer through DNA and its promise for molecular electronics by a large number of different research groups. Nevertheless, only a few research groups have studied CT of DNA monolayers, probably because of the difficulties in creating well-defined DNA assemblies on a metal surface.[26-28] For example, Hartwich et al.[29] used cyclic voltammetry to characterize charge transfer in mixed monolayers of DNA having a pyrrolo-quinoline-quinone redox probe attached to DNA through a spacer, and linked to an Au(111) surface through an ethane-thiol linker. These studies determined that the CT rate constant for a 12-base pairs (bp) DNA duplex was 1.5 s^{-1} while for the same duplex containing two mismatches it was 0.6 s^{-1}, and that charge transfer could not be detected for single-stranded (ss) DNA at a scan rate of >10 mV s^{-1}. Liu et al.[30] argued that CT through a monolayer of a 30-bp double stranded (ds) DNA takes place through the base stack and does not involve the DNA backbone. They based their argument on the fact that the rate constant for CT of 30 s^{-1} was not affected by breaks in the sugar-phosphate backbone and was too small to be measured when a mismatch was introduced in the ds DNA. Interestingly, a similar rate constant for CT was measured for a monolayer of a 15-bp ds DNA.[31] CT rate constants for ss oligonucleotides are also quite high. For example, Kraatz and collaborators reported a CT rate constant of 12 s^{-1} for a 20-base ss DNA monolayer, which was only 10 times lower than the rate constant for a monolayer of the corresponding 20-bp ds DNA.[32,33] The studies on duplex DNA indicate an important role for the base pairs, while

those on ss-DNA suggest that the bases may contribute significantly even when they are not involved in base pairing.

Peptide nucleic acid (PNA) is an analogue of DNA that has a neutral and achiral backbone based on aminoethylglycine, in contrast to the negatively-charged and chiral backbone of DNA (Figure 3.1 a).[34,35] Like DNA, PNA forms duplexes with itself and other nucleic acids by Watson-Crick base pairing. The PNA·PNA duplexes adopt a helical structure termed P-type, which has a large pitch with 18 bases/turn, diameter of 28 Å, and 3.2-3.4 Å rise/base pair.[36-38] Recent work shows that ligand-modified PNA can be used as a scaffold for transition metal ions.[39-41] The inorganic nucleic acid structures formed by this method contain transition metal ions at specific positions and may mediate CT over tens of nanometers, in a manner similar to that in which metal cofactors mediate electron transfer in metalloproteins. The study of charge transfer in such metalized PNA is a long term goal toward which the experiments described below are targeted.

ssPNA has a clear advantage over ssDNA for SAM preparation, because it is neutral.[42-44] Martin-Gago and coworkers[42-44] successfully prepared SAMs of ss PNA molecules having a cysteine group at the C-terminus that bound the PNA to the gold surface. They characterized the surface by X-ray photoemission spectroscopy (XPS), atomic force microscopy (AFM), X-ray absorption near-edge spectroscopy (XANES), and reflection-absorption infrared spectroscopy (RAIRS). They proposed that the formation of PNA SAMs occurs in two main steps; at low coverage, the adsorbed ss PNA molecules lie down on the surface; as the surface coverage increases, the layer of lying down molecules undergoes a phase transition and the PNA realigns perpendicular to the

surface. This two-phase mechanism is similar to that proposed for the formation of alkanethiol SAMs.[1,2]

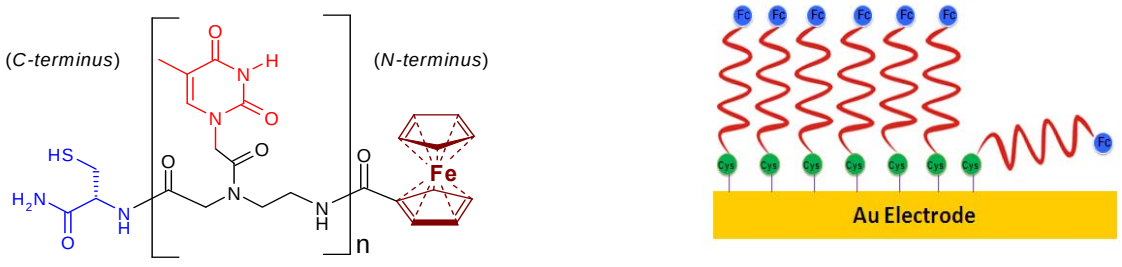

(a) (b)

Figure 3.1 (a) Chemical structure of thymine containing ss PNA that has a C-terminus cysteine and an N-terminus ferrocene, where n = 3 to 7. (b) Panel B shows a schematic representation of PNA molecules self-assembled on a gold surface, in which the green circle represents cysteine, the red curl represents PNA and the blue circle represents ferrocene.

In this work, PNA SAMs were grown on gold ball electrodes and used to systematically study the distance dependence of the electron transfer to a ferrocene redox reporter. The changeover of mechanism from tunneling to hopping in DNA has been shown to depend on the bases present in the nucleic acid and is linked to their oxidation potential.[20] Among the four different natural nucleobases, thymine (T) and cytosine (C) has the highest oxidation potential.[45] Therefore the change over from a superexchange mechanism to charge hopping in T-only nucleic acids should occur at larger distances than for nucleic acids composed of other nucleobases. With an aim to evaluate electron tunneling in PNA-based SAMs, the electron transfer through short PNA oligomers containing thymine only were studied (see Figure 3.1(a)). PNA was immobilized on a gold surface through a cysteine group at the C-terminus of the PNA (Figure 3.1(b)), which forms a gold-sulfur bond. A ferrocene redox probe was covalently attached at the

N-terminus of the PNA. The presence of two distinct subpopulations of the ferrocene, namely a fast CT rate, or 'lying-down', population and a slow CT rate, or 'standing-up', population was detected by atomic force microscopy (AFM) and cyclic voltammetry (CV). This finding was supported by ellipsometry[46,47] and contact angle studies. By electrochemically destroying the fast population, it was possible to measure the electron transfer rate constants for the slow population. The length of the PNA was varied by increasing the number of thymine nucleotides, and the tunneling decay constant (β) for single stranded PNA molecules was determined. The rapid decay of the charge transfer rate with increasing number of thymines was found to be consistent with a superexchange-mediated tunneling mechanism.

3.3 Experimental

PNA synthesis: PNA oligomers were synthesized by solid phase peptide synthesis using the Boc protection strategy.[48-50] MBHA resin (Peptides International, Louisville, KY) with a loading of 0.18 mEquiv/g was down-loaded (see reference 50 for more detail about this procedure) using Boc-L-Cys-(4-MeOBzl)-OH (NovaBiochem/Merck Biosciences, Switzerland) to an estimated loading of 0.04-0.06 mEquiv/g. Thereafter, 3-7 Boc-T-OH PNA monomers (Applied Biosystems, Foster City, CA) were coupled using *O*-(1H-6-chlorobenzotriazole-1-yl)-*N,N,N',N'*-tetramethyluronium hexafluorophosphate (HCTU, Peptide International) or *O*-benzotriazoly-1-yl-*N,N,N',N'*-tetramethyluronium hexafluorophosphate (HBTU, Peptide International) as a coupling agent. Finally, ferrocenecarboxylic acid (Aldrich) was coupled to the N-terminus using the same coupling procedure, repeated twice to increase the yield of ferrocene-conjugated PNA. Oligomers were cleaved from the resin using trifluoroacetic acid (TFA) and

trifluoromethanesulfonic acid (TFMSA), thioanisole, and m-cresol, precipitated in ethyl ether, and dried under nitrogen. The solid products were dissolved in 15% acetonitrile aqueous solution and purified by reverse-phase HPLC using a solvent gradient, from 15% to 35% acetonitrile in water over 40 minutes on a Waters Delta 600 pump with a 2996 photodiode array detector (Milford, MA). PNA oligomers were characterized by MALDI-TOF mass spectrometry on an Applied Biosystems Voyager-DE STR Workstation. (MALDI-TOF mass spectra is available in supporting information)

PNA solutions were prepared in deionized water and the PNA concentrations were determined by UV-Vis spectrophotometry assuming ε_{260} = 8600 cm^{-1} M^{-1} for each T-monomer.[50] PNA solutions for electrode incubation were typically 20 μM ssPNA in 10 mM pH 7.0 sodium phosphate buffer solution that was a 50% acetonitrile/50% water mixture.

Electrode Preparation: A gold wire (0.5 mm diameter, 99.999%, Alfa Aesar, MA) was cleaned by reflux in nitric acid (70%) at 130°C for two hours and then washed with deionized water (>18 MΩ. cm). The wire was sealed in a soft-glass capillary tube with the tip exposed. The tip of the gold wire was heated to form a ball. The gold ball was reheated in a flame until glowing, then slowly cooled down and finally quenched in deionized water. This annealing process was repeated more than fifteen times until a smooth ball electrode was obtained. The area of the electrode was determined electrochemically[51] and found to be typically ~0.1 cm^2.

Self Assembled Monolayer (SAM) Preparation: Self-assembled monolayers were prepared by incubating gold ball electrodes in 1 mL of a 20 μM PNA solution under the

conditions specified in Table 3.1. After incubation the gold electrodes were washed with nanopure water and directly used in the electrochemical studies.

Table 3.1 Incubation Temperature and Incubation Time used for PNA SAM preparation

Molecule	Temperature (°C)	Incubation time (Hour)
Cys-T3-Fc	40°	40
Cys-T4-Fc	35°/40°	40
Cys-T5-Fc	40°	40
Cys-T6-Fc	40°	40
Cys-T7-Fc	40°	28

Evidence of ferrocene decomposition by cyclopentadiene loss was observed for the PNA oligomers if the incubation solutions were kept in light for several days. However MALDI-ToF characterization of the PNA SAMs (SAMDI-ToF)[52] showed no evidence of ferrocene decomposition after incubation at 30-40°C for 42-48 hours (supporting information). After SAM preparation under the conditions described here, the electrodes could be kept in nanopure water, and electrochemical experiments could be performed more than ten days after incubation without significant changes in the response.

Electrochemical Measurements: Cyclic voltammetry was carried out on a CH Instrument Electrochemical Analyzer 618B (Austin, TX). The three-electrode electrochemical cell consisted of an Ag/AgCl (3 M KCl) reference electrode, a platinum wire as counter electrode, and a SAM-coated gold ball electrode as the working electrode. All

experiments were performed in 1 M $NaClO_4$ (pH=7-8) aqueous electrolyte solution at room temperature. The uncompensated solution resistance was measured by AC impedance and found to be less than 5 Ω, so that the iR drop was not important for these measurements. The coverage of the PNA-ferrocene SAM was calculated by integrating the charge under the voltammetric peaks.

Atomic Force Microscopy (AFM): Atomic force microscopy was carried out on a Molecular Imaging PicoPlus (Tempe, AZ) instrument. A tapping mode silicon cantilever AFM tip (NSC16, Resonant frequency 170 kHz, force constant 40 N/ m, MikroMasch, Estonia) was used. AFM experiments were done in ambient at room temperature.

The Au bead electrode was made by melting a 0.8 mm Au wire (99.999%, Alfa Aesar, MA) in a hydrogen flame. Prior to the experiments the substrate was cleaned by immersion in hot piranha solution (1:3 H_2O_2 and 98% H_2SO_4) in ambient conditions at room temperature **(Caution! The piranha solution is a very strong oxidizing agent and extremely dangerous. Eye protection and gloves should be used during handling)** for one hour. After each step the sample was rinsed by sonication in deionized water. After cleaning, the crystal was annealed in a hydrogen flame and allowed to cool in air. The ~2.6 mm diameter bead displayed numerous facets of ~0.5 mm diameter, with predominant (111) orientation.

Ellipsometry and Contact Angle: The molecules were self-assembled to form a monolayer thick film on evaporated gold slides (EMF Corp, Ithaca, NY). The Au slides were 0.7 inch x 0.3 inch x 0.062 inches in size and consisted of about 100 nm Au over a 50 nm thick Ti binder layer on float glass. The gold slides were cleaned by immersion in "piranha" solution (1:3 H_2O_2 and 98% H_2SO_4) **(Caution! The piranha solution is a very**

strong oxidizing agent and extremely dangerous. Eye protection and gloves should be used during handling) for two minutes, then rinsed by a large amount of deionized water, followed by ethanol. They were, subsequently dried under nitrogen. For SAM formation, the Au slides were incubated in 1.0 mL of a 20 μM PNA solution under the conditions specified in Table 3.1. After incubation, these SAM-coated gold slides were rinsed vigorously with ethanol and water and dried under nitrogen. The thickness was measured by a Gaertner L-117 Null ellipsometer, and the contact angle with water was measured on the same gold slides using a home-built goniometer system.

3.4 Background

The Electron Transfer Rate Constant[53-62]*:* In the nonadiabatic limit, the electron transfer rate constant k_{et} is given by the Fermi Golden Rule expression,

$$k_{et} = \frac{2\pi}{\hbar}|V|^2 FCWDS \tag{3.1}$$

Equation 3.1 describes the rate constant for a nonadiabatic transition between two states, which have an electronic coupling magnitude of $|V|$. FCWDS is the Franck-Condon weighted density of states, which accounts for the effect of nuclear coordinates on the rate constant. If the Gibbs reaction free energy (ΔG) is smaller than the reorganization energy λ of the reaction (normal regime) and if high frequency vibrational modes of the donor and acceptor do not contribute significantly to the reorganization energy, the FCWDS can be written as

$$FCWDS = \frac{1}{\sqrt{4\pi\lambda k_B T}} \exp\left[-\frac{(\lambda + \Delta G)^2}{4\lambda k_B T}\right] \tag{3.2}$$

The reorganization energy λ encompasses an inner sphere contribution λ_{in}, which is associated with the internal coordinates of the redox species, and an outer sphere component λ_{out}, which is dominated by the solvent polarization. For the ferrocene/ ferrocenium redox couple the λ_{out} term is dominant and the reorganization energy in water is reported to lie between 0.7 eV and 0.96 eV.[62,63]

For electron transfer at an electrode, equations 3.1 and 3.2 must be generalized to consider the distribution of electronic states that are available in the solid. For an electron at energy ε in the electrode, the free energy of reaction is given by

$$\Delta G = (\varepsilon_F - \varepsilon) + e\eta \tag{3.3}$$

where η is the overpotential and ε_F is the Fermi level of the electrode. Substitution of equation 3.3 into equation 3.2 generates

$$k_{red}(\varepsilon,\eta) = \frac{2\pi}{\hbar}|V|^2 \frac{1}{\sqrt{4\pi\lambda k_B T}} \exp\left[-\frac{(\lambda + (\varepsilon_F - \varepsilon) + e\eta)^2}{4\lambda k_B T}\right] \tag{3.4}$$

The total rate constant for reduction requires integration over all electronic states of the solid, so that

$$k_{red}(\varepsilon,\eta) = \frac{2\pi}{\hbar}|V|^2 \frac{1}{\sqrt{4\pi\lambda k_B T}} \int_{-\infty}^{\infty} \rho(\varepsilon) \times \exp\left[-\frac{(\lambda + (\varepsilon_F - \varepsilon) + e\eta)^2}{4\lambda k_B T}\right] f(\varepsilon) d\varepsilon \tag{3.5}$$

where $\rho(\varepsilon)$ is the density of electronic states of the electrode (often an energy-independent average value is used), and $|V|$ is assumed to be independent of energy. $f(\varepsilon)$ is the Fermi-Dirac distribution law

$$f(\varepsilon) = \frac{1}{1 + \exp[(\varepsilon - \varepsilon_F)/k_B T]} \tag{3.6}$$

An expression similar to equation 3.5 can be written for the oxidation rate constant

$$k_{ox}(\varepsilon,\eta) = \frac{2\pi}{\hbar}|V|^2 \frac{1}{\sqrt{4\pi\lambda k_B T}} \int_{-\infty}^{\infty} \rho(\varepsilon) \times \exp\left[-\frac{(\lambda + (\varepsilon_F - \varepsilon) - e\eta)^2}{4\lambda k_B T}\right][1 - f(\varepsilon)]d\varepsilon \qquad (3.7)$$

The electron-transfer rate constants have been obtained by measuring the shift in the faradaic current peak potential as a function of voltage scan rate in cyclic voltammetry experiments and fitting of the data by the Marcus model. Equations 3.5 and 3.7 were used to create working curves of peak shift versus $\log_{10}$(scan rate/k^0) for specific values of λ at room temperature.[58] Those working curves were used to fit the experimental data and obtain the standard electrochemical rate constant k^0. See reference 58 for more detail about this procedure.

3.5 Results

Characterization of PNA monolayers

Contact Angle Measurements: The static contact angles measured for the PNA SAMs with water are between 35° and 53° (Table 3.2), and they decrease with the increasing length of the PNA, which means that the hydrophilicity of the exposed surface increases with the PNA length. Because the thymines are hydrophilic and ferrocene is hydrophobic, the increase in hydrophilicity with the PNA length suggests that the thymines of the PNA oligomers are solvent accessible and the monolayer is not compact.

Ellipsometry Studies: Ellipsometry determines the film thickness by measuring the change in light polarization upon reflection from the surface. The thickness determination requires knowledge of the refractive index of the SAM. The refractive index of a PNA SAM has not been reported yet. Therefore in this study, we have used a refractive index of 1.6, which is between the refractive indices of 1.57 and 1.7 reported for protein and DNA SAMs, respectively.[64-66] Any difference between the actual refractive index of a

PNA SAM and 1.6 will cause a systematic error in the calculated thickness value, but it will not affect the trend observed for the change in thickness with the length of the PNA. The PNA SAM thicknesses, which have been obtained in this way, are compared with the lengths of different PNA molecules in Table 3.2. These molecular lengths have been determined by adding characteristic lengths for the cysteine (4 Å), the ferrocene (5 Å), and each PNA base (3.5 Å).[67]

If the SAM was highly compact and the PNA strands were fully extended then the calculated lengths and the ellipsometrically determined film thicknesses in Table 3.2 would agree, for each PNA oligomer. In contrast, the ellipsometrically determined film thickness was less than the calculated length of the fully extended molecules and there is no systematic change of the SAM film thickness with chain length. In order to understand the ellipsometric results better the PNA SAMs were modeled in two different ways.

Table 3.2 Ellipsometric Thickness, Calculated Length and Contact Angle of PNA Molecules

Molecule	Ellipsometric Thickness (nm)	Calculated Length of PNA (nm)	Contact Angle with H_2O
Cys-T3-Fc	1.4 ± 0.1	1.95	53° ± 2°
Cys-T4-Fc	1.4 ± 0.1	2.30	47° ± 1°
Cys-T5-Fc	1.3 ± 0.1	2.65	41° ± 1°
Cys-T6-Fc	2.1 ± 0.1	3.00	40° ± 1°
Cys-T7-Fc	2.3 ± 0.1	3.35	35°± 1°

In the first model, the PNA SAMs were assumed to be compact and all the PNA oligomers were assumed to be tilted on the surface at some angle from the surface normal. Based on this model, we determined by simple geometry an average tilt angle

from the measured film thickness of 43±4°, 51±3°, 62±3°, 46±3° and 47±3° from Cys-T3-Fc to Cy-T7-Fc respectively. These angles are relatively large when compared to the tilt angle of alkanethiol[68,69] and there is no trend of the angles with the PNA length.

In the second model, the PNA SAMs were assumed to consist of two different phases that differed in thickness, namely a 'lying-down' phase. The 'standing-up' molecules were assumed to be oriented perpendicular to the surface, *i.e.,* the PNA's backbone axis is oriented along the surface normal, and the 'lying-down' molecules were assumed to be parallel to the Au surface, *i.e.,* the backbone axis is perpendicular to the surface normal. The thickness of the 'lying-down' molecules was taken as 0.5 nm and the thickness of the 'standing-up' molecules was taken to be the calculated length given in Table 3.2. The average thickness was computed as a weighted sum of the thickness for the 'lying-down' molecules and the 'standing-up' molecules. Equating the ellipsometric thickness to the average thickness allowed the percentage of each phase to be determined. The percentage of the 'lying-down' phase was found to be 36±5% for Cys-T3-Fc, 48±4% for Cys-T4-Fc, 64±6% for Cys-T5-Fc, 38±4% for Cys-T6-Fc, and 38±5% for Cys-T7-Fc. These percentages correspond to the geometric area of the surface that is covered by the 'lying down' phase; and not the percentages of the PNA oligomers in each phase. If the 'standing up' molecules can be approximated as cylinders with a radius r of 0.49 nm[70] and height equal to the calculated length of the PNA, then the circular footprint of the molecules in the 'standing up' phase is πr^2 = 0.75 nm^2 and the rectangular footprint of molecules in the 'lying down' phase is $2 \cdot r \cdot h$ = $0.98 \cdot h$ nm^2. Using the ellipsometric fractions and this model, the percentage of the 'lying-down' molecules are 14.1±2.0% for

Cys-T3-Fc, 16.0±1.4% for Cys-T4-Fc, 18.5±1.7% for Cys-T5-Fc, 9.7±1.0% for Cys-T6-Fc, and 8.7±1.2% for Cys-T7-Fc.

AFM Studies: Tapping mode Atomic Force Microscopy was performed on a Cys-T6-Fc SAM formed on a (111) facet of a large gold bead. Note that the Au beads used for the AFM studies had an area which is about five times larger than the area of the Au ball

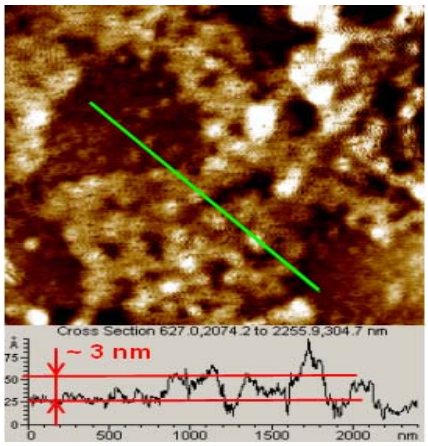

Figure 3.2: A tapping mode AFM topography image (3 μm x 3 μm) is shown for Cys-T6-Fc monolayer, collected in ambient at room temperature.

electrodes used for electrochemistry. The AFM topography image in Figure 3.2 shows two distinct regions, with a significant height difference of about 3 nm. The calculated length of a fully extended Cys-T6-Fc is about 3 nm. This result supports the idea that a 'standing-up' phase and a 'lying-down' phase coexist on the Au surface. Analysis of multiple AFM images revealed that 52±10% of the total area was occupied by a 'lying-down' phase, which is somewhat larger than the 38±4% value obtained from the ellipsometry measurements.

Electrochemical Characterization: This section describes the electrochemical manifestations of the PNA SAMs grown by incubating gold electrodes first at room temperature and then at higher temperature (35°C to 40°C).

Initial attempts to grow ss-PNA SAMs by incubation of the electrodes with a 20 µM solution of PNA in pH=7, 10 mM phosphate buffer at room temperature for up to 48 h generated SAMs with low surface coverage of 50±3 to 56±5 pmol/cm^2, compared to the maximum expected surface coverage of 300 pmol/cm^2 for Cys-Tn-Fc,[70] where n=4-6. The electron transfer rate constants for these films were k^0 = 1833 ± 61 s^{-1}, 1081 ± 493 s^{-1}, and 633 ± 28 s^{-1} for Cys-T4-Fc, Cys-T5-Fc, and Cys-T6-Fc respectively. Given the poor surface coverage, it is possible that the PNA molecules were 'lying-down' on the surface. The weak length dependence may reflect a change in the average distance between the gold electrode and the ferrocene due to packing in the film. A similar high transfer rate was reported by Anne et al.[71] for thymine (T) containing single stranded DNA molecules lying flat on gold surfaces.

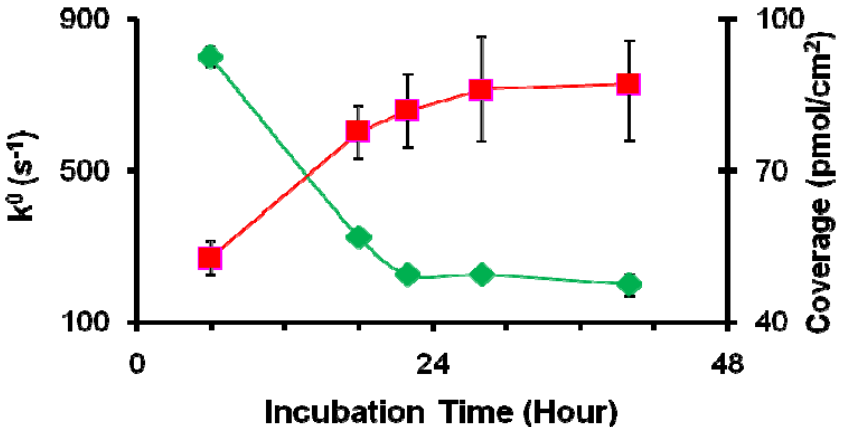

Figure 3.3 The electron transfer rate (diamond symbols) and coverage (square symbols) for Cys-T4-Fc SAMs are plotted as a function of the incubation time at 35°C.

Higher coverage and more compact films have been formed by incubating electrodes in PNA solutions at 35°C. The surface coverage was measured by integrating the charge passed in voltammograms, which increased with the incubation time; the growth of the Cys-T4-Fc SAM was complete in 22 to 28 hours (Figure 3.3). Simultaneously, the measured electron transfer rate constant, k^0, decreased with the increasing incubation time for a Cys-T4-Fc film, which suggests an increase in the fraction of PNA molecules that 'stand-up'. In this case the charge transfer would take place by tunneling through the PNA rather than directly through space from ferrocene to the Au surface, which would dominate for PNA molecules that are 'lying down'. No significant change in coverage of Cys-T4-Fc SAMs was found by elevating the incubation temperature from 35°C to 40°C.

Although the optimized conditions lead to more compact films, it was not possible to make films in which all of the PNA molecules are 'standing-up' on the surface. For the oligomers Cys-T5-Fc, Cys-T6-Fc and Cys-T7-Fc the presence of two different phases, namely 'lying down' and 'standing up' molecules, was observed by voltammetry. If the potential scan speed is slow enough in a voltammetry experiment, electrochemical reversibility can be achieved. For a reversible process, the FWHM of the peaks is ~90.6 mV and the voltammetric peak maxima appear at the formal potential (E^0) of the redox probe. As the potential scan speed is increased and becomes fast compared to the electron transfer rate, the voltammetric peak maxima shift away from the formal potential. If the electron transfer rates of the 'lying-down' and 'standing-up' phases are different enough, their peaks shift by a different amount for a given scan speed and can be distinguished.

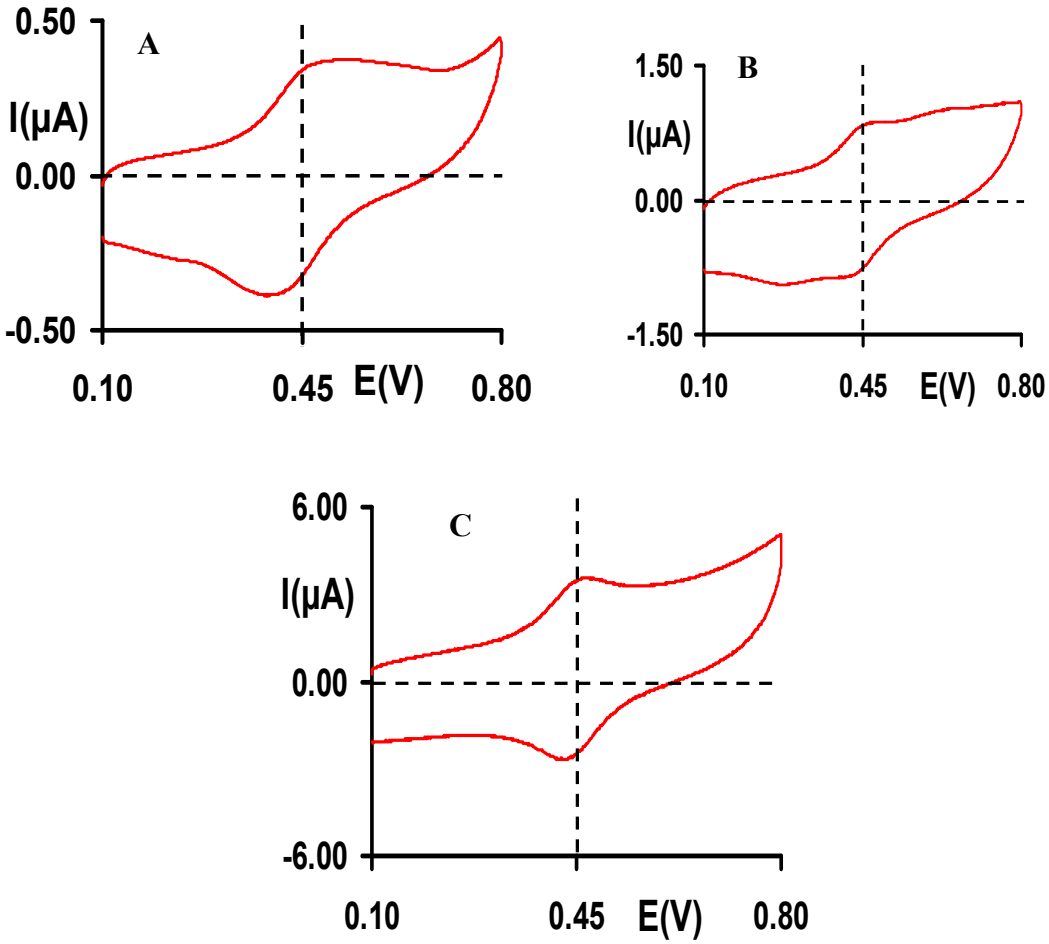

Figure 3.4 Three cyclic voltammograms are shown for Cys-T6-Fc SAM at scan rate (A) 20 mV/s, (B) 80 mV/s and (C) 1 V/s. The vertical dashed line marks the formal potential of ferrocene.

Figure 3.4 shows three representative voltammograms for Cys-T6-Fc. The voltammogram taken at a 20 mV/s scan speed shows a broad peak (200 mV FWHM) and a peak maximum that is shifted from the formal potential of ferrocene (Panel A). The voltammogram at 80 mV/s scan speed shows two peaks one which appears to be nearly reversible and one in which the peak maxima are strongly displaced from each other (Panel B). The voltammogram taken at 1 V/s scan speed shows a sharp peak with a 102 mV FWHM and peak maxima close to the formal potential of the ferrocene (Panel C).

These data can be understood in terms of two distinct populations of Cys-T6-Fc coexisting on the gold surface. One population has a fast electron transfer rate, presumably a 'lying-down' species in which the ferrocene is near the gold electrode. The second population has a slow electron transfer rate, presumably a 'standing-up' species in which electron transfer occurs through the PNA. At slow scan speeds, both populations undergo electron transfer. As the scan speed is increased, the peaks for the slow population shift and decrease in amplitude until they are no longer evident in the potential window. If the scan speed is high enough, the 'standing up' species do not undergo electron transfer. Panel C corresponds to this latter case, in which the scan speed is slow compared to the electron transfer rate for the 'lying down' species but is fast compared to the electron transfer rate of the 'standing up' species. Consequently, the voltammogram looks nearly ideal and corresponds to reduction and oxidation of the 'lying down' species only.

This interpretation of the electrochemical behavior was corroborated by the analysis of the total charge passed through the film. At the 20 mV/s scan speed (panel A) the total charge is 1.5 μC, whereas at 1 V/s the total charge is only 0.14 μC. Hence at 20 mV/s, the slow species dominates the response and the peak maxima are shifted. Less charge is passed at the higher scan speed because only the 'lying down' species undergo electron transfer. For this particular Cys-T6-Fc film, the percentage of 'lying-down' molecules was found to be 9.3% from the charge passed, corresponding to 14.5 pmol/cm^2. This percentage of 'lying down' and 'standing up' species is similar to that found according to the second model applied to the ellipsometry experiments.

A similar electrochemical behavior attributable to the coexistence of a 'lying-down' and 'standing-up' molecules was observed for Cys-T5-Fc and Cys-T7-Fc. In the cases of Cys-T3-Fc and Cys-T4-Fc, the presence of two different phases was not observed and a possible explanation described in discussion and conclusions (*vide supra*).

Measurement of k^0 for the 'standing up' subpopulation:

The standard heterogeneous electrochemical rate constant was determined by first making the 'lying down' subpopulation electrochemically silent and then studying the scan speed dependence of the 'standing up' phase. In this way, the 'lying down' phase does not interfere with the rate constant determination.

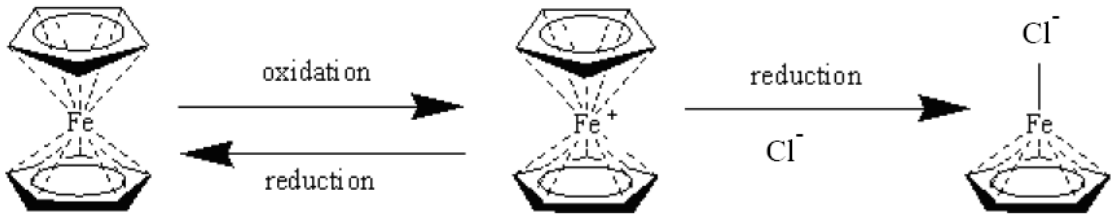

Figure 3.5 Ferrocene reaction during cyclic voltammetry cycles

The ferrocenium ion can exchange one of its cyclopentadienyl rings for an anion of the electrolyte solution (see Figure 3.5).[53] This exchange is slow and not significant when the electrolyte solution contains perchlorate, but it is much faster with chloride or sulfate anions.[53] By exploiting the difference in the oxidation kinetics for the 'lying down' and 'standing up' species, it is possible to preferentially react the 'lying down' species with chloride ion.

The protocol for preferentially destroying the 'lying-down' species by the reaction with chloride was to scan the PNA SAM coated electrode to potentials between 0.35 V and 0.65 V in 1 M NaCl solution at scan rates of 1 V/s for Cys-T6-Fc and Cys-T7-Fc, and at 10 V/s for Cys-T5-Fc, until the voltammetric peak of the 'lying-down' species

disappeared. Scanning at higher scan speed did not destroy the ferrocene of the 'standing-up' species, because oxidation of the 'standing-up' ferrocene is too slow. Subsequent to this process, the NaCl electrolyte was replaced with a $NaClO_4$ electrolyte and voltammetry was used to determine the electron transfer rate constant k^0 for the 'standing-up' species without interference

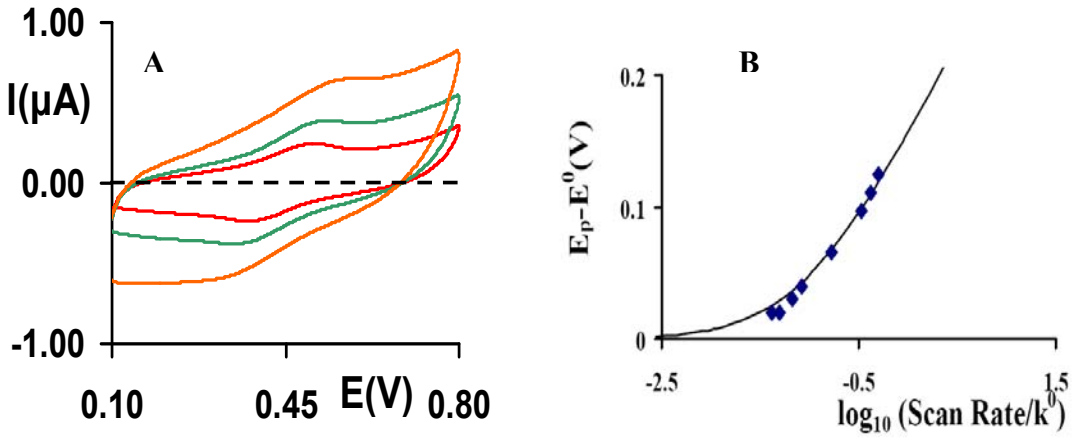

Figure 3.6 (A) Cyclic voltammograms are shown for Cys-T6-Fc SAM at scan rates 5 mV/s (red), 10 mV/s (green) and 20 mV/s (orange). (B) A fitting curve is plotted for the determination of electron transfer rate of Cys-T6-Fc SAM. The diamond symbols represent the experimentally determined points and the solid line represents the best fit theoretical curve.

The results of a voltammetry study of the 'standing-up' species of the Cys-T6-Fc films are shown in Figure 3.6, after the redox species in the 'lying-down' phase were destroyed. The voltammograms in Figure 3.6 (A) show that as the voltammetric scan speed increases, the voltammetric peak maxima shift away from the formal potential. Figure 3.6 (B) plots the dependence of the oxidation peak potential on the scan speed and compares it to the prediction of the Marcus theory,[55,56] in which the electron transfer rate k^0 was used as an adjustable parameter and the reorganization energy for ferrocene was taken to be 0.8 eV.[58] The voltammograms and fitting curves of other PNA SAMs are shown in the Supporting Information.

Table 3.3 Electron Transfer Rate and Coverage for the 'standing-up' population of PNA SAMs

Molecule	k^0 (s^{-1})	Coverage ($pmol/cm^2$)	FWHM* (mV)	No of trials
Cys-T3-Fc	2000 ± 200	89 ± 8	115 ± 3 (1 V/s)	5
Cys-T4-Fc	200± 20	87 ± 7	116 ± 3 (0.1 V/s)	9
Cys-T5-Fc	3.0 ± 0.5	47 ± 3	106 ± 4 (0.01 V/s)	3
Cys-T6-Fc	0.14 ± 0.03	144 ± 60	129 ± 4 (0.005 V/s)	5
Cys-T7-Fc	0.018 ± 0.002	80 ± 13	188 ± 6 (0.005 V/s)	4

* *The scan speeds at which FWHMs are calculated are reported in parenthesis.*

The k^0 values determined from the oxidation and reduction waves were different, with those for reduction being consistently 1.5 times larger than those for oxidation (Table 3.3). It is likely that this asymmetry in the electron transfer rate arises from ion pairing of the surface bound ferrocenium with the anion of the electrolyte solution, as reported by others.[72] Alternatively, interactions between redox centers can cause such asymmetries.[61] For simplicity, the discussion focuses on the oxidation waves as others have done for alkanethiol-ferrocene assemblies.[58,73]

The full width at half maximum (FWHM) for different PNA molecules are listed in Table 3.3. For Cys-T6-Fc and Cys-T7-Fc, electrochemical reversibility was not achieved even at the slowest scan speed, because the electron transfer rates were very slow. Simulations of the voltammograms for Cys-T6-Fc and Cys-T7-Fc at a scan speed of 0.005 V/s gave a FWHM of 106 mV for Cys-T6-Fc and 124 mV for Cys-T7-Fc. As Table 3.3 shows, the experimental FWHM for shorter PNA oligomers are somewhat broader

than the ideal limit of a homogeneous film (90.6 mV). This result may be attributed to interaction between redox centers[74] or to the inhomogeneity of the films.[61]

Distance Dependence of k^0 through PNA:

The electron transfer rate constant for the 'standing-up' phase decreases as the number of thymine nucleotides in the PNA chain increases. This exponential dependence revealed by Figure 3.7 is consistent with a charge transfer that occurs by a superexchange mechanism.[9-19] The slope of the line gives a tunneling decay constant of $\beta = 0.86 \pm 0.04$ $Å^{-1}$ ($\beta = 3.0 \pm 0.1$/ Base),[75] which is comparable to the tunneling decay constants reported for alkanethiols[63,73,76-78] and for peptides.[79,80]

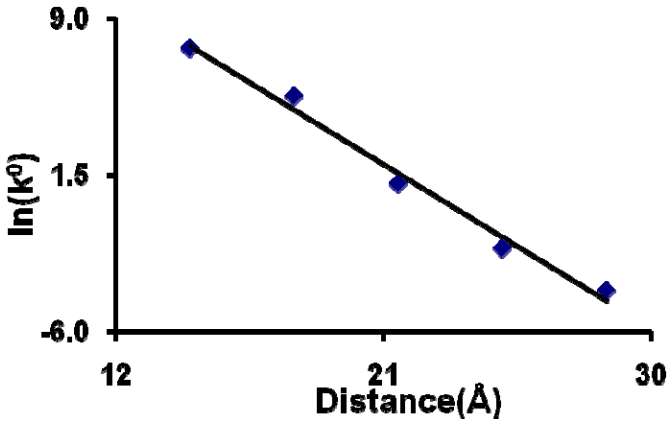

Figure 3.7 Electron transfer rate of PNA molecules are plotted as a function of the distance between gold electrode and ferrocene (blue diamond symbols) (error bars are smaller than symbols). The solid line represents the best fit line used for the determination of the tunneling decay constant (β) for thymine (T) containing single stranded PNA molecules.

3.6 Discussion and Conclusions

In this work single stranded peptide nucleic acid oligomers consisting of thymine bases were self-assembled on a gold surface. In order to obtain a high coverage and compact films the assembly was performed at 35°C to 40°C. The SAM was characterized by SAMDI-ToF mass spectrometry, cyclic voltammetry, atomic force microscopy,

contact angle and ellipsometry measurements. Electrochemistry detected two distinct populations of molecules in the PNA SAM, one consisting of 'lying-down' molecules with a fast electron transfer rate and the other of 'standing-up' molecules with a slow electron transfer rate. The AFM studies of Cys-T6-Fc also revealed that ss-PNA SAM is composed of 'lying-down' and 'standing-up' species. Hence the second model of ellipsometry was deemed more appropriate for this study. The percentage of 'lying-down' molecules varied with the oligonucleotide length (number of T bases) of the PNA. According to cyclic voltammetry, percentages of the 'lying-down' molecules were 27±5% 10±3% and 9±2% for Cys-Tn-Fc, where n=5-7 respectively, whereas according to the second model of ellipsometry the percentage of 'lying-down' molecules were 14.1±2.0%, 16.0±1.4%, 18.5±1.7%, 9.7±1.0% and 8.7±1.2% for Cys-Tn-Fc, where n= 3-7 respectively.

In contrast to the cases of Cys-T5-Fc, Cys-T6-Fc, and Cys-T7-Fc, the presence of two subpopulations of ferrocene was not apparent in the voltammetry of Cys-T3-Fc and Cys-T4-Fc assemblies. Nevertheless, the ellipsometry measurements suggested that some of the PNA molecules were 'lying-down' on these surfaces. The failure to observe two phases in the voltammetry of Cys-T3-Fc and Cys-T4-Fc, could be caused by the fact that the rate constants for the 'lying-down' and 'standing-up' phases are not different enough to generate to distinguishable peaks in cyclic voltammetry. Presumably the electron transfer rate of the 'standing-up' species of Cys-T3-Fc and Cys-T4-Fc are much higher than that of Cys-T5-Fc, Cys-T6-Fc or Cys-T7-Fc, and thus the voltammetric peak starts to shift at higher scan speeds; this makes the analysis more difficult because the rate of the 'standing-up' phase is closer to the rate of the 'lying-down' phase.

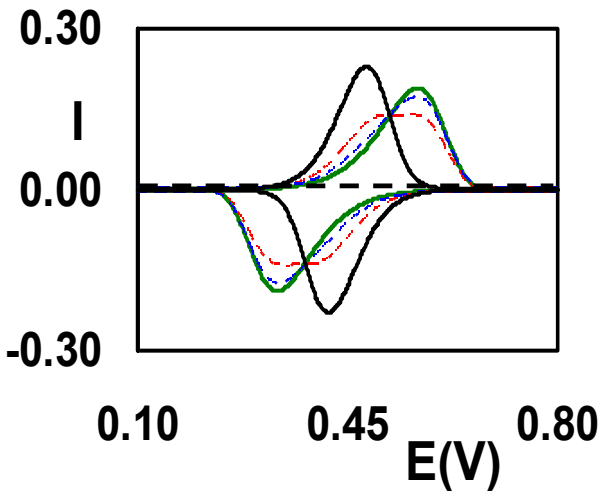

Figure 3.8 Simulated voltammograms obtained for four different cases at scan rate 100 V/s. Solid green and black voltammograms are for species having k^0 = 200 s^{-1} and k^0= 1800 s^{-1} respectively. Dotted blue and red voltammograms are for 9:1 ratio and 7:3 ratio of two species, having k^0 = 200 s^{-1} and k^0 = 1800 s^{-1} respectively.

Simulated voltammograms[81] were used to assess how 'lying-down' molecules of Cys-T3-Fc and Cys-T4-Fc impact the observations (Figure 3.8). If two species are present at a 9:1 ratio (blue voltammogram) with a significant difference in k^0 (9 times), the peak for the majority species ('standing-up') dominates the response over the minority ('lying-down'), i.e. the voltammetric peaks remain at the same position where majority species ('standing-up' species) (green voltammogram) have a peak, even if 10-15% molecules have a faster electron transfer rate. These simulated voltammograms do not consider background charging, however the background charge was relatively low for the Cys-T3-Fc and Cys-T4-Fc films (see supporting information). However, the red voltammogram of Figure 3.8 shows that if the ratio is increased to 7:3, then a peak maximum appears in between the majority ('standing-up') (green voltammogram) and minority ('lying-down') species (black voltammogram). These simulated voltammograms imply that if 'lying-down' molecules are 10-15% of the total, then the k^0 obtained for the

Cys-T3-Fc and Cys-T4-Fc would not be affected significantly, but if the amount of 'lying-down' species is more than 20%, then k^0 will be affected and cause a somewhat lower k^0 than that reported here. Note that the ellipsometry data analysis according to our second model suggests that the percentage of 'lying down' species is below 20% for Cys-T3-Fc and Cys-T4-Fc.

These findings should be contrasted with those of Martin-Gago and coworkers who successfully formed a densely packed peptide nucleic acid (PNA) SAM by incubation of Au surfaces at room temperature. In their study, the PNA oligomers contained a 3 nm long linker between the PNA and the cysteine.[42-44] We performed an analogous assembly in which a β-alanine linker was placed between the PNA and the cysteine and found that dense compact films are formed on the electrode (data not shown). Because it slows down the charge transfer rate and controls the response, such long linkers are incompatible with the distance-dependent charge transfer studies pursued here.

By creating compact films and chemically destroying the 'lying-down' species, the slower electron transfer rate constant of the 'standing-up' species could be measured. The distance dependent charge transfer of the thymine (T) containing PNA SAMs had a tunneling decay constant similar to that of peptide linkages,[79,80] $\beta = 0.86 \pm 0.04$ Å^{-1}. Using this value and extrapolating to zero distance, *i.e.* to contact between ferrocene and the electrode, provided a maximum electron transfer rate constant of 5.8×10^8 s^{-1}. This value is similar to that obtained by Smalley et al.[63] for ferrocene terminated alkanethiol (6×10^8 s^{-1}). Using the semiclassical Marcus theory, a contact electronic coupling between the donor and acceptor of about 69 cm^{-1} is obtained. This value is small enough that the electron transfer can be reasonably modeled as nonadiabatic.

The electron transfer rate constant measured for the thymine-containing single stranded PNA molecules is slower than that reported for duplex DNA.[29-31,33] This difference could arise from the fact that the base stacking[82] which is important for long range charge transfer is weaker in ss-PNA compared to ds-DNA. It is worth to noting that such conclusion cannot be drawn based on the present study but it requires a detailed systematic study is required, which is underway in our laboratory. In the case of DNA, long range charge transfer has been explained by a hopping mechanism;[20-25] *i.e.,* thermal oxidation of the guanine (G) or adenine (A) bases competes with the tunneling when the bridge between the donor and acceptor is long.[25] Thymine is more difficult to oxidize so that the tunneling pathway remains dominant for longer oligomers, than what one would expect if G or A bases were present. Charge transport in the short thymine PNAs used here appears to operate by a single step super-exchange mediated tunneling mechanism.

3.7 Acknowledgements

We acknowledge support from the U.S National Science Foundation (CHE 0628169).

3.8 References and Notes:

(1) Schwartz, D. K. *Annu. Rev. Phys. Chem.* **2001**, *52*, 107-137.

(2) Ulman, A. *Chem. Rev.* **1996**, *96*, 1533-1554.

(3) Jortner, J.; Ratner, M. A. *Molecular Electronics;* Blackwell: London, **1997**.

(4) Kumar, A.; Biebuyck, H. A.; Whitesides, G. M. *Langmuir* **1994**, *10*, 1498-1511.

(5) Revell, D. J.; Knight, J. R.; Blyth, D. J.; Haines, A. H.; Russell, D. A. *Langmuir* **1998**, *14*, 4517-4524.

(6) Bain, C. D.; Evans, S. D. *Chem. Br.* **1995**, *31*, 46.

(7) Donhauser, Z. J.; Mantooth, B. A.; Kelly, K. F.; Bumm, L. A.; Monnell, J. D.; Stapleton, J. J.; Jr, D. W. P.; Rawlett, A. M.; Allara, D. L.; Tour, J. M.; Weiss, P. S. *Science* **2001**, *292*, 2303-2307.

(8) Prime, K. L.; Whitesides, G. M. *Science* **1991**, *252*, 1164-1167.

(9) Degama, A. A. S. *Theor. Chim. Acta.* **1985**, *68*, 159.

(10) Evenson, J. W.; Karplus, M. *Science* **1993**, *262*, 1247-1249.

(11) Gehlen, J. N.; Daizadeh, I.; Stuchebrukhov, A. A.; Marcus, R. A. *Inorganica Chimica Acta* **1996**, *243*, 271-282.

(12) Goldman, C. *Phys. Rev. A* **1991**, *43*, 4500.

(13) Harden, M. M. *J. Chem. Phys.* **1961**, *35*, 508-515.

(14) Joachim, C.; Ratner, M. A. *Nanotechnology* **2004**, *15*, 1065.

(15) Magoga, M.; Joachim, C. *Phys. Rev. B* **1997**, *56*, 4722.

(16) Priyadarshy, S.; Risser, S. M.; Beratan, D. N. *J. Phys. Chem.* **1996**, *100*, 17678-17682.

(17) Ratner, M. A. *J. Phys. Chem.* **1990**, *94*, 4877-4883.

(18) Reimers, J. R.; Hush, N. S. *J. Photochem. and Photobiol. A: Chemistry* **1994**, *82*, 31-46.

(19) Remacle, F.; Levine, R. D. *J. Phys. Chem. B* **2001**, *105*, 2153-2162.

(20) Berlin, Y. A.; Burin, A. L.; Ratner, M. A. *Chem. Phys.* **2002**, *275*, 61-74.

(21) Berlin, Y. A.; Hutchison, G. R.; Rempala, P.; Ratner, M. A.; Michl, J. *J. Phys. Chem. A* **2003**, *107*, 3970-3980.

(22) Giese, B. *Ann. Rev. Biochem.* **2002**, *71*, 51-70.

(23) Jortner, J.; Bixon, M.; Langenbacher, T.; Michel-Beyerle, M. E. *Proc. Natl. Acad. Sci.* **1998**, *95*, 12759.

(24) Li, X. Q.; Zhang, H.; Yan, Y. *J. Phys. Chem. A* **2001**, *105*, 9563-9567.

(25) Schuster, G. B. *Long-Range Charge Transfer in DNA I. in Top. Curr. Chem. Vols 236 and 237;* Springer: NY, 2004.

(26) Casero, E.; Darder, M.; Diaz, D. J.; Pariente, F.; Martin-Gago, J. A.; Abruna, H.; Lorenzo, E. *Langmuir* **2003**, *19*, 6230-6235.

(27) Herne, T. M.; Tarlov, M. J. *J. Am. Chem. Soc.* **1997**, *119*, 8916-8920.

(28) Zhang, R. Y.; Pang, D. W.; Zhang, Z. L.; Yan, J. W.; Yao, J. L.; Tian, Z. Q.; Mao, B. W.; Sun, S. G. *J. Phys. Chem. B* **2002**, *106*, 11233-11239.

(29) Hartwich, G.; Caruana, D. J.; de Lumley-Woodyear, T.; Wu, Y.; Campbell, C. N.; Heller, A. *J. Am. Chem. Soc.* **1999**, *121*, 10803-10812.

(30) Liu, T.; Barton, J. K. *J. Am. Chem. Soc.* **2005**, *127*, 10160-10161.

(31) Kelley, S. O.; Boon, E. M.; Barton, J. K. *Angew. Chem. Int. Ed.* **1999**, *38*, 941.

(32) Chahma, M.; Lee, J. S.; Kraatz, H.-B. *J. Electroanal. Chem.* **2004**, *567*, 283-287.

(33) Long, Y. T.; Li, C. Z.; Sutherland, T. C.; Chahma, M.; Lee, J. S.; Kraatz, H. B. *J. Am. Chem. Soc.* **2003**, *125*, 8724-8725.

(34) Egholm, M.; Buchardt, O.; Christensen, L.; Behrens, C.; Freier, S. M.; Driver, D. A.; Berg, R. H.; Kim, S. K.; Norden, B.; Nielsen, P. E. *Nature* **1993**, *365*, 566-568.

(35) Egholm, M.; Nielsen, P. E.; Buchardt, O.; Berg, R. H. *J. Am. Chem. Soc.* **1992**, *114*, 9677-9678.

(36) Petersson, B.; Nielsen, B. B.; Rasmussen, H.; Larsen, I. K.; Gajhede, M.; Nielsen, P. E.; Kastrup, J. S. *J. Am. Chem. Soc.* **2005**, *127*, 1424-1430.

(37) Rasmussen, H.; Kastrup, J. S.; Nielsen, J. N.; Nielsen, J. M.; Nielsen, P. E. *Nature Struct. Biol.* **1997**, *4*, 98-101.

(38) Rasmussen, H.; Liljefors, T.; Petersson, B.; Nielsen, P. E.; Kastrup, J. S. *Journal of Biomolecular Structure & Dynamics* **2004**, *21*, 495-502.

(39) Franzini, R. M.; Watson, R. M.; Patra, G. K.; Breece, R. M.; Tierney, D. L.; Hendrich, M. P.; Achim, C. *Inorg. Chem.* **2006**, *45*, 9798-9811.

(40) Popescu, D. L.; Parolin, T. J.; Achim, C. *J. Am. Chem. Soc.* **2003**, *125*, 6354-6355.

(41) Watson, R. M.; Skorik, Y. A.; Patra, G. K.; Achim, C. *J. Am. Chem. Soc.* **2005**, *127*, 14628-14639.

(42) Briones, C.; Mateo-Marti, E.; Gomez-Navarro, C.; Parro, V.; Roman, E.; Martin-Gago, J. A. *Phys. Rev. Lett.* **2004**, *93*, 208103.

(43) Briones, C.; Mateo-Marti, E.; Gomez-Navarro, C.; Parro, V.; Roman, E.; Martin-Gago, J. A. *J. Mol. Catalysis A: Chemical* **2005**, *228*, 131-136.

(44) Mateo-Marti, E.; Briones, C.; Roman, E.; Briand, E.; Pradier, C. M.; Martin-Gago, J. A. *Langmuir* **2005**, *21*, 9510-9517.

(45) Seidel, C. A. M.; Schulz, A.; Sauer, M. H. M. *J. Phys. Chem.* **1996**, *100*, 5541-5553.

(46) Azzam, R. M. A.; Bashara, N. M. *Ellipsometry and Polarized Light;* North- Holland publishing Company: Amsterdam, 1977.

(47) Tompkins, H. G. *A User's Guide to Ellipsometry;* Academic Press Inc.: MA, 1993.

(48) Anderson, G. W.; McGregor, A. C. *J. Am. Chem. Soc.* **1957**, *79*, 6180-6183.

(49) McKay, F. C.; Albertson, N. F. *J. Am. Chem. Soc.* **1957**, *79*, 4686-4690.

(50) Nielsen, P. E. *Peptide Nucleic Acids: Protocols and Applications;* Horizon Bioscience: UK, Wymondham, 2004.

(51) Sawyer, D. T.; Sobkowiak, A.; Roberts, J. L. *Experimental Electrochemistry for Chemists; Wiley, NY, 1995.*

(52) Patrie, S. M.; Mrksich, M. *Anal. Chem.* **2007**, *79*, 5878-5887.

(53) Finklea, H. O. *In Electroanalytical Chemistry; Bard, A. J., Rubinstein, I., Eds.;* Marcel Dekker Inc.: NY, 1996, 19, 109.

(54) Khoshtariya, D. E.; Dolidze, T. D.; Zusman, L. D.; Waldeck, D. H. *J. Phys. Chem. A* **2001**, *105*, 1818-1829.

(55) Marcus, R. A. *J. Chem. Phys.* **1956**, *24*, 966-978.

(56) Marcus, R. A. *J. Chem. Phys.* **1965**, *43*, 679-701.

(57) Miller, C. J. *Physical Electrochemistry: Principles, Methods and Applications. Rubinstein, I, Ed.;* Marcel Dekker Inc.: NY, 1995, 27.

(58) Napper, A. M.; Liu, H.; Waldeck, D. H. *J. Phys. Chem. B* **2001**, *105*, 7699-7707.

(59) Wei, J.; Liu, H.; Dick, A. R.; Yamamoto, H.; He, Y.; Waldeck, D. H. *J. Am. Chem. Soc.* **2002**, *124*, 9591-9599.

(60) Barbara, P. F.; Meyer, T. J.; Ratner, M. A. *J. Phys. Chem.* **1996**, *100*, 13148-13168.

(61) Bard, A. J.; Faulkner, L. R. *Electrochemical Methods; Fundamental and Applications; Wiley, NY, 1980.*

(62) Chidsey, C. E. D. *Science* **1991**, *251*, 919-922.

(63) Smalley, J. F.; Feldberg, S. W.; Chidsey, C. E. D.; Linford, M. R.; Newton, M. D.; Liu, Y.-P. *J. Phys. Chem.* **1995**, *99*, 13141-13149.

(64) Harrington, R. E. *J. Am. Chem. Soc.* **1970**, *92*, 6957-6964.

(65) Jung, L. S.; Campbell, C. T.; Chinowsky, T. M.; Mar, M. N.; Yee, S. S. *Langmuir* **1998**, *14*, 5636-5648.

(66) Wu, P. G.; Fujimoto, B. S.; Song, L.; Schurr, J. M. *Biophys. Chem.* **1991**, *41*, 217-236.

(67) The length of Cysteine, Ferrocene and each PNA base has been calculated by CAChe software. Geometry has been optimized by PM3 method.

(68) Ehler, T. T.; Malmberg, N.; Noe, L. J. *J. Phys. Chem. B* **1997**, *101*, 1268-1272.

(69) Porter, M. D.; Bright, T. B.; Allara, D. L.; Chidsey, C. E. D. *J. Am. Chem. Soc.* **1987**, *109*, 3559-3568.

(70) Assuming that ssPNA has a radius similar to ssDNA, the radius of ssPNA is taken as 4.9 Å. Mucic, R. C.; Herrlein, M. K.; Mirkin, C. A.; Letsinger, R. L. *Chem. Commun.* **1996**, *4*, 555-557.

(71) Anne, A.; Demaille, C. *J. Am. Chem. Soc.* **2006**, *128*, 542-557.

(72) Rowe, G. K.; Creager, S. E. *Langmuir* **1991**, *7*, 2307-2312.

(73) Weber, K.; Hockett, L.; Creager, S. *J. Phys. Chem. B* **1997**, *101*, 8286-8291.

(74) Peng, Z.; Qu, X.; Dong, S. *J. Electroanal. Chem.* **2004**, *563*, 291-298.

(75) This error is a 2σ error in the slope obtained by a weighted linear least square fit and assuming no error in the distance values for the films.

(76) Carter, M. T.; Rowe, G. K.; Richardson, J. N.; Tender, L. M.; Terrill, R. H.; Murray, R. W. *J. Am. Chem. Soc.* **1995**, *117*, 2896-2899.

(77) Slowinski, K.; Chamberlain, R. V.; Miller, C. J.; Majda, M. *J. Am. Chem. Soc.* **1997**, *119*, 11910-11919.

(78) Sumner, J. J.; Weber, K. S.; Hockett, L. A.; Creager, S. E. *J. Phys. Chem. B* **2000**, *104*, 7449-7454.

(79) Sek, S.; Sepiol, A.; Tolak, A.; Misicka, A.; Bilewicz, R. *J. Phys. Chem. B* **2004**, *108*, 8102-8105.

(80) Tao, N. *J. Mater. Chem.* **2005**, *15*, 3260 - 3263.

(81) Simulated voltammograms are generated by CH Instruments (Austin, TX) software package.

(82) Jacobsen, E. N. *Comprehensive Organometallic Chemistry II, Vol. 12;* Permagon: NY, 1995, p.1097, and reference therein.

3.9 Supporting Information

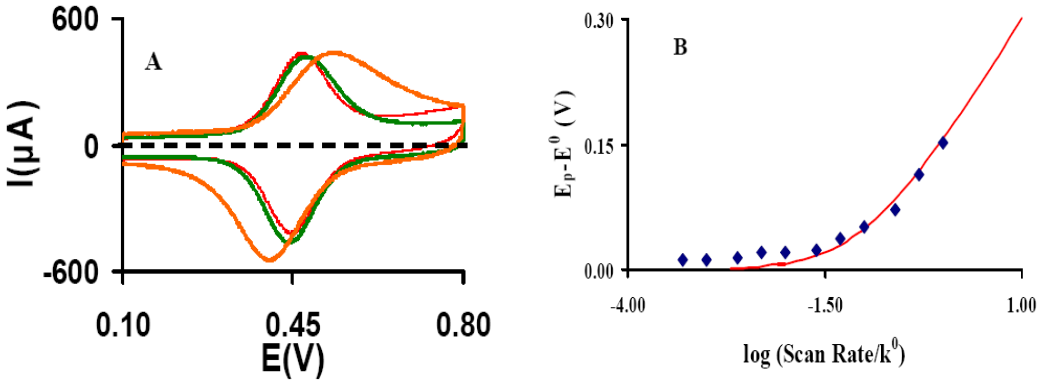

Figure 3.9 (A) Three cyclic voltammograms are shown for Cys-T3-Fc SAM at scan rates 1 V/s (Red), 10 V/s (Green) and 500 V/s (Orange). (B) A fitting curve is plotted for the determination of electron transfer rate of Cys-T3-Fc SAM.

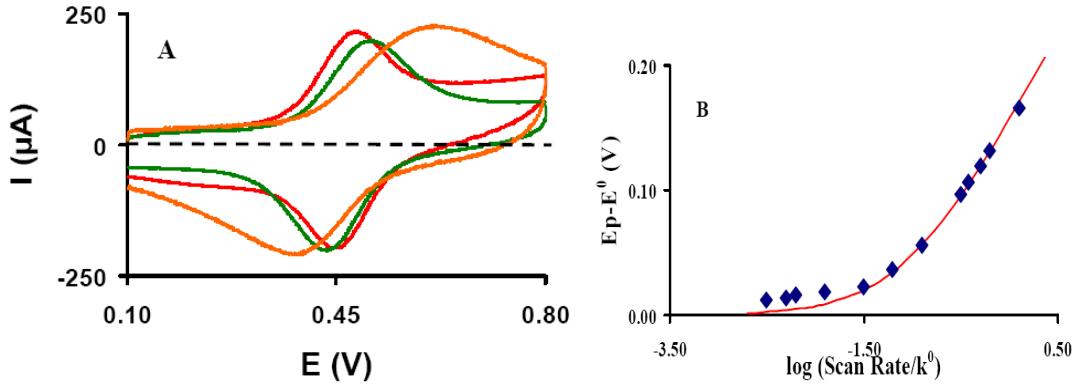

Figure 3.10 (A) Three cyclic voltammograms are shown for Cys-T4-Fc SAM at scan rates 1 V/s (Red), 10 V/s (Green) and 100 V/s (Orange). (B) A fitting curve is plotted for the determination of electron transfer rate of Cys-T4-Fc SAM.

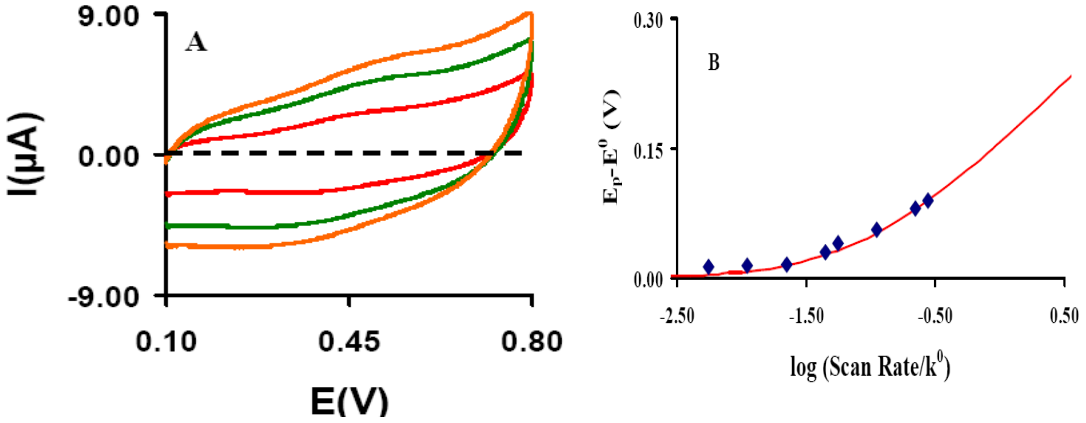

Figure 3.11 (A) Three cyclic voltammograms are shown for Cys-T5-Fc SAM at scan rates 80 mV/s (Red), 200 mV/s (Green) and 400 mV/s (Orange). (B) A fitting curve is plotted for the determination of electron transfer rate of Cys-T5-Fc SAM

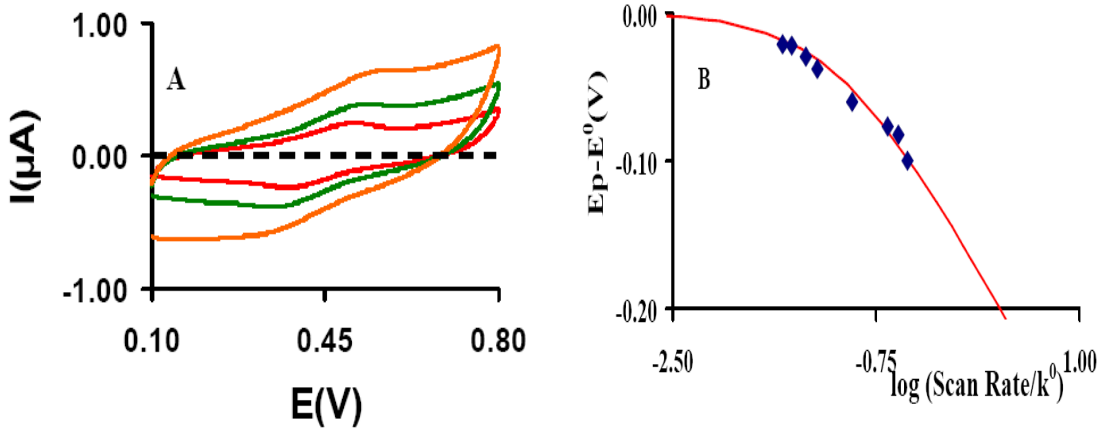

Figure 3.12 (A) Three cyclic voltammograms are shown for Cys-T6-Fc SAM at scan rates 5 mV/s (Red), 10 mV/s (Green) and 20 mV/s (Orange). (B) A fitting curve for the reduction wave is plotted for the determination of electron transfer rate of Cys-T6-Fc SAM. The fitting curve for oxidation wave is shown in main manuscript. The electron transfer rate for the reduction wave is found to be 1.5 times larger than the oxidation wave.

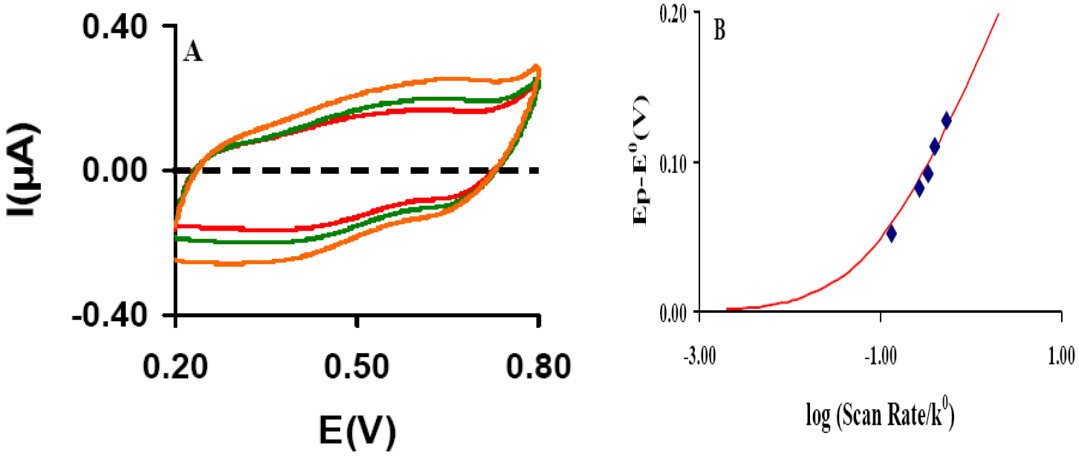

Figure 3.13 (A) Three cyclic voltammograms are shown for Cys-T7-Fc SAM at scan rates 5 mV/s (Red), 6 mV/s (Green) and 8 mV/s (Orange). (B) A fitting curve is plotted for the determination of electron transfer rate of Cys-T7-Fc SAM.

Characterization of PNA-Fc Products

Table 3.4 Calculated masses of PNA molecules and corresponding m/z observed from MALDI-ToF MS (reflection mode, α-cyano-4-hydroxycinnamic acid matrix, laser intensity 2300).

Molecule	Expected Mass (Da)	Observed *m/z*
H_2N-Cys-T3-Fc (+ Na^+)*	1153.99	1154.0
H_2N-Cys-T4-Fc (+ Na^+)	1420.25	1419.4
H_2N-Cys-T5-Fc (+ Na^+)	1686.51	1686.0
H_2N-Cys-T6-Fc (+ Na^+)	1952.77	1951.4
H_2N-Cys-T7-Fc (+ Na^+)	2219.03	2218.2

*The most intense peak corresponds to the mass of the molecule plus the mass of a sodium ion. This is most likely due to the propensity of T to tautomerize to the imidic acid form, which associates with Na^+ after deprotonation. Cys-Tn-Fc sequences often exhibited binding to 1 to n sodium ions (Figure 3.14).

Verification of Ferrocene Stability in SAMs

PNA solutions used to incubate electrodes for 6 hours or more were characterized by MALDI-ToF MS after the incubation was complete. This analysis

revealed that some of the PNA-coupled ferrocene in solution had decomposed over the course of the incubation by losing the Fe ion as well as one of the cyclopentadienyl (Cp) rings (Figure 3.14).

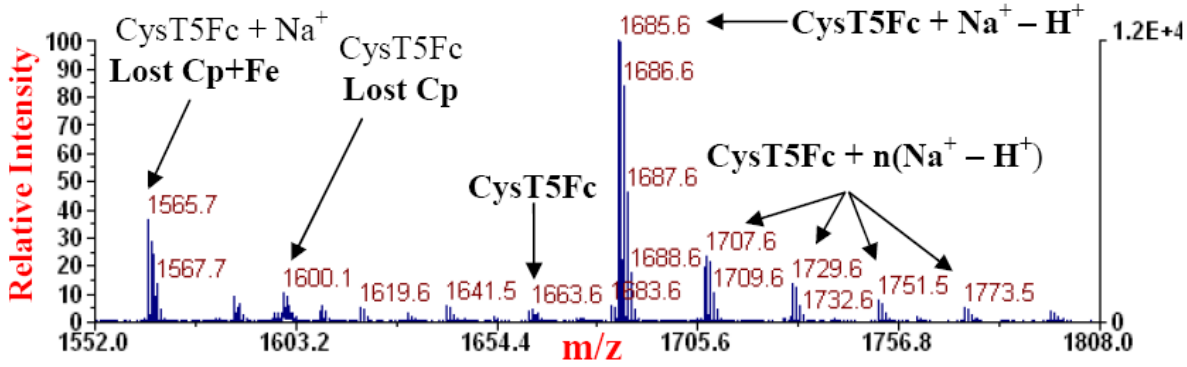

Figure 3.14 MALDI-ToF spectrogram of a solution of Cys-T5-Fc (20 μM PNA in 1:1 acetonitrile:water with 10 mM sodium phosphate buffer, pH 7.0) used to incubated CV electrodes for 6 hours.

SAMDI-ToF MS[52], a method used to analyze self-assembled monolayers by MALDI, was employed to determine whether decomposition occurred for molecules adsorbed onto the Au surface. Thin gold-coated glass slides were rinsed 3 times with ethanol and DI water and then dried under nitrogen. Small shards of these slides were incubated in PNA solutions (20 μM in 1:1 acetonitrile:water with 10 mM sodium phosphate buffer, pH 7.0) under the same conditions as CV electrodes (see manuscript. Briefly: 35-40°C for up to 48 h). Then 1.5 microliters of a solution containing 5 mg of

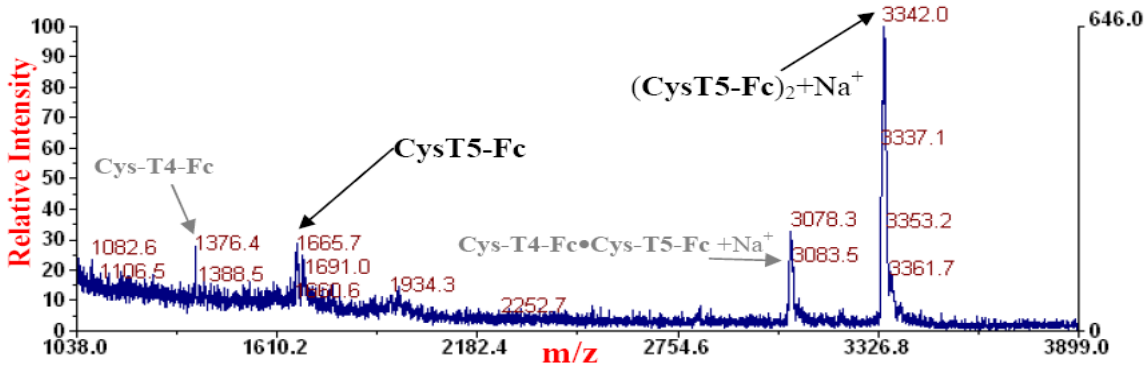

Figure 3.15 MALDI-ToF spectrogram of a Cys-T5-Fc SAM formed by incubation of a gold slide shard in a 200 μM PNA solution. The higher molecular weight species represent disulfide dimers that commonly form during the SAMDI technique. There is no indication of decomposed species which would have masses of 1565 (–CpFe), 1598 (–Fe), or of disulfide dimers formed between any combination of these decomposed species and the intact species, with or without sodium. (Cys-T4-Fc was a minor impurity in this sample, and does not represent a decomposed species)

2,4,6-trihydroxyacetophenone (THAP) in 1 mL acetonitrile (HPLC grade) was pipetted onto the gold shards. Once dry, the slides were attached to a MALDI plate (stainless steel Voyager plate with surface indent, part V700698, Applied Biosystems) by doubled-sided tape (Scotch) and analyzed using an Applied Biosystems Voyager DE Workstation (linear mode; laser intensity: 3031, accelerating voltage: 20000V, grid voltage: 68%, extraction delay: 250 nsec). Two PNA molecules were tested (Cys-T7-Fc and Cys-T5-Fc), and in both cases, MALDI spectrograms displayed peaks corresponding only to the molecular mass (*M*) of Cys-Tn-Fc. Peaks corresponding to $M+Na^+$, $M+K^+$, $M+Au^+$, and their disulfide dimers were also observed, which is common for this technique. However there was no indication of decomposition of any ferrocene bound to the surface by PNA (Figure 3.15).

Chapter 4 Charge Transfer Mechanism Switchover from Superexchange to "Hopping" in Peptide Nucleic Acid

Amit Paul,[a] Richard M. Watson,[†] Emil Wierzbinski,[a] Paul Lund,[†]

Kathryn L. Davis,[a] Helen Wei, [†] Catalina Achim,[†] David H. Waldeck[a]

Department of Chemistry, University of Pittsburgh, PA, 15260[a]

Department of Chemistry, Carnegie Mellon University, Pittsburgh, PA, 15213[†]

4.1 Abstract

Charge transfer studies have been performed for self-assembled monolayers (SAMs) of single-stranded and double-stranded peptide nucleic acids (PNAs), having a C-terminus cysteine and an N-terminus ferrocene group. For short single-stranded PNA molecules, a strong decay with distance is observed and for long chain PNA molecules a weak decay with distance is observed. These observations are consistent with a transition in the charge transport mechanism from super-exchange mediated tunneling for short chains to a "hopping" mechanism for long chains. The experimentally determined critical base number for the mechanism switchover is found to be in good agreement with a tight-binding model proposed earlier.

4.2 Introduction

The mechanism of charge transfer through deoxyribonucleic acid (DNA) has been one of the more highly debated topics in the scientific community during the past decade.[1-19] Barton and coworkers initiated the debate in the 1990's, when they first reported that DNA is a "molecular wire".[1,11,14,18] Questions about whether DNA is a molecular wire and the mechanism of its charge transport, e.g. through its "π-stack" or not, has been investigated by a number of groups. The debate also sparked interest in the

nature of charge transfer through self-assembled monolayers (SAMs)[20,21] of nucleic acids and their potential applications in the field of molecular electronics.[22] A detailed understanding of the charge transport through such SAMs is needed to realize their potential for applications in molecular electronics.

Giese and coworkers have studied hole transfer between guanines (G) in DNA by varying the number of Adenine-Thymine (A-T) base pairs between G bases.[4,6,7,13] They have shown that if the number of intervening (A-T) base pairs is ≤ 3 then the (A-T) base pair acts as a bridge and is not oxidized during single step hole transfer but when the number of (A-T) base pairs is ≥ 3 endothermic oxidation of the adenine occurs and the hole migrates by a hopping process over the adenines until it reaches the next guanine base. Their findings imply that charge transfer through DNA follows two different mechanisms. At short distance charge transfer follows a super-exchange mechanism,[23-33] in which the charge tunnels from the first site to the last site by a single coherent jump; this mechanism has an exponential distance decay and is not effective beyond a few nanometers. For longer distance transport, the charge "hops through bridging sites" (i.e. intervening base pairs in DNA). Lewis and coworkers looked at the hole transport dynamics from a primary hole donor to a secondary hole acceptor over short distance.[16,34] Their results show that the rate constant increases as the hole transport becomes more exergonic. Their results indicate that the hole transport rates are very fast so that the charge can migrate through the bridging sites before other chemical reactions occur on the oxidized base pairs.

The detailed nature of the long distance transport remains under discussion and a number of different models have been proposed. According to the incoherent multi-step

hopping mechanism,[3,4,6,7,9,10,12,13,16,19,35] the charge diffuses from the donor to the acceptor and is localized on individual "hole resting sites"; modeled as a one dimensional random walk with an absorbing sink at the acceptor. Schuster and coworkers proposed a "polaron like" hopping mechanism,[2,5,8,15-17] where local energy-lowering structural distortions generate a self-trapped state of finite extent that migrates from one location to another by thermal (phonon) activation. So far most of the ds DNA charge transfer studies show that the guanine (G) and adenine (A) nucleobases act as hole resting sites,[16] i.e. charge can pause briefly on G or A, since their oxidation potentials are lower than that of their partners thymine (T) and cytosine (C). Recently Joy et al.[36] have shown that a radical cation of thymine (T) can act as a resting site and charge can hop through thymines to facilitate long range charge transfer.

Though charge transfer through DNA has been broadly investigated in the past decade, most of these studies were in solution. Very few studies have been performed on self-assembled monolayers (SAMs) of DNA, because of the difficulties in creating well-defined DNA assemblies on a metal surface.[37-39] An alternative to DNA for realizing nucleic acid SAMs and their potential application in molecular electronics is peptide nucleic acid (PNA). PNA is an analogue of DNA that has a neutral and achiral backbone based on aminoethylglycine, in contrast to the negatively-charged and chiral backbone of DNA (Figure 4.1(A) and (C)).[40,41] The neutral backbone of PNA makes it a promising candidate for monolayer self-assembly. PNA forms duplexes with itself and also with DNA by Watson-Crick base pairing. PNA·PNA duplexes adopt a helical structure termed P-type, which have a large pitch with 18 bases/turn, a diameter of 28 Å, and a 3.2-3.4 Å rise/base pair.[42-44] Although the backbone of PNA is achiral, chirality can be induced by

introducing chiral amino acids in PNA.[45] Moreover, ligand modified PNA can be used as a scaffold for transition metal ions at specified positions.[46-48] It is hoped that such metal containing PNA may facilitate charge transfer over tens of nanometers, in a manner similar to that in which metal cofactors mediate charge transfer in metalloproteins.

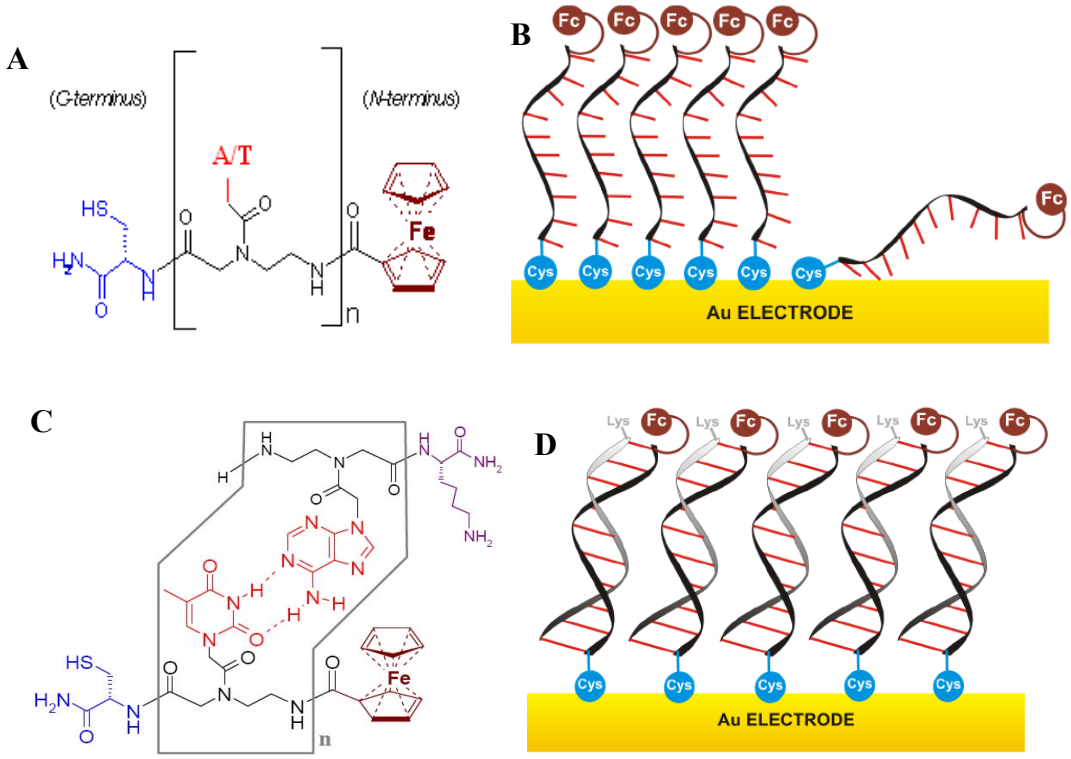

Figure 4.1 Panel A shows the chemical structure of thymine/ adenine containing ss-PNA that has a C-terminus cysteine and an N-terminus ferrocene, where n =3-10. Panel B shows a schematic representation of ss-PNA molecules self-assembled on a gold surface, in which blue circle represents cysteine, the black curl represents the PNA backbone, red lines represent A or T nucleobase, and the light brown circle represents ferrocene. Panel C shows the chemical structure of (A-T) ds-PNA that has a C-terminus cysteine and an N-terminus ferrocene, where n =7-10, 15. Panel D shows a schematic representation of ds PNA molecules self-assembled on a gold surface, in which the blue circle represents cysteine, the black curl represents the PNA backbone, red lines represent the A- T nucleobase pair and the light brown circle represents ferrocene.

In this work, PNA SAMs were grown on gold electrodes. PNA with a ferrocene redox probe covalently attached at its N-terminus was immobilized on a gold surface through a cysteine group at its C-terminus (Figures 4.1(B) and (D)). This study investigated the charge transfer of three different types of PNA assemblies: i) single-stranded thymine PNA (Cys-(T)n-Fc), ii) single-stranded adenine PNA (Cys-(A)n-Fc) and iii) double-stranded adenine-thymine PNA (Duplex-Cys-(A-T)n-Fc) where both cysteine and ferrocene was attached on the thymine strand. The length of the PNA oligomers was varied by increasing the number of nucleobases. Cyclic voltammetry (CV) was used to measure the charge transfer rate between a gold electrode and the ferrocene redox reporter at the terminus of the PNA chain. Ellipsometry[49,50] was used to measure the film thicknesses. This work shows that for short chain ss-PNA molecules, the charge transfer rate falls rapidly with increasing chain length and is consistent with a super-exchange mediated tunneling mechanism; however, when the chain length is long enough, the charge transfer rate has a weaker distance dependence and is consistent with a multi-step hopping mechanism. The transition between the two regimes is compared with a tight-binding model[3] that was proposed earlier. In addition, this study shows that charge hopping is also possible when the nucleobase is thymine.

4.3 Experimental

PNA synthesis: PNA oligomers were synthesized by solid phase peptide synthesis using the Boc protection strategy.[51-53] MBHA resin (Peptides International, Louisville, KY) with a loading of 0.18 mEquiv/g was down-loaded (see reference 53 for more detail about this procedure) using Boc-L-Cys-(4-MeOBzl)-OH or Boc-L-Lys-(4-MeOBzl)-OH (NovaBiochem/Merck Biosciences, Switzerland) to an estimated loading of 0.04-0.06

mEquiv/g. Thereafter Boc-T-OH or Boc-A-OH PNA monomers (Applied Biosystems, Foster City, CA) were coupled using 1H-Benzotriazolium 1-[*bis*(dimethylamino) methylene]-5chloro-hexafluorophosphate (1),3-oxide (HCTU) (Peptides International) as a coupling agent to create oligonucleotide of the desired length (3-10, 15). Finally, ferrocenecarboxylic acid (Aldrich) was coupled to the N-terminus; this last step was repeated twice to increase the yield of ferrocene-conjugated PNA. Oligomers were cleaved from the resin using trifluoroacetic acid (TFA) and trifluoromethanesulfonic acid (TFMSA), precipitated in ethyl ether, and dried under nitrogen. The solid products were dissolved in 15% acetonitrile aqueous solution and purified by reverse-phase HPLC using a solvent gradient, from 15% to 35% acetonitrile in water over 40 minutes on a Waters Delta 600 pump with a 2996 photodiode array detector (Milford, MA). PNA oligomers were characterized by MALDI-ToF mass spectrometry on an Applied Biosystems Voyager-DE STR Workstation.

PNA solutions were prepared in deionized water and the PNA concentrations were determined by UV-Vis spectrophotometry assuming ε_{260} = 8600 and 13700 cm^{-1} M^{-1} for each T and A monomer respectively.[53] PNA solutions for electrode incubation were typically 20 μM ssPNA in 10 mM pH 7.0 sodium phosphate buffer solution that was a 50% acetonitrile/50% water mixture. Double-stranded PNA samples were prepared by heating 20 μM Cys-(T)n-Fc and 20 μM Lys-(A)n PNA at 95°C and then slowly cooling down to room temperature. The melting temperature of duplex PNAs were determined by UV-Vis spectrophotometry and are reported in Table 4.1. The data in Table 4.1 shows that as the number of base pairs increases the melting temperature increases, as expected.

Duplex-Cys-(A-T)6-Fc is not stable enough to study, hence duplex-Cys-(A-T)7-Fc was the shortest duplex used here.

Table 4.1 Melting Temperature of Duplex PNA molecules:

Molecule	Melting Temperature in 50% ACN/ 50% water mixture (°C)
Duplex Cys (A-T)6-Fc	26
Duplex Cys (A-T)7-Fc	39
Duplex Cys (A-T)8-Fc	47
Duplex Cys (A-T)9-Fc	57
Duplex Cys (A-T)10-Fc	64

Electrode Preparation: A gold wire (0.5 mm diameter, 99.999%, Alfa Aesar, MA) was cleaned by reflux in nitric acid (70%) at 130°C for two hours and then washed with deionized water (>18 MΩ. cm). The wire was sealed in a soft-glass capillary tube with the tip exposed. The tip of the gold wire was heated to form a ball. The gold ball was reheated in a flame until glowing, then slowly cooled down and finally quenched in deionized water. This annealing process was repeated more than fifteen times until a smooth ball electrode was obtained. The area of the electrode was determined electrochemically[54] and found to be typically ~0.1 cm^2.

Self Assembled Monolayer (SAM) Preparation: Self-assembled monolayers of ss-PNA and ds-PNA molecules were prepared by incubating gold ball electrodes in 1 mL of a 20 μM PNA solution for 28-40 hours at 35-40°C and at 27°C respectively. After incubation the gold electrodes were washed with nanopure water and directly used in the electrochemical studies.

Mixed Duplex PNA/n-Octadecanethiol Self-Assembled Monolayer Preparation: The mixed duplex PNA/alkanethiol SAMs were prepared by a two-step process. Gold electrodes were covered by a submonolayer of duplex PNA, which was formed during overnight incubation (27°C) of the electrodes in the acetonitrile/water/ethanol (1: 1: 2) solution containing the desired PNA sequence at 5 μM concentration. To complete the monolayer with a octadecanethiol matrix, we adopted the method of the preparation of electrooxidation of alkylthiosulfates proposed by Lee et al.[55] The details of the mixed monolayer preparation are provided in the supporting information.

Electrochemical Measurements: Cyclic voltammetry was carried out on a CH Instrument Electrochemical Analyzer 618B (Austin, TX). The three-electrode electrochemical cell consisted of an Ag/AgCl (3 M/ 1 M KCl) reference electrode, a platinum wire as counter electrode, and a SAM-coated gold ball electrode as the working electrode. All experiments were performed in 1.0 M $NaClO_4$ (pH=7-8) aqueous electrolyte solution at room temperature. The uncompensated solution resistance was measured by AC impedance and found to be less than 5 Ω, so that the iR drop was not important for these measurements. The coverage of the PNA-ferrocene SAM was calculated by integrating the charge under the voltammetric peaks.

Ellipsometry: The molecules were self-assembled to form a monolayer thick film on evaporated gold slides (EMF Corp, Ithaca, NY). The Au slides were 0.7 inch x 0.3 inch x 0.062 inches in size and consisted of about 100 nm Au over a 50 nm thick Ti binder layer on float glass. The gold slides were cleaned by immersion in "piranha" solution (1:3 H_2O_2 and 98% H_2SO_4) **(Caution! The piranha solution is a very strong oxidizing agent and extremely dangerous. Eye protection and gloves should be used during**

handling) for two minutes, then rinsed by a large amount of deionized water, followed by ethanol. The slides were, subsequently dried under nitrogen. For SAM formation, theAu slides were incubated according to the conditions specified earlier. After incubation, these SAM-coated gold slides were rinsed vigorously with ethanol and water and dried under nitrogen. The thickness was measured by a Gaertner L-117 Null ellipsometer.

4.4 Results

Ellipsometry Studies: Ellipsometry was used to determine the film thickness by measuring the change in light polarization upon reflection from the SAM-coated gold surface. The thickness determination requires knowledge of the refractive index of the SAM. As discussed previously,[56] a refractive index of 1.6 was used. Any difference between the actual refractive index of a PNA SAM and 1.6 will cause a systematic error in the calculated thickness value. The PNA SAM thicknesses, which have been obtained in this way, are reported in Table 4.2 and compared with the calculated lengths of the different PNA molecules. The length of the molecules have been estimated by adding characteristic lengths for the cysteine (4 Å), the ferrocene (5 Å), and each PNA base (3.5 Å or 3.4 Å).[57]

Table 4.2 (a) Ellipsometric Thickness, Calculated Length of Single-Stranded PNA Molecules:

oligomer	Ellipsometric thickness (nm)	Calculated length of molecule (nm)	oligomer	Ellipsometric thickness (nm)	Calculated length of molecule (nm)
Cys-T3-Fc	1.4 ± 0.1	1.95			
Cys-T4-Fc	1.4 ± 0.1	2.30	Cys-A4-Fc	1.6 ± 0.2	2.30
Cys-T5-Fc	1.3 ± 0.1	2.65			
Cys-T6-Fc	2.1 ± 0.1	3.00	Cys-A6-Fc	1.8 ± 0.1	3.00
Cys-T7-Fc	2.3 ± 0.1	3.35	Cys-A7-Fc	2.2 ± 0.2	3.35
Cys-T8-Fc	2.6 ± 0.1	3.70	Cys-A8-Fc	2.5 ± 0.1	3.70
Cys-T9-Fc	3.1 ± 0.1	4.05			
Cys-T10-Fc	3.0 ± 0.2	4.40	Cys-A10-Fc	3.2 ± 0.2	4.40

Table 4.2 (b) Ellipsometric Thickness, Calculated Length of Double-Stranded PNA Molecules:

molecule	Ellipsometric thickness (nm)	Calculated length of molecule (nm)
Duplex Cys-(A-T)7-Fc	2.5 ± 0.2	3.24
Duplex Cys-(A-T)8-Fc	3.2 ± 0.2	3.62
Duplex Cys-(A-T)9-Fc	3.5 ± 0.1	3.96
Duplex Cys-(A-T)10-Fc	3.6 ± 0.1	4.30
Duplex Cys-(A-T)15-Fc	5.1 ± 0.2	6.00

The ellipsometric thicknesses for the single-stranded SAMs were considerably less than the calculated length of the molecules. As described in our previous work,[56] this phenomenon seems to reflect a SAM with a certain percentage of molecules "lying-down" on the electrode surface and a second population of "standing-up" molecules. Based on this observation we previously proposed a model to calculate the percentage of

"lying-down" molecules using ellipsometric thickness values.[56] For Cys-T3-Fc to Cys-T7-Fc molecules the percentages are those reported earlier (ranging from 9% to 19% "lying-down" phase).[56] For the newer films studied here, the percentages of "lying-down" ss Cys-T8-Fc is 7.1±0.7%,Cys-T9-Fc is 5.1±0.5%, Cys-T10-Fc is 6.2±0.9%, Cys-A4-Fc is 12.9±3.6%,Cys-A6-Fc is 12.2±1.1%, Cys-A7-Fc is 9.2±1.8%, Cys-A8-Fc is 7.8±0.7% and Cys-A10-Fc is 5.4±1% respectively.

In the case of double-stranded PNA molecules, the thickness values were higher than the corresponding single-stranded molecule, which indicates that the ds PNA SAMs were more uniform and compact than ss SAMs. The difference between the measured thickness value and the calculated length of ds-PNA molecule could arise from the orientation of molecules at a certain tilt angle on the surface or from a mixture of "standing-up" and "lying-down" molecules. Although not conclusive, the electrochemistry results support the latter model. About 75% of the electrochemistry experiments of the double-stranded PNA SAM showed a small percentage (≤ 3%) of faster species (*vide supra*), whereas 25% did not show any evidence of faster species.

Electrochemical Characterization:

The voltammetry of freshly coated single-stranded PNA SAMs consisted of ferrocene with two different electron transfer rates. One species has a fast rate which has been attributed to molecules that are 'lying-down' on the gold surface, and occurs through space between the redox probe and the gold electrode. The second species has a slower charge transfer which has been attributed to the response of 'standing-up' molecules, so that charge transfer occurs through the PNA molecule; this feature of the SAMs was characterized and discussed at length in an earlier report.[56] To quantify the

slow rate constant species, the 'lying-down' molecules were electrochemically destroyed, using the protocol described previously.[56] In this method the ferrocenium of the 'lying-down' phase is preferentially reacted with Cl^-,[56,58] so that it becomes electrochemically silent. Subsequently, the charge transfer rates were measured for 'standing-up' molecules in a $NaClO_4$ solution for which the ferrocenium is stable (see reference 56 for details on this procedure).

In the case of the double-stranded PNA SAM, 75% of the voltammetry experiments showed the presence of a small percentage of molecules ($\leq$ 3%) which had a faster charge transfer rate and the other 25% of the electrode samples showed no clear evidence of a faster species. If the voltammetry experiment showed the presence of faster species, then this component was destroyed by using the same protocol that was developed for the single-stranded PNA SAMs. This protocol had little affected on the observed rate constant, presumably because the 'lying down' phase is a small percentage.

Possible sources of a faster species in the ds SAMs are a "lying-down" phase of the ds-PNA or contamination by ss-PNA that is "lying-down". The PNA duplex was formed by adding the complementary adenine (A) strand into a solution of ss-thymine (T)-PNA; the ferrocene redox probe is covalently attached to the ss-T-PNA. If the duplex formation with the complementary strand is less than 100%, then the sample will have both ds-PNA and a small amount of ss-T-PNA. Because the incubation temperature for ds-monolayer preparation was 27°C (higher temperatures could melt the duplexes), the single stranded ss-T-PNA contaminant could form a significant amount of "lying-down" phase.[56] Because the amount of 'lying-down' phase was typically not present or occurred in small amounts, no effort was made to distinguish between these two possibilities.

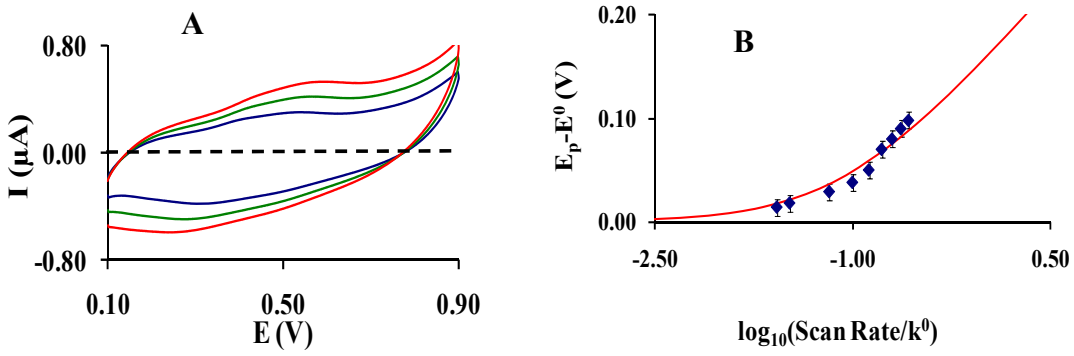

Figure 4.2 (A) Cyclic voltammograms are shown for duplex Cys-(A-T)7-Fc SAM at scan rates 20 mV/s (blue), 30 mV/s (green) and 40 mV/s (red). (B) A fitting curve is plotted for the determination of charge transfer rate of duplex Cys-(A-T)7-Fc SAM. The diamond symbols represent the experimentally determined points and the solid line represents the best fit theoretical curve. Error bars represent error in peak position determination

Electrochemical Results of Different PNA molecules:

Cyclic voltammetry was used to determine the charge transfer rate through duplex PNA molecules. If the charge transfer becomes slower than the voltammetric scan speed the voltammetric peak maxima start to shift. These voltammetric peak shifts can be fit by the Marcus theory[59,60] to determine the charge transfer rate constant. Representative electrochemical results for duplex Cys-(A-T)7-Fc are shown in Figure 4.2. Panel A shows three representative voltammograms collected at 20 mV/s, 30 mV/s and 40 mV/s. These voltammograms show that as the scan speed increases the voltammetric peak shifts, indicating that the charge transfer rate was slower than the scan speed of voltammetry. Figure 4.2B plots the dependence of the oxidation peak potential versus the scan speed and compares it to the prediction of the Marcus theory,[59,60] in which the standard electrocheical rate constant k^0 was used as an adjustable parameter. The ferrocene reorganization energy has been characterized by several research groups and

found to lie between 0.7 eV and 0.96 eV.[61,62] In this study, the ferrocene reorganization energy was taken as 0.8 eV.[63] A 25% change in reorganization energy does not change the quality of fitting. The voltammograms and fitting curves of other PNA SAMs are provided in the Supporting Information.

The following discussion is divided into three parts: Comparison of ss-T-PNA and ss-A-PNA SAMs; comparison of pure ds-(A-T)-PNA and mixed alkanethiol/ ds-(A-T)-PNA SAMs, and the comparison of ss-A-PNA, ss-T-PNA and ds-(A-T)-PNA SAMs respectively.

Table 4.3 Charge Transfer Rate for the "Standing-up" Population of ss-PNA SAMs

oligomer	k^0 (s^{-1})	oligomer	k^0 (s^{-1})
Cys-T3-Fc	2000 ± 200		
Cys-T4-Fc	200 ± 20	Cys-A4-Fc	275 ± 18
Cys-T5-Fc	3.0 ± 0.5		
Cys-T6-Fc	0.14 ± 0.03	Cys-A6-Fc	1.23 ± 0.12
Cys-T7-Fc	0.018 ± 0.002	Cys-A7-Fc	0.12 ± 0.03
Cys-T8-Fc	0.014 ± 0.004	Cys-A8-Fc	0.10 ± 0.01
Cys-T9-Fc	0.008 ± 0.002		
Cys-T10-Fc	0.007 ± 0.003	Cys-A10-Fc	0.037 ± 0.01

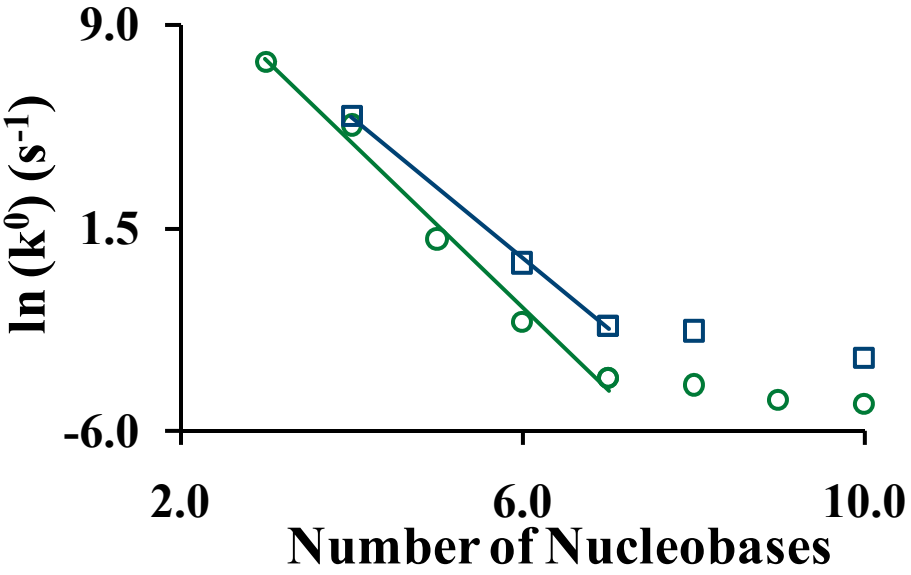

Figure 4.3 The charge-transfer rate constant k^0 of PNA molecules are plotted as a function of number of nucleobases between the gold electrode and ferrocene. Open circle green and blue symbols represent ss-T-PNA and ss-A-PNA respectively (error bars are smaller than symbols). The solid lines represent the best fit tunneling decay constant (β) for PNA molecules.

(a) *Comparison of ss-T-PNA and ss-A-PNA SAMs*: The charge transfer rate constants for ss-T-PNA and ss-A-PNA molecules are reported in Table 4.3, and the logarithm of the charge transfer rate constant is plotted versus the number of nucleobases in Figure 4.3 (open circle green is ss-T-PNA and open square blue is ss-A-PNA). Comparison of ss-T-PNA and ss-A-PNA charge transfer rates reveal that the k^0 of ss-A-PNA is consistently 7-9 time higher than ss-T-PNA when the number of nucleobases is ≥ 7. The solid lines in Figure 4.3 are best fits to a tunneling model for the shorter oligonucleotides, using a tunneling decay parameter of 0.86 $Å^{-1}$ that was previously determined for ss-T oligomers.[56] The rate constants for ss-A4, ss-A6 and ss-A7 imply a $\beta = 0.76 \pm 0.06$ $Å^{-1}$, it is clear that these data are consistent with 0.86 $Å^{-1}$ value as well. In this regime the charge transfer rate decreases exponentially as the number of nucleobases increases. For

nucleobase numbers ≥ 7 the slowing of the CT rate with distance is weak for both the Cys-(T)n-Fc and the Cys-(A)n-Fc. when the number of nucleobase ≥ 7.

(b) *Comparison of pure ds-(A-T) PNA monolayer and mixed alkanethiol/ ds-(A-T)-PNA SAM:* The rate constant k^0 for ds-(A-T)-PNA SAM has been measured in pure SAMs and in mixed n-octadecanethiol/ ds-(A-T)-PNA SAMs by voltammetry. Table 4.4 summarizes the data, and Figure 4.4 shows a logarithm plot of the rate constant versus the number of nucleobases pair. The black open triangle and open diamond points correspond to the experimental results for pure and mixed SAMs, respectively. The solid lines represent the best fit lines used for the determination of a tunneling decay length, β. The shortest duplex has 7 base pairs and the longest duplex has 15 base pairs. The results for both types of SAM show a similar CT rate and a weak decay of the rate constant with distance, 0.07 ± 0.03 $Å^{-1}$ for the pure monolayer and 0.23 ± 0.10 $Å^{-1}$ for the mixed monolayer. Although the mixed SAM has higher rate constant, the data show that both SAM types have charge transfer rates of similar magnitude. A fit of both data sets to a line gives a characteristic decay length of 0.17± 0.26 $Å^{-1}$.

Table 4.4 Charge Transfer Rate of ds-(A-T)-PNA SAM and mixed octadecanethiol/ds-(A-T)-PNA SAMs

Molecule	Pure SAM k^0 (s^{-1})	Pure SAM Coverage (pmol/cm^2)	Mixed SAM k^0 (s^{-1})
Duplex Cys-(A-T)7-Fc	0.25±0.05	109±38	0.80±0.15
Duplex Cys-(A-T)8-Fc	0.24±0.08	66±36	0.70±0.10
Duplex Cys-(A-T)9-Fc	0.14±0.07	90±23	0.21±0.04
Duplex Cys-(A-T)10-Fc	0.09±0.02	63±9	0.09±0.02
Duplex Cys-(A-T)15-Fc	0.038±0.005	87±30	

Because of low signal levels, it was not possible to determine k^0 for the 15 mer in the mixed SAM

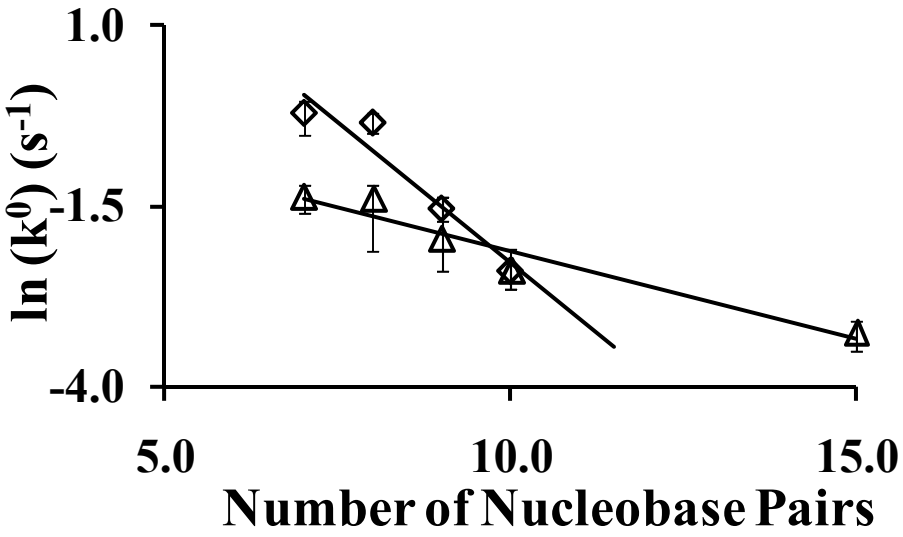

Figure 4.4 Charge-transfer rate of ds-(A-T)-PNA molecules are plotted as a function of the number of nucleobase pairs between a gold electrode and ferrocene. The open triangle black symbols represent the CT rate of pure monolayer and open diamond black symbols represent mixed octadecanethiol/ ds-(A-T)-PNA monolayer. The solid lines represent the best fit line used for the decay constant determination for PNA molecules

(c) *Comparison of ss-T-PNA, ss-A-PNA and ds-(A-T)-PNA results:* The charge transfer rate constants for three different types of pure SAMs (reported in Tables 4.3 & 4.4) are plotted together in Figure 4.5. In Figure 4.5, the green open circle, blue open square, black open triangle and black open diamond represent experimentally determined CT rates for ss-T-PNA, ss-A-PNA, ds-(A-T)-PNA and mixed ds-(A-T)-PNA SAM respectively. The solid lines are best fits to the rate constants for the case of $n \geq 7$. Comparison of ss-T-PNA and ds-(A-T)-PNA shows that the charge transfer rate of the duplex was consistently 14-15 times higher than the corresponding ss-T-PNA, and were two times higher than the ss-A-PNA where $n \geq 7$. For $n \geq 7$, a weak distance dependence is evident for all three different types of PNA oligomers. Comparison of these rate constant data with the short chain results suggests that the long distance charge transfer proceeds by a different mechanism.

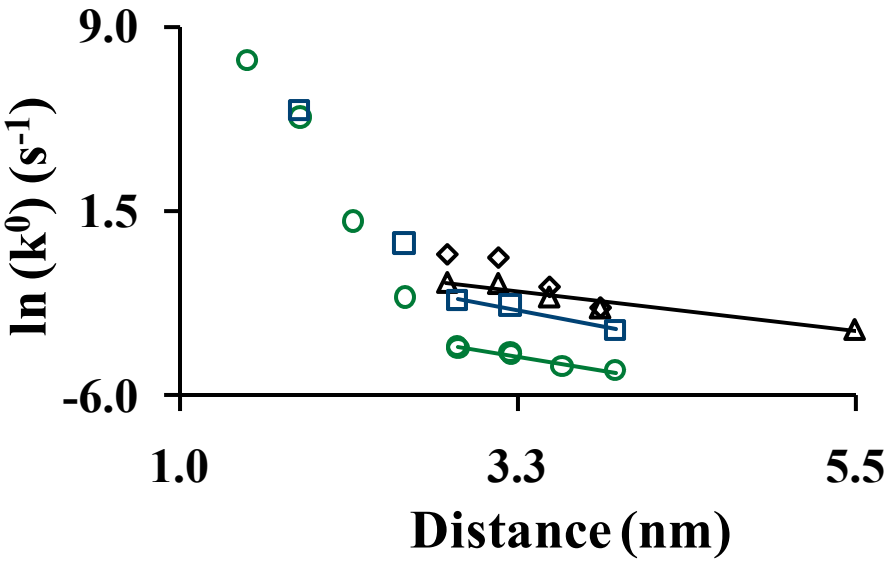

Figure 4.5 The charge-transfer rate of PNA molecules are plotted as a function of the distance between gold electrode and ferrocene. Green circle, blue square and black triangle symbols represent ss-T-PNA, ss-A-PNA and ds-(A-T) PNA respectively. Diamond black symbols represent the CT rate of mixed octadecanethiol/ ds-(A-T)-PNA monolayer. The solid lines represent the best fit line to the measured decay rates at long chain length; corresponding to $\beta = 0.10\pm0.13$ Å^{-1} for ss-T-PNA, $\beta = 0.12\pm0.14$ Å^{-1} for ss A-PNA, $\beta = 0.07\pm0.03$Å^{-1} for ds-(A-T)-PNA.

4.5 Discussion

The above results can be understood by considering two mechanisms for the electron transfer, namely a super-exchange mediated tunneling mechanism and a "hopping" mechanism. For short enough distance between the electrode and the ferrocene (<7 nucleotides), the charge transfer follows a coherent super-exchange mediated tunneling mechanism with a strong distance decay. At larger distances between the donor and acceptor(>7 nucleotides), the charge transfer rate follows an "incoherent hopping mechanism", in which charge briefly pauses on the nucleobases, giving rise to softer distance dependence. For all three different types of PNA molecules, the results show that for the number of nucleobases greater than or equal to 7, the charge transfer mechanism switches from tunneling to hopping. Can we understand the reason behind

this value for the mechanism switchover? In addition, the charge transfer rate of ss-T-PNA was consistently 7-8 times slower than ss-A-PNA when number of nucleobases were ≥ 7 and 14-15 times slower than ds-(A-T)-PNA. An explanation of the mechanism change should be able to account for this difference in the rate constants as well.

Tight-binding model:[3] Berlin et al. proposed a tight-binding model to determine the critical base number for switchover of the charge transfer mechanism from "super-exchange" to "hopping". We briefly describe this model and then apply it to the PNA results.

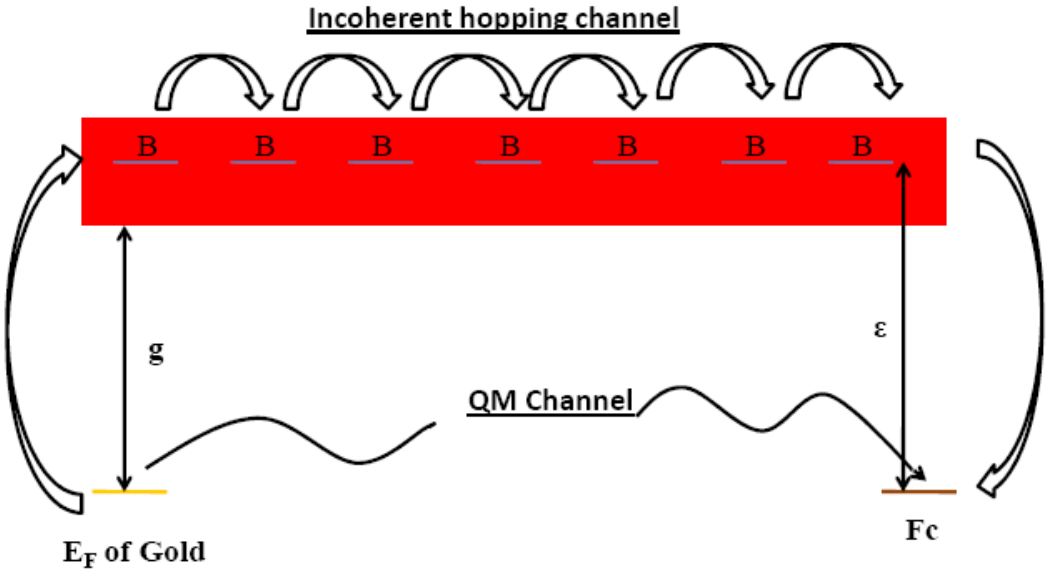

Figure 4.6 The diagram shows a band picture for stacks of Watson-Crick base pairs in PNA. The electronic coupling, b between base pairs leads to the formation of a tight-binding band that has a width of 4b. ε represents the energy gap between ferrocene and the base pair levels. g is the energy gap between the redox level and the bottom of the tight-binding conduction band. The energy level for the Fermi level of gold and ferrocene is taken to be the same. B represents the nucleobase and corresponds to A, T, or an A-T pair.

In this model, the incoherent hopping mechanism and the direct tunneling mechanism are assumed to operate simultaneously, hence $k_{total} = k_{tun} + k_{therm}$. At short

distance the quantum mechanical tunneling has the highest rate constant, so that $k_{tun} >> k_{therm}$ and $k_{total} \approx k_{tun}$. Because the tunneling decays strongly with distance, the contribution of k_{therm} to the overall rate constant becomes more important as the oligomer chain length increases. A mechanism switchover to a regime where the incoherent hopping mechanism dominates and the distance dependence is weak can be realized.

The electronic coupling between stacked base pairs leads to the formation of a tight-binding band. The energy (E) of the localized hole is given by Equation 4.1.

$$E = -((2b)^2 + \varepsilon^2)^{1/2} \tag{4.1}$$

where b is the coupling between bridge sites and ε is the difference in hole energy between the donor/acceptor and the bridge sites. The energy gap between the donor/ acceptor level and the tight-binding conduction band is g, given by

$$g = -2b + [(2b)^2 + \varepsilon^2]^{1/2} \tag{4.2}$$

When the charge transfer follows a tunneling mechanism, the tunneling rate (k_{tun}) can be written as

$$k_{tun} = \nu_{tun} \exp(-\beta L) \tag{4.3}$$

where ν_{tun} is the preexponential frequency factor for the tunneling mechanism, L is the length of the bridge (L = (n+1)a and a is the distance between the base pairs) and the tunneling decay parameter, β is given by Equation 4.4.

$$\beta = \frac{2}{a} \ln\left[1 + \frac{g}{2b} + \sqrt{\frac{g}{b} + \frac{g^2}{(2b)^2}}\right] \tag{4.4}$$

In the limit where the charge transfer follows a thermally activated hopping mechanism, the model assumes that it obeys an Arrhenius law, namely

$$k_{therm} = \nu_{therm} \exp(-g / k_B T) \tag{4.5}$$

where ν_{therm} is the preexponential frequency factor for the thermally activated release of a hole. In the case of very long oligomers, one must treat the diffusive motion of the hole along the chain. A one-dimensional random walk model for the diffusion gives a dependence on length of 1/L (see Eqn 14 of reference 3).

Comparison of equation 4.4 and 4.5 suggests the mechanism switchover from tunneling to hopping can be quantified by the condition $k_{tun} = k_{therm}$. Using this condition, one can calculate a critical length (n_{cr}) at which the "hopping" transport becomes important.

$$n_{cr} = [\frac{bx}{k_B T} - \frac{1}{2}\ln(\frac{\nu_{therm}}{\nu_{tun}})] \times \frac{1}{\ln[1 + x + (2x + x^2)^{1/2}]} - 1 \qquad (4.6)$$

where

$$x = \frac{g}{2b} \qquad (4.7)$$

In the approximation that $\nu_{therm} = \nu_{tun}$, equation 6 can be written as

$$n_{cr} \approx \frac{bx}{k_B T} \times \frac{1}{\ln[1 + x + (2x + x^2)^{1/2}]} - 1 \qquad (4.8)$$

Estimation of n_{cr} for PNA molecules:

The tight-binding model can be used to calculate n_{cr} for the three different types of PNA SAMs, if the parameters b and ε are known (g may be found via Eqn 4.2). For DNA, b values ranging from 0.1 eV to 0.4 eV have been reported.[5,64] Seidel et al.[65] have reported oxidation potentials for adenine and thymine. Assuming that the oxidation potentials found for adenine and thymine in DNA are the same in PNA, ε can be taken as 1.27 eV for A and 1.42 eV for T (see Figure 4.7). It seems plausible to assume that the charge in the ds-PNA hops through adenine rather than thymine, because the oxidation

potential of adenine is lower than that of thymine. Using Equation 4.8 and different b values, n_{cr} calculated for ss-T-PNA, ss-A-PNA and ds-(A-T)-PNA; see table 4.5

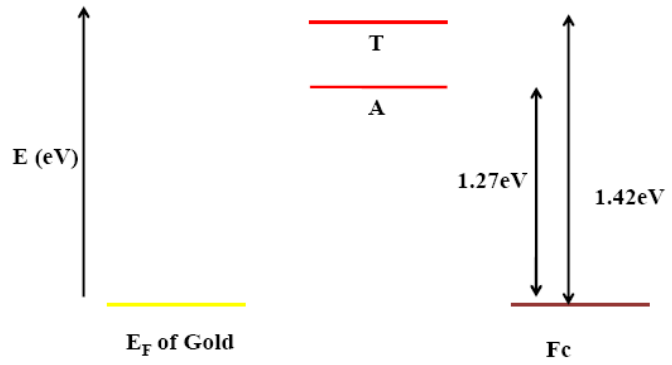

Figure 4.7 Oxidation Potential/ Tunneling barrier for Adenine and Thymine with respect to ferrocene.

Table 4.5 n_{cr} values for different b values for ss-A-PNA/ ds-(A-T)-PNA and ss-T-PNA

b (eV)	n_{cr} for ss-A-PNAds-(A-T)-PNA	n_{cr} for ss-T-PNA
0.1	7.3	8
0.16	8.2	9
0.2	8.7	9.5
0.3	9.5	10.5
0.4	10	11

According to the tight-binding model, n_{cr} values for ss-T-PNA range from 8 to 11 and for ss-A-PNA or ds-(A-T)-PNA range from 7.3 to 10, depending on the b value. Comparison to the experimental data should account for the cysteine between the PNA oligomer and the electrode. If the cysteine is considered to be equivalent to an extra nucleobase in the calculation, then the experimental n_{cr} for the ss-T-PNA and ss-A-PNA lies between 8 and 9. For the ds-(A-T) PNA the transition is not evident, however it is

clear that n_{cr} will be less than or equal to that found for the single strands. The tight binding model gives a range of n_{cr} values depending on the choice of b. Using a value of 0.16 eV for the electronic coupling between nucleobases (as reported earlier in 3, 66), the n_{cr} values are 8 to 9, in good agreement with the experiment.

Using b = 0.16 eV and equation 4.5, the rate constant for ds-(A-T)-PNA/ ss-A-PNA should be nearly 290 times higher than ss-T-PNA, because the difference in ε between A and T is 0.15 eV. The PNA SAMs showed a much weaker increase of the rate in ds-(A-T)-PNA/ss-(A)-PNA as compared to ss-T-PNA. The experimental change in the rate constant is consistent with a change in ε between A and T of 0.07-0.08 eV, about half the reported difference in oxidation potentials. This difference could arise from a difference in the oxidation potentials of A and T in DNA versus PNA, or from other environmental influences (e.g., from the metal surface) on the oxidation potential

Alternatively, it could be argued that the improvement of the rate constant in ss-A-PNA or ds-(A-T)-PNA is not so pronounced compared to ss-T-PNA because the different types of PNA molecules have different b values, i.e. electronic couplings. Comparing the CT rates of ss-T-PNA, ds-(A-T)-PNA, and ss-A-PNA, it is estimated that the g values are 0.05 eV and 0.07 eV lower in ss-A-PNA and ds-(A-T)-PNA respectively compared to ss-T-PNA. Using these values and ε in Figure 4.7, the b value for ss-A-PNA and ds-(A-T)-PNA need to be 0.11 eV and 0.12 eV, respectively (using b=0.16 eV value for ss-T-PNA).[3,66] From this calculation, n_{cr} for ss-A-PNA and ds-(A-T)-PNA will be 7.5 and 7.6 respectively which is in close agreement with experimental results.

Analysis of duplex pure (A-T) SAM results: The "hopping" mechanism is the basis of long range charge transfer and requires a large dynamic range in distance to properly

examine its accuracy. To this end a 15-mer of ds-(A-T)-PNA was synthesized and placed into the SAMs. One model for the "hopping" follows equation 4.9,[9,13,67] i.e.

$$k^0 = D \cdot \exp(-g/kT)/aL \qquad (4.9)$$

where D is the hole diffusion coefficient, a is the distance between the base pairs, L is the length of the bridge, and g is the bandgap for hole excitation. Figure 4.8, plots the charge transfer rate versus 1/L and a fit to the data by a straight line with a slope of 1.31 nm/s.

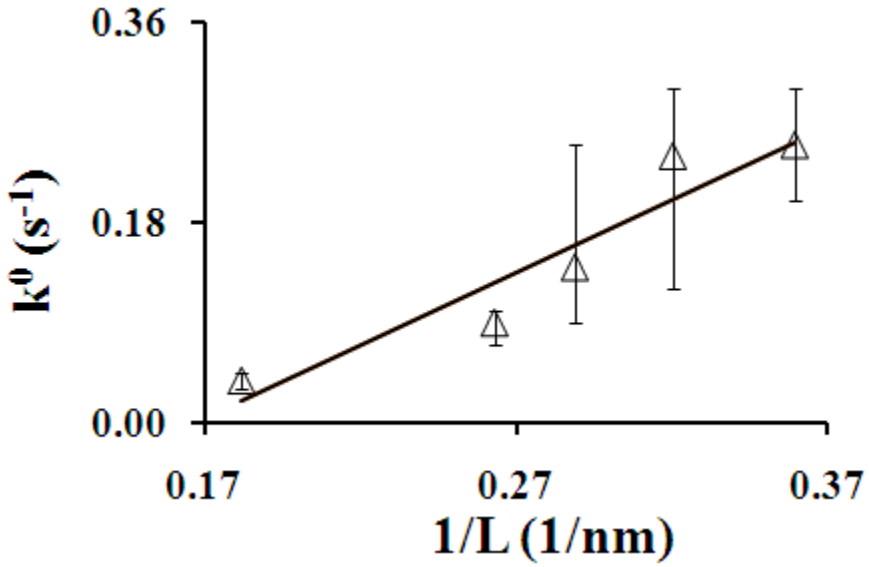

Figure 4.8 The charge transfer rate of duplex (A-T)-PNA molecules are plotted against 1/L. Black triangle symbols represent the experimentally determined results and the black solid line represents the best fit line for the determination of slope.

In order to estimate diffusion constant of hole (D) from the slope of figure 4.8 and equation 4.9, an estimation of g is necessary and its value is dependent on b value. From Equation 4.2, the g value is estimated to be 1.05 eV when b = 0.12 eV.[3] Then from equation 4.9, the diffusion constant (D) is estimated to be 2577 cm^2s^{-1}, using ε = 1.27 eV. This diffusion constant value found for PNA is larger than previously reported for DNA which was 6 x 10^{-3} cm^2s^{-1}.[5] Note that a change in the choice of g from 1.05 eV to 0.72 eV provides D= 6 x 10^{-3} cm^2s^{-1}. In order to provide a more rigorous test of the hopping

transport, it will be necessary to study different chain lengths in the hopping regime and to examine the temperature dependence of the rate constant.

4.6 Conclusions:

In this work ss-PNA and ds-PNA oligomers were self-assembled on a gold electrode. The SAM was characterized by cyclic voltammetry and ellipsometry. Electron transfer through these different types of PNA i.e. ss-T-PNA, ss-A-PNA and ds-(A-T)-PNA was studied. For short chains the distance dependence appears exponential, which indicates that charge transfer follows a super-exchange mediated tunneling mechanism, whereas for longer chains a weaker distance dependence was evident, suggesting that the charge transfer follows an incoherent hopping mechanism. For the shorter ss-T-PNA a tunneling decay constant (β) was reported to be 0.86±0.04 $Å^{-1}$.[56] In the case of ss-A-PNA, the decay constant (β) is found to be 0.76±0.06 $Å^{-1}$. For longer chains, the distance decay constant is very soft. The experimental transition point between these two (super-exchange and hopping mechanisms) could be rationalized by a tight-binding model[3] that was previously proposed for DNA. When charge transfer follows a hopping mechanism, it seems appropriate to treat the motion as diffusion of the charge carrier in the band. To obtain an accurate experimental assessment of that supposition requires a wider range of oligomer distances to be probed. For the more rigid duplex-(A-T)-PNA, the rate of longer PNA molecules was measured and compared to the prediction of a diffusion model, 1/L. While this range of distance remains limited for assessing the mechanism rigorously, these data support a hopping transport mechanism for the long range charge transfer in PNA, analogous to the case of DNA

The nature of the hopping mechanism remains under debate. Two different hopping models are discussed most often, i.e. "hole-resting site"[3,9,10,12,16,19,35] model and "polaron-like"[2,5,8,15-17] hopping model. According to the "hole-resting site" model the radical cation or hole is localized on individual bases and charge hops through individual bases to reach the final destination. In a "polaron like" hopping model structural distortion of the nucleic acid stabilizes and delocalizes the radical cation over several bases. Migration of charge occurs by thermal motions and the environment when bases are added or removed from the polaron. Importantly both mechanisms predict a weak distance dependence. The present study on PNA SAMs cannot distinguish between these two mechanisms.

The present studies on three different types of PNA molecules show several important observations and hence lead to several important conclusions. First of all it has been found that ss-T-PNA has the slowest rate among these three classes of PNA. The ss-A-PNA and ds-(A-T)-PNA rates were consistently 7-8 times and 14-15 times faster than that of ss-T-PNA. Second, these observations suggest that even in ss-PNA, nucleobases primarily determine the charge transfer rate and charge transfer occurs through nucleobases. The rates for ss-A-PNA are two times slower than that in ds-(A-T)-PNA, suggesting that the base pairing of duplex PNA makes charge transfer faster. This increase may reflect enhanced electronic coupling because of better nucleobase stacking of duplex PNA as compared to ss-PNA or hydrogen bonding in the duplex PNA. Lastly, the study of single-strand PNA and double-stranded PNA SAMs reveals that charge hopping is possible in thymine bases, as well as the widely appreciated hopping through adenine and guanine nucleobases.

4.7 Acknowledgements

We acknowledge support from the U.S National Science Foundation (CHE 0628169).

4.8 References and Notes:

(1) Arkin, M. R.; Stemp, E. D. A.; Holmlin, R. E.; Barton, J. K.; Hormann, A.; Olson, E. J. C.; Barbara, P. F. *Science* **1996**, *273*, 475-480.

(2) Barnett, R. N.; Cleveland, C. L.; Joy, A.; Landman, U.; Schuster, G. B. *Science* **2001**, *294*, 567-571.

(3) Berlin, Y. A.; Burin, A. L.; Ratner, M. A. *Chem. Phys.* **2002**, *275*, 61-74.

(4) Bernd Giese, S. W. *Angew. Chem.* **2000**, *39*, 3490-3491.

(5) Conwell, E. M.; Rakhmanova, S. V. *Proc. Natl. Acad. Sci.* **2000**, *97*, 4556-4560.

(6) Giese, B. *Annu. Rev. Biochem.* **2002**, *71*, 51-70.

(7) Giese, B.; Amaudrut, J.; Kohler, A.-K.; Spormann, M.; Wessely, S. *Nature* **2001**, *412*, 318-320.

(8) Henderson, P. T.; Jones, D.; Hampikian, G.; Kan, Y.; Schuster, G. B. *Proc. Natl. Acad. Sci.* **1999**, *96*, 8353-8358.

(9) Jortner, J.; Bixon, M.; Langenbacher, T.; Michel-Beyerle, M. E. *Proc. Natl. Acad. Sci.* **1998**, *95*, 12759.

(10) Jortner, J.; Bixon, M.; Voityuk, A. A.; Rosch, N. *J. Phys. Chem. A* **2002**, *106*, 7599-7606.

(11) Kelley, S. O.; Holmlin, R. E.; Stemp, E. D. A.; Barton, J. K. *J. Am. Chem. Soc.* **1997**, *119*, 9861-9870.

(12) Li, X. Q.; Zhang, H.; Yan, Y. *J. Phys. Chem. A* **2001**, *105*, 9563-9567.

(13) Meggers, E.; Michel-Beyerle, M. E.; Giese, B. *J. Am. Chem. Soc.* **1998**, *120*, 12950-12955.

(14) Murphy, C. J.; Arkin, M. R.; Jenkins, Y.; Ghatlia, N. D.; Bossmann, S. H.; Turro, N. J.; Barton, J. K. *Science* **1993**, *262*, 1025-1029.

(15) Rakhmanova, S. V.; Conwell, E. M. *J. Phys. Chem. B* **2001**, *105*, 2056-2061.

(16) Schuster, G. B. *Long-Range Charge Transfer in DNA;* Top. Curr. Chem. Vols 236 and 237; Springer: New York, 2004.

(17) Schuster, G. B. *Acc. Chem. Res.* **2000**, *33*, 253-260.

(18) Vicic, D. A.; Odom, D. T.; Nunez, M. E.; Gianolio, D. A.; McLaughlin, L. W.; Barton, J. K. *J. Am. Chem. Soc.* **2000**, *122*, 8603-8611.

(19) Berlin, Y. A.; Hutchison, G. R.; Rempala, P.; Ratner, M. A.; Michl, J. *J. Phys. Chem. A* **2003**, *107*, 3970-3980.

(20) Schwartz, D. K. *Annu. Rev. Phys. Chem.* **2001**, *52*, 107-137.

(21) Ulman, A. *Chem. Rev.* **1996**, *96*, 1533-1554.

(22) Jortner, J.; Ratner, M. A. *Molecular Electronics;* Blackwell: London. 1997.

(23) Degama, A. A. S. *Theor. Chim. Acta.* **1985**, *68*, 159.

(24) Evenson, J. W.; Karplus, M. *Science* **1993**, *262*, 1247-1249.

(25) Gehlen, J. N.; Daizadeh, I.; Stuchebrukhov, A. A.; Marcus, R. A. *Inorg. Chim. Acta.* **1996**, *243*, 271-282.

(26) Goldman, C. *Phys. Rev. A* **1991**, *43*, 4500.

(27) Harden, M. M. *J. Chem. Phys.* **1961**, *35*, 508-515.

(28) Joachim, C.; Ratner, M. A. *Nanotechnology* **2004**, *15*, 1065.

(29) Magoga, M.; Joachim, C. *Phys. Rev. B* **1997**, *56*, 4722.

(30) Priyadarshy, S.; Risser, S. M.; Beratan, D. N. *J. Phys. Chem.* **1996**, *100*, 17678-17682.

(31) Ratner, M. A. *J. Phys. Chem.* **1990**, *94*, 4877-4883.

(32) Reimers, J. R.; Hush, N. S. *J. Photochem. Photobiol. A* **1994**, *82*, 31-46.

(33) Remacle, F.; Levine, R. D. *J. Phys. Chem. B* **2001**, *105*, 2153-2162.

(34) Lewis, F. D.; Wu, T.; Liu, X.; Letsinger, R. L.; Greenfield, S. R.; Miller, S. E.; Wasielewski, M. R. *J. Am. Chem. Soc.* **2000**, *122*, 2889-2902.

(35) Bixon, M.; Giese, B.; Wessely, S.; Langenbacher, T.; Michel-Beyerle, M. E.; Jortner, J. *Proc. Natl. Acad. Sci.* **1999**, *96*, 11713-11716.

(36) Joy, A.; Ghosh, A. K.; Schuster, G. B. *J. Am. Chem. Soc.* **2006**, *128*, 5346-5347.

(37) Casero, E.; Darder, M.; Diaz, D. J.; Pariente, F.; Martin-Gago, J. A.; Abruna, H.; Lorenzo, E. *Langmuir* **2003**, *19*, 6230-6235.

(38) Herne, T. M.; Tarlov, M. J. *J. Am. Chem. Soc.* **1997**, *119*, 8916-8920.

(39) Zhang, R. Y.; Pang, D. W.; Zhang, Z. L.; Yan, J. W.; Yao, J. L.; Tian, Z. Q.; Mao, B. W.; Sun, S. G. *J. Phys. Chem. B* **2002**, *106*, 11233-11239.

(40) Egholm, M.; Buchardt, O.; Christensen, L.; Behrens, C.; Freier, S. M.; Driver, D. A.; Berg, R. H.; Kim, S. K.; Norden, B.; Nielsen, P. E. *Nature* **1993**, *365*, 566-568.

(41) Egholm, M.; Nielsen, P. E.; Buchardt, O.; Berg, R. H. *J. Am. Chem. Soc.* **1992**, *114*, 9677-9678.

(42) Petersson, B.; Nielsen, B. B.; Rasmussen, H.; Larsen, I. K.; Gajhede, M.; Nielsen, P. E.; Kastrup, J. S. *J. Am. Chem. Soc.* **2005**, *127*, 1424-1430.

(43) Rasmussen, H.; Kastrup, J. S.; Nielsen, J. N.; Nielsen, J. M.; Nielsen, P. E. *Nat. Struct. Biol.* **1997**, *4*, 98-101.

(44) Rasmussen, H.; Liljefors, T.; Petersson, B.; Nielsen, P. E.; Kastrup, J. S. *J. Biomol. Struct. Dyn.* **2004**, *21*, 495-502.

(45) Wittung, P.; Eriksson, M.; Lyng, R.; Nielsen, P. E.; Norden, B. *J. Am. Chem. Soc.* **1995**, *117*, 10167-10173.

(46) Franzini, R. M.; Watson, R. M.; Patra, G. K.; Breece, R. M.; Tierney, D. L.; Hendrich, M. P.; Achim, C. *Inorg. Chem.* **2006**, *45*, 9798-9811.

(47) Popescu, D. L.; Parolin, T. J.; Achim, C. *J. Am. Chem. Soc.* **2003**, *125*, 6354-6355.

(48) Watson, R. M.; Skorik, Y. A.; Patra, G. K.; Achim, C. *J. Am. Chem. Soc.* **2005**, *127*, 14628-14639.

(49) Azzam, R. M. A.; Bashara, N. M. *Ellipsometry and Polarized Light;* North- Holland publishing Co.: Amsterdam, 1977.

(50) Tompkins, H. G. *A User's Guide to Ellipsometry;* Academic Press Inc., MA, 1993.

(51) Anderson, G. W.; McGregor, A. C. *J. Am. Chem. Soc.* **1957**, *79*, 6180-6183.

(52) McKay, F. C.; Albertson, N. F. *J. Am. Chem. Soc.* **1957**, *79*, 4686-4690.

(53) Nielsen, P. E. *Peptide Nucleic Acids: Protocols and Applications,* Horizon Bioscience, UK, Wymondham, 2004.

(54) Sawyer, D. T.; Sobkowiak, A.; Roberts, J. L. *Experimental Electrochemistry for Chemists;* Wiley, NY, 1995.

(55) Lee, M. T.; Hsueh, C. C.; Freund, M. S.; Ferguson, G. S. *Langmuir* **2003**, *19*, 5246-5253.

(56) Paul, A.; Watson, R. M.; Lund, P.; Xing, Y.; Burke, K.; He, Y.; Borguet, E.; Achim, C.; Waldeck, D. H. *J. Phys. Chem. C* **2008**, *112*, 7233-7240.

(57) *The length of Cysteine, Ferrocene and each PNA base has been calculated by CAChe software. Geometry has been optimized by PM3 method.*

(58) Finklea, H. O. *In Electroanalytical Chemistry;* Bard, A. J., Rubinstein, I., Eds.; Marcel Dekker Inc.: New York, 1996, 19, 109.

(59) Marcus, R. A. *J. Chem. Phys.* **1956**, *24*, 966-978.

(60) Marcus, R. A. *J. Chem. Phys.* **1965**, *43*, 679-701.

(61) Chidsey, C. E. D. *Science* **1991**, *251*, 919-922.

(62) Smalley, J. F.; Feldberg, S. W.; Chidsey, C. E. D.; Linford, M. R.; Newton, M. D.; Liu, Y.-P. *J. Phys. Chem.* **1995**, *99*, 13141-13149.

(63) Napper, A. M.; Liu, H.; Waldeck, D. H. *J. Phys. Chem. B* **2001**, *105*, 7699-7707.

(64) Sugiyama, H.; Saito, I. *J. Am. Chem. Soc.* **1996**, *118*, 7063-7068.

(65) Seidel, C. A. M.; Schulz, A.; Sauer, M. H. M. *J. Phys. Chem.* **1996**, *100*, 5541-5553.

(66) Voityuk, A. A.; Rosch, N.; Bixon, M.; Jortner, J. *J. Phys. Chem. B* **2000**, *104*, 9740-9745.

(67) Giese, B.; Wessely, S.; Spormann, M.; Lindemann, U.; Meggers, E.; Michel-Beyerle, M. E. *Angew. Chem. Int. Ed.* **1999**, *38*, 996-998.

4.9 Supporting Information

Mixed Duplex PNA/n-Octadecanethiol Self-assembled Monolayer Preparation: The mixed duplex PNA/alkanethiol SAMs were prepared by a two-step process. Gold electrodes were covered by a submonolayer of duplex PNA, which was formed during overnight incubation (27°C) of the electrodes in the acetonitrile/water/ethanol (1: 1: 2) solution containing the desired PNA sequence at 5 μM concentration. To complete the monolayer with a octadecanethiol matrix, we adopted the method of the preparation of electrooxidation of alkylthiosulfates proposed by Lee et al.[55] Electrodeposition was performed in a three electrode system with the PNA-pre modified gold working electrode polarized with respect to a tungsten electrode. Platinum wire was taken as a counter electrode. The electrodes were immersed into 10 mM octadecylthiosulfate in tetrahydrofuran, in the presence of 100 mM tetrabutylammonium tetrafluoroborate as a supporting electrolyte. Electrodeposition was performed by applying multiple short potential pulses to the working electrode at +1.25 V (electrooxidation of the alkylthiosulfate) and -0.9 V (resting potential) vs tungsten. For example, in a single oxidative pulse, the potential was stepped from -0.90 to +1.20 V, held at +1.25 V for 5 s, and then stepped back to the -0.90 V resting potential for 5 seconds. The progress of the electrodeposition was periodically monitored (after each series of 50 potential pulses) by cycling the potential of the working electrode in the potential window of -0.9 to 1.25 V, and observing the height of the peak arising from the electrooxidation of octadecylthiosulfate. The decrease in the peak current suggests a decrease in the available area of the gold surface.[55] The electrodeposition was stopped when no peak was present or the height of the peak remained the same after three consequent series of 50 oxidative

potential pulses. Typically, the total process of electrodeposition required 8 to10 series of 50 oxidative potential pulses.

Table 4.6 Charge Transfer Rate and Surface Coverage for the "Standing-up" Population of ss-PNA SAMs

oligomer	k^0 (s^{-1})	coverage (pmol /cm^2)	no of trials	oligomer	k^0 (s^{-1})	coverage (pmol/ cm^2)	no of trials
Cys-T3-Fc	2000 ± 200	89 ± 8	5				
Cys-T4-Fc	200 ± 20	87 ± 7	9	Cys-A4-Fc	275	74 ± 4	6
Cys-T5-Fc	3.0 ± 0.5	47 ± 3	3				
Cys-T6-Fc	0.14 ± 0.03	140 ± 60	5	Cys-A6-Fc	1.23 ± 0.12	71 ± 10	4
Cys-T7-Fc	0.018 ± 0.002	80 ± 10	4	Cys-A7-Fc	0.12 ± 0.03	83 ± 11	5
Cys-T8-Fc	0.014 ± 0.004	80 ± 14	5	Cys-A8-Fc	0.10 ± 0.01	75 ± 11	4
Cys-T9-Fc	0.008 ± 0.002	95 ± 28	7				
Cys-T10-Fc	0.007 ± 0.003	87 ± 9	4	Cys-A10-Fc	0.037 ± 0.01	75 ± 9	3

Cyclic Voltammograms and Fitting Curves for Cys-T3-Fc, Cys-T4-Fc, Cys-T5-Fc, Cys-T6-Fc and Cys-T7-Fc are shown in Chapter 3 (Figure 3.9 to Figure 3.13)

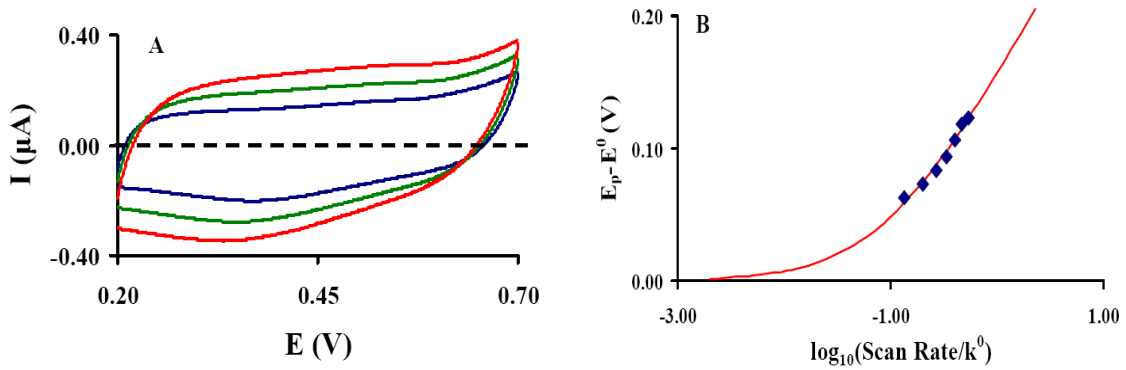

Figure 4.9 (A) Three cyclic voltammograms are shown for Cys-T8-Fc SAM at scan rates 4 mV/s (Blue), 6 mV/s (Green) and 8 mV/s (Red). (B) A fitting Curve is plotted for the determination of electron transfer rate of Cys-T8-Fc SAM.

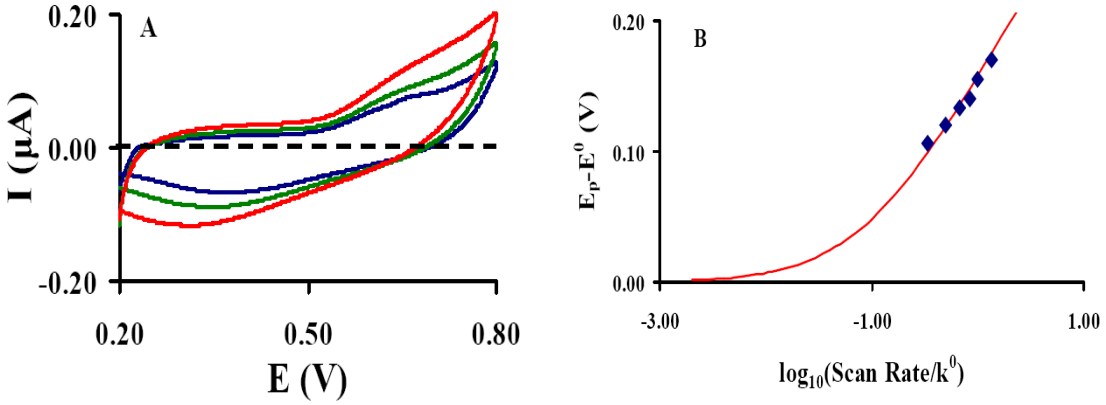

Figure 4.10 (A) Three cyclic voltammograms are shown for Cys-T9-Fc SAM at scan rates 2 mV/s (Blue), 4 mV/s (Green) and 6 mV/s (Red). (B) A fitting Curve is plotted for the determination of electron transfer rate of Cys-T9-Fc SAM.

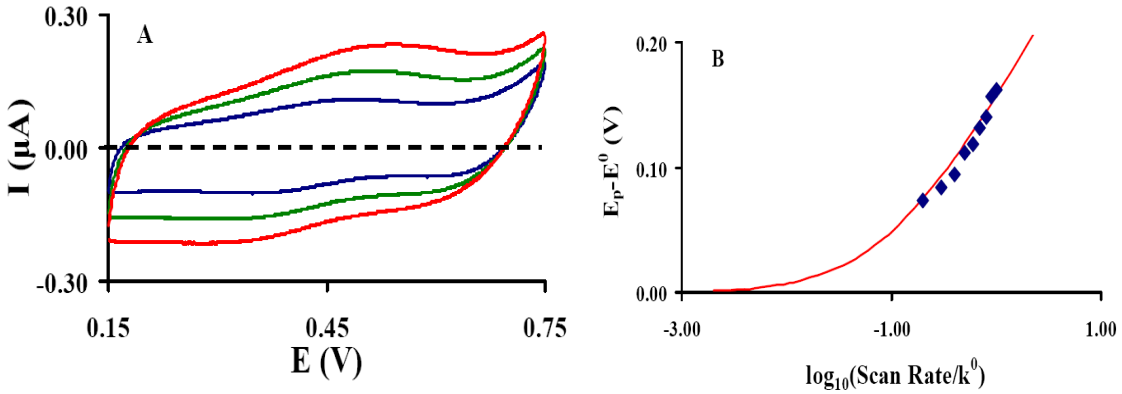

Figure 4.11 (A) Three cyclic voltammograms are shown for Cys-T10-Fc SAM at scan rates 2 mV/s (Blue), 4 mV/s (Green) and 6 mV/s (Red). (B) A fitting Curve is plotted for the determination of electron transfer rate of Cys-T10-Fc SAM.

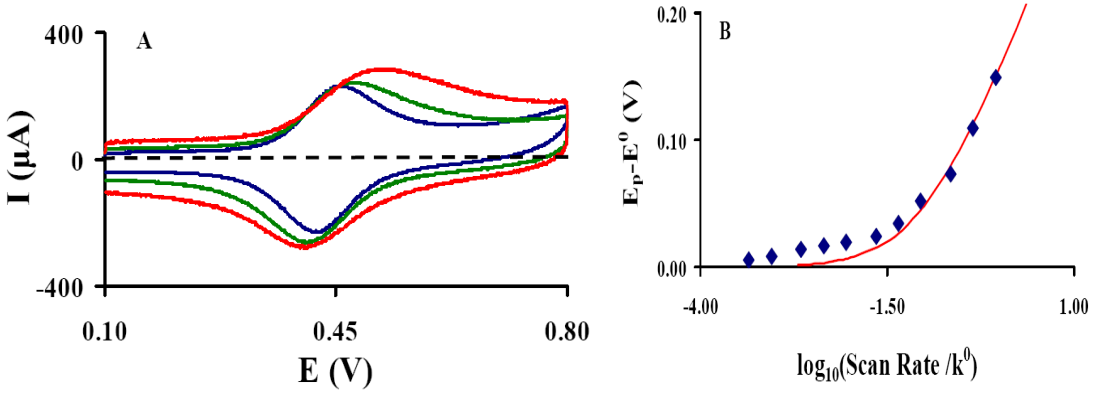

Figure 4.12 (A) Three cyclic voltammograms are shown for Cys-A4-Fc SAM at scan rates 1 V/s (Blue), 20 V/s (green) and 50 V/s (red). (B) A fitting curve is plotted for the determination of electron transfer rate of Cys-A4-Fc SAM.

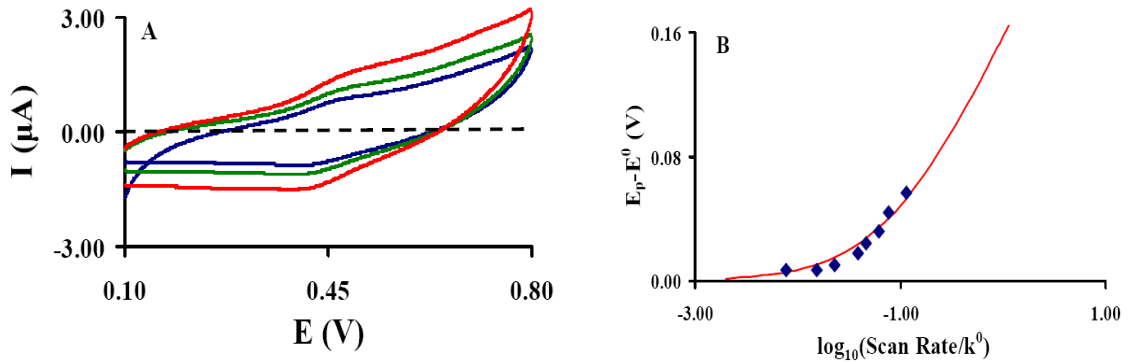

Figure 4.13 (A) Three cyclic voltammograms are shown for Cys-A6-Fc SAM at scan rates 20 mV/s (Blue), 30 mV/s (green) and 50 mV/s (red). (B) A fitting curve is plotted for the determination of electron transfer rate of Cys-A6-Fc SAM.

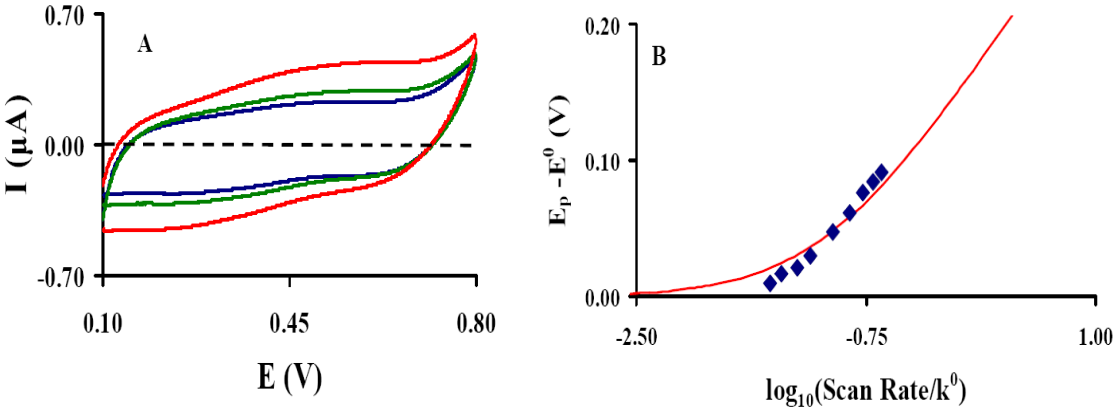

Figure 4.14 (A) Three cyclic voltammograms are shown for Cys-A7-Fc SAM at scan rates 8 mV/s (Blue), 10 mV/s (green) and 20 mV/s (red). (B) A fitting curve is plotted for the determination of electron transfer rate of Cys-A7-Fc SAM.

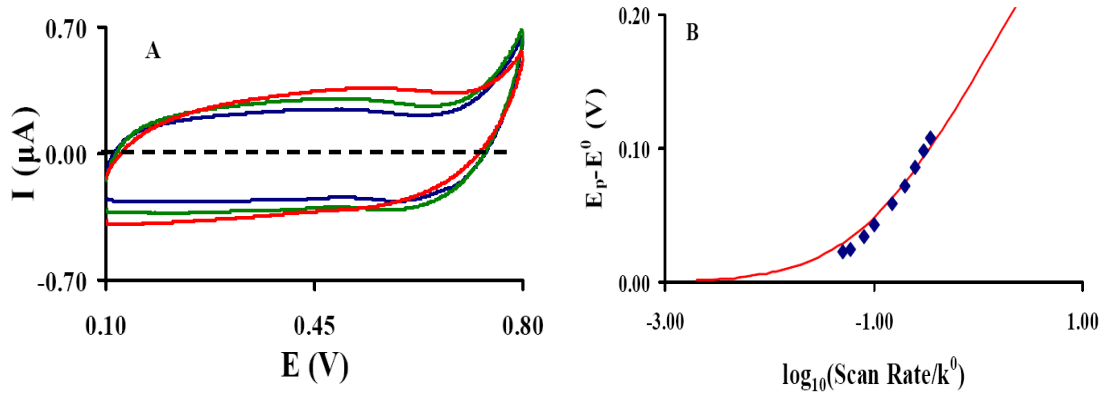

Figure 4.15 (A) Three cyclic voltammograms are shown for Cys-A8-Fc SAM at scan rates 8 mV/s (Blue), 10 mV/s (green) and 20 mV/s (red). (B) A fitting curve is plotted for the determination of electron transfer rate of Cys-A8-Fc SAM.

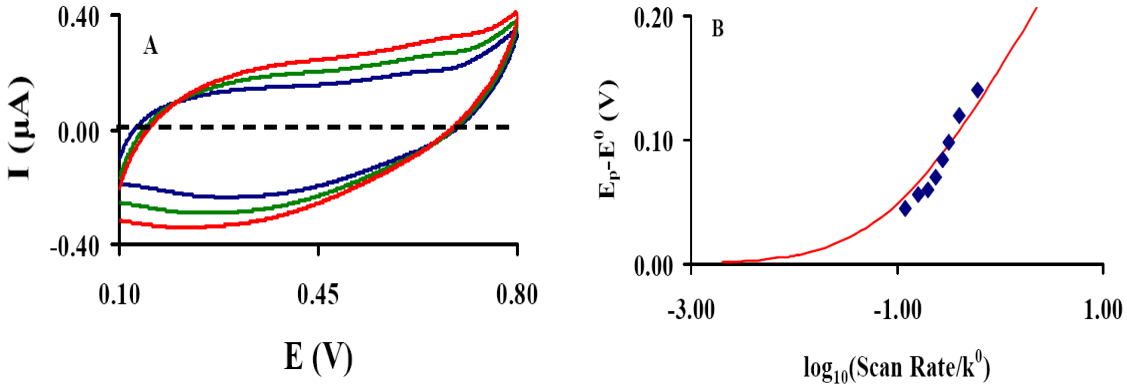

Figure 4.16 (A) Three cyclic voltammograms are shown for Cys-A10-Fc SAM at scan rates 8 mV/s (Blue), 10 mV/s (green) and 15 mV/s (red). (B) A fitting curve is plotted for the determination of electron transfer rate of Cys-A10-Fc SAM.

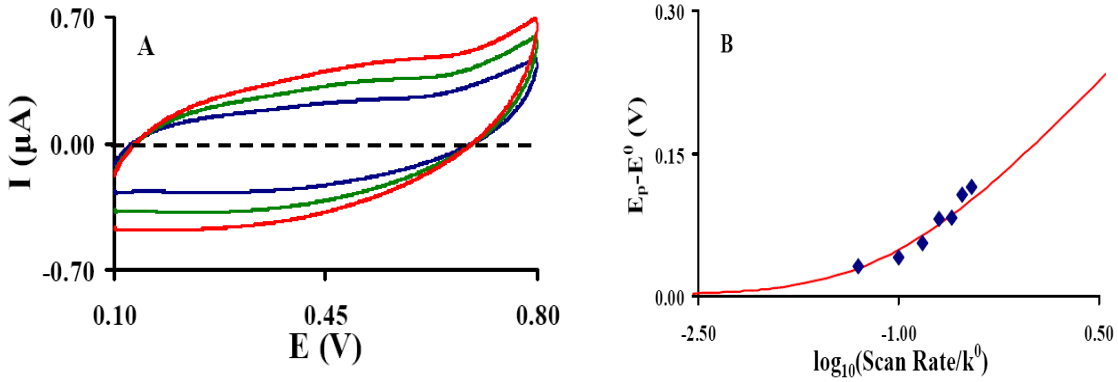

Figure 4.17 (A) Three cyclic voltammograms are shown for Duplex Cys-(A-T)8-Fc SAM at scan rates 20 mV/s (Blue), 30 mV/s (green) and 40 mV/s (red). (B) A fitting curve is plotted for the determination of electron transfer rate of Duplex Cys-(A-T)8-Fc SAM.

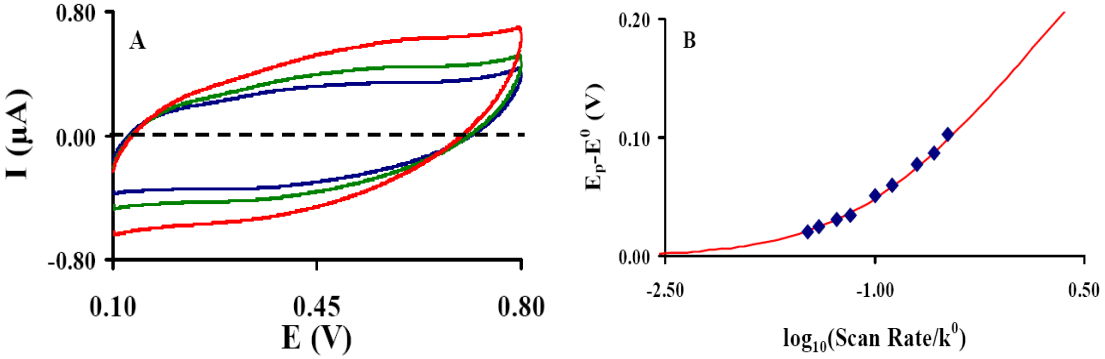

Figure 4.18 (A) Three cyclic voltammograms are shown for Duplex Cys-(A-T)9-Fc SAM at scan rates 15 mV/s (Blue), 20 mV/s (green) and 30 mV/s (red)) (B) A fitting curve is plotted for the determination of electron transfer rate of Duplex Cys-(A-T)9-Fc SAM

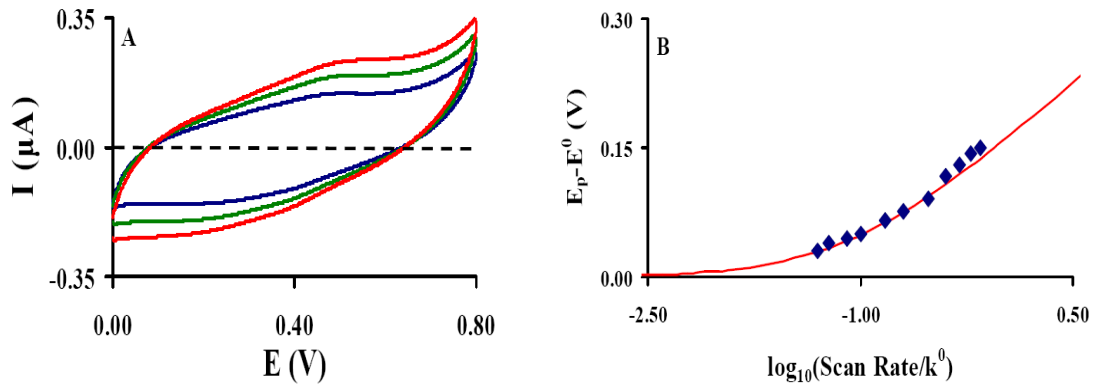

Figure 4.19 (A) Three cyclic voltammograms are shown for Duplex Cys-(A-T)10-Fc SAM at scan rates 10 mV/s (Blue), 15 mV/s (green) and 20 mV/s (red). (B) A fitting curve is plotted for the determination of electron transfer rate of Duplex Cys-(A-T)10-Fc SAM.

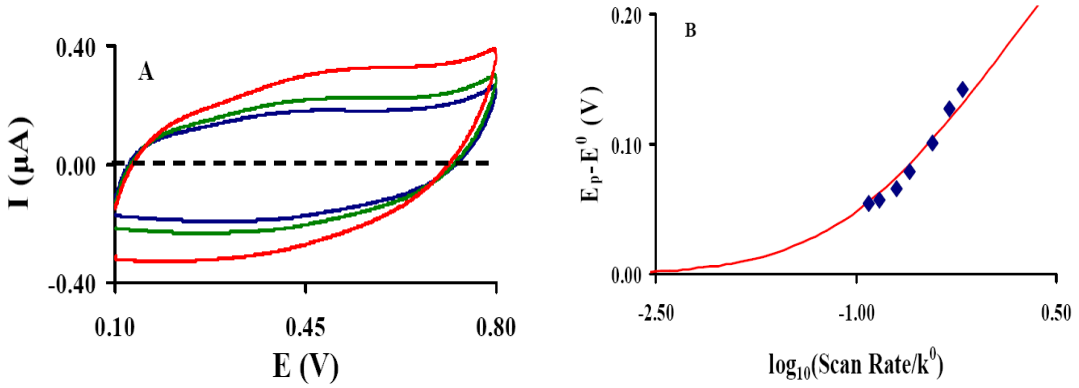

Figure 4.20 (A) Three cyclic voltammograms are shown for Duplex Cys-(A-T)15-Fc SAM at scan rates 8 mV/s (Blue), 10 mV/s (green) and 15 mV/s (red). (B) A fitting curve is plotted for the determination of electron transfer rate of Duplex Cys-(A-T)15-Fc SAM.

Chapter 5 Role of Nucleobases on the Charge Transfer of Peptide Nucleic Acid

Amit Paul,[a] Silvia Bezer,[#] Kathryn Davis,[a] Ravindra Venkatramani,[†] Richard M. Watson,[#] Alexander Balaeff,[†] Shahar Keinan,[†], David Beratan,[†*] Catalina Achim,[#*] David H. Waldeck[a*]

Department of Chemistry, University of Pittsburgh, Pittsburgh, PA, 15260,[a]

Department of Chemistry, Carnegie Mellon University, Pittsburgh, PA, 15213,[#]

Department of Chemistry, Duke University, Durham, NC, 27708[†]

5.1 Abstract

Self-assembled monolayers (SAMs) of single stranded (ss) and double stranded (ds) peptide nucleic acids (PNAs) containing seven nucleotides or seven base pairs were formed on gold electrodes. The dependence of the electron transfer rate constant on the nature of the central base or base pair (i.e., the fourth nucleotide was selected to be either cytosine (C), thymine (T), adenine (A), guanine (G) or a hydrogen (Bk) was investigated by using a ferrocene moiety at the N-terminus of the strand. The experiments show that the electron transfer rate constant through the oligonucleotide correlates with the oxidation potential of the nucleobase (or base pair) that is changed. Theoretical calculations of the electronic coupling through the relevant base stacks were performed and show a good correspondence with the observations. These data and calculations support the conclusion that the nucleobases (and base pairs) mediate the electron transfer in PNA, as with DNA.

5.2 Introduction

Self-assembled monolayers (SAMs)[1,2] of nucleic acids have been of great interest in the past decade, because of their potential applications in molecular electronics,[3] materials science,[4] molecular recognition,[5] biotechnology and biosensor development.[6-8] A mechanistic understanding of charge transfer (CT) through such SAMs is required for their potential application in molecular electronics. The past decade has seen progress in understanding the CT mechanism for deoxyribonucleic acid (DNA). For short DNA oligomers, it was found that charge transfer follows a one step superexchange mediated tunneling mechanism[9-19] and at large distance it follows a multi step hopping mechanism and charge can migrate more than 200 Å.[20-25] In duplex (ds) DNA, it has been claimed that guanine (G) and adenine (A) acts as hole resting sites,[25] *i.e.*, charge localizes on G or A, because their oxidation is lower than thymine (T) and cytosine (C).

Although, the CT mechanism through DNA has been well established in solution, only a few studies have addressed DNA SAMs, probably because of the difficulties in creating well-defined DNA assemblies on a metal surface.[26-28] This problem is particularly limiting for the case of single stranded (ss) DNA monolayer studies, which are even fewer than the number of ds DNA monolayer studies. Hartwich et al.[29] tried to determine the CT rate constant for mixed monolayers of a 12-mer single stranded DNA having a pyrrolo-quinoline-quinone redox probe attached to DNA through a spacer, and linked to an Au (111) surface through an ethane-thiol linker. The CT rate constant was too slow to be measured by cyclic voltammetry at a scan rate of >10 mV s^{-1}. Chahma et al.[30] reported a CT rate constant of 12 s^{-1} for a 20 base ss DNA monolayer, which was only 10 times slower than the corresponding ds monolayer. By contrast, Anne et al.[31]

reported a charge transfer rate of 4 x 10^4 s^{-1} for a 20 mer ss thymine containing DNA monolayer and attributed this fast transfer rate constant to the fact that ss DNA lies flat on the electrode; so that CT occurs through space to redox groups near the electrode surface. The limited success of earlier workers and the challenge of making compact films with charged DNA oligomers has motivated us to seek an alternative to DNA that preserves the nucleobase properties.

In contrast to the negatively-charged and chiral backbone of DNA, peptide nucleic acid (PNA) has a neutral and achiral backbone based on aminoethylglycine (Figure 5.1 (a) and (c)).[32,33] The neutral backbone of PNA makes it a good candidate for self-assembly. PNA forms duplexes with itself and also with DNA by Watson-Crick base pairing. The PNA·PNA duplexes adopt a helical structure termed P-type, which has a large pitch with 18 bases/turn, diameter of 28 Å, and 3.2-3.4 Å rise/base pair.[34-36] Although the backbone of PNA is achiral, chirality can be induced by introducing a chiral amino acid in PNA.[37]

Recently we reported a charge transfer study of short chain thymine (T) containing ss PNA molecules, where the number of T residues was varied.[38] The charge transfer mechanism was found to be described well by a superexchange mediated tunneling mechanism, where the decay constant (β) was 0.86 $Å^{-1}$. This decay constant is similar to that for alkanethiol[39-43] and peptides.[44,45] That study poses an important question, "Is the charge transfer in PNA controlled by the nucleobase or the peptide backbone?"

In this work, five different 7-mer ss PNA and four different ds-PNA molecules were studied (Figures 5.1(a) and (c)). PNA with a ferrocene redox probe covalently attached at its N-terminus was immobilized on a gold surface through a cysteine group at

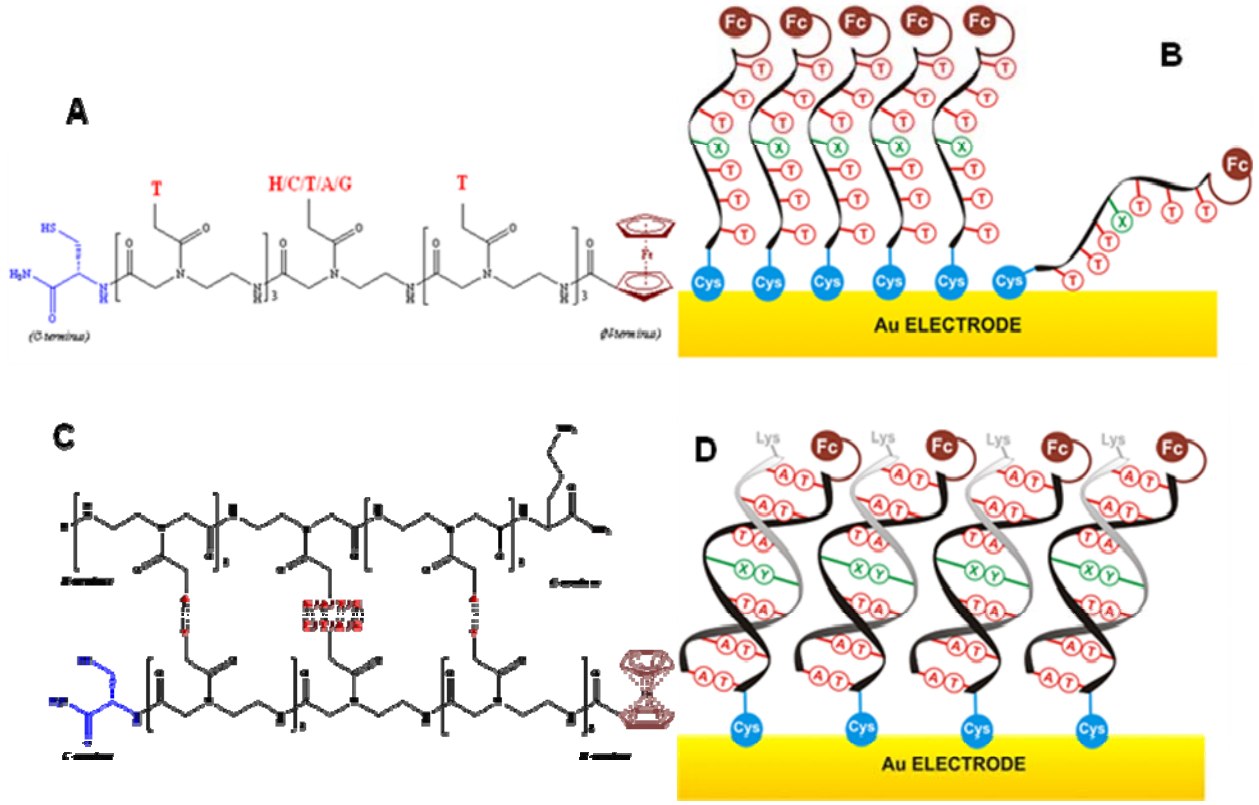

Figure 5.1 (A) Chemical structure of ss PNA that has a C-terminus cysteine and an N-terminus ferrocene. (B) Panel B shows a schematic representation of ss PNA molecules self-assembled on a gold surface, in which the blue circle represents cysteine, the black curl represents backbone of PNA, the nucleobases are represented in open circles (Fourth residue is represented as X where X is (H(Bk)/C/T/A/G) and the brown circle represents ferrocene. (C) Chemical structure of ds PNA that has a C-terminus cysteine and an N-terminus ferrocene. (D) Panel D shows a schematic representation of ds PNA molecules self-assembled on a gold surface, in which the blue circle represents cysteine, the black curl represents backbone of PNA, the nucleobases are represented in open circles (Fourth base pair is represented as X and Y where X and Y pairs are (T-A, A-T, C-G, G-C)) and the brown circle represents ferrocene.

its C-terminus (Figure 5.1(b) and (d)). In the case of ss-PNA molecules the first and end three residues were kept as thymine (T) nucleobases and the fourth middle residue was varied, i.e. guanine (G), adenine (A), cytosine (C), thymine (T), or hydrogen (Bk). For ds-PNA, the first and end three base pairs were thymine-adenine (T-A) and fourth base pairs were T-A, A-T, C-G and G-C respectively. Cyclic voltammetry was used to determine the CT rate constant through SAMs of these PNA molecules and probe the role

of the nucleobase on the charge transfer. The study demonstrates that the CT rate in PNA SAMs can vary by more than a hundred-fold with a change in the fourth (middle) residue, which indicates that charge transfer in PNA is primarily controlled by nucleobases.

Theoretical transport calculations, using the non-equilibrium Green's function method on optimized structures of seven base pair single stranded PNA fragments, were performed on each of the four T3-X-T3 fragments investigated experimentally. The results show that the purine substituted (X=G,A) systems are significantly more conductive than the pyrimidine substituted (X=C,T) systems in agreement with the experimental trend. The trend within the purines also agrees with the experimental trends however the trend within the pyrimidines is reversed (X=C is seen to be more conductive than X=T). However since the difference in experimental charge transfer rates falls within the errors bars for X=C,T this is not taken as a major deviation from the experimental trend. Another trend in the results that agrees with experiments is that the conductivity of purine substituted systems is more well resolved (further apart) than that of the pyrimidines substituted systems. A linear relationship is obtained between calculated (near zero bias) conductance and experimental charge transfer rates. To summarize, the calculations affirm that charge transport through the nucleobases can explain the observed differences in charge transfer rate constants for the four single stranded PNA (T3-X-T3 ; X=G,A,C,T) SAMs.

5.3 Experimental Details

PNA synthesis: PNA oligomers were synthesized by solid phase peptide synthesis using the Boc protection strategy.[46-48] MBHA resin (Peptides International, Louisville, KY) with a loading of 0.18 mEquiv/g was down-loaded (see reference 48 for more detail

about this procedure) using Boc-L-Cys-(4-MeOBzl)-OH (NovaBiochem/Merck Biosciences, Switzerland) to an estimated loading of 0.04-0.06 mEquiv/g. Thereafter three Boc-T-OH PNA monomers (Applied Biosystems, Foster City, CA) were coupled using 1H-Benzotriazolium 1-[*bis*(dimethylamino) methylene]-5chloro-hexafluorophosphate (1),3-oxide (HCTU) (Peptides International) as a coupling agent. After that one Boc-(A-Z)-OH/ Boc-(G-Z)-OH/ Boc-(C-Z)-OH/ Boc-T-OH or Boc-Backbone-OH monomer was coupled depending on the sequence. Subsequently, three more Boc-T-OH monomers were coupled. Finally, ferrocenecarboxylic acid (Aldrich) was coupled to the N-terminus, repeated twice to increase the yield of ferrocene-conjugated PNA. The complementary strand for duplex PNA molecules has been synthesized by down-loading MBHA resin with Boc-L-Lys-(4-MeOBzl)-OH. Thereafter three Boc-(A-Z)-OH was coupled. After that one Boc-(A-Z)-OH/ Boc-(G-Z)-OH/ Boc-(C-Z)-OH/ Boc-T-OH monomer was coupled depending on the sequence. Then three more Boc-(A-Z)-OH monomers were coupled. Oligomers were cleaved from the resin using trifluoroacetic acid (TFA) and trifluoromethanesulfonic acid (TFMSA), precipitated in ethyl ether, and dried under nitrogen. The solid products were dissolved in 15% acetonitrile aqueous solution and purified by reverse-phase HPLC using a solvent gradient, from 15% to 35% acetonitrile in water over 40 minutes on a Waters Delta 600 pump with a 2996 photodiode array detector (Milford, MA). PNA oligomers were characterized by MALDI-TOF mass spectrometry on an Applied Biosystems Voyager-DE STR Workstation.

PNA solutions were prepared in deionized water and the PNA concentrations were determined by UV-Vis spectrophotometry assuming ε_{260} = 8600, 6600, 13700, and 11700

cm^{-1} M^{-1} for each T, C, A, and G-monomer respectively.[48] PNA solutions for electrode incubation were typically 20 μM ssPNA in 10 mM pH 7.0 sodium phosphate buffer solution that was a 50% acetonitrile/50% water mixture. Double stranded PNA samples were prepared by mixing a 20 μM solution of two strands, then heating at 95ºC and after that slowly cooling down to room temperature.

Electrode Preparation: A gold wire (0.5 mm diameter, 99.999%, Alfa Aesar, MA) was cleaned by reflux in nitric acid (70%) at 130°C for two hours and then washed with deionized water (>18 MΩ. cm). The wire was sealed in a soft-glass capillary tube with the tip exposed. The tip of the gold wire was heated to form a ball. The gold ball was reheated in a flame until glowing, then slowly cooled down and finally quenched in deionized water. This annealing process was repeated more than fifteen times until a smooth ball electrode was obtained. The area of the electrode was determined electrochemically[49] and found to be typically ~0.1 cm^2.

Self Assembled Monolayer (SAM) Preparation: Self-assembled monolayers for ss-PNA were prepared by incubating gold ball electrodes in 1 mL of a 20 μM PNA solution for 28 hours at 40°C. After incubation the gold electrodes were washed with nanopure water and directly used in the electrochemical studies. SAMs of ds-PNA were prepared by incubating gold ball electrodes in 1 mL of a 20 μM ds PNA solution for 28 hours at 27°C.

Electrochemical Measurements: Cyclic voltammetry was carried out on a CH Instrument Electrochemical Analyzer 618B (Austin, TX). The three-electrode electrochemical cell consisted of an Ag/AgCl (3 M KCl) reference electrode, a platinum wire as counter electrode, and a SAM-coated gold ball electrode as the working electrode. All experiments were performed in 1 M $NaClO_4$ (pH=7-8) aqueous electrolyte solution at

room temperature. The uncompensated solution resistance was measured by AC impedance and found to be less than 5 Ω, so that the iR drop was not important for these measurements. The coverage of the PNA-ferrocene SAM was calculated by integrating the charge under the voltammetric peaks.

Ellipsometry: Ellipsometry[50,51] was used to measure film thicknesses. The molecules were self-assembled to form a monolayer thick film on evaporated gold slides (EMF Corp, Ithaca, NY). The Au slides were 0.7 inch x 0.3 inch x 0.062 inches in size and consisted of about 100 nm Au over a 50 nm thick Ti binder layer on float glass. The gold slides were cleaned by immersion in "piranha" solution (1:3 H_2O_2 and 98% H_2SO_4) **(Caution! The piranha solution is a very strong oxidizing agent and extremely dangerous. Eye protection and gloves should be used during handling)** for two minutes, then rinsed by a large amount of deionized water, followed by ethanol. They were, subsequently dried under nitrogen. For ss-PNA SAM formation, the Au slides were incubated in 1.0 mL of a 20 μM ss PNA solution for 28 hours at 40°C and in the case of ds-PNA, the slides were incubated in 1.0 mL of a 20 μM ds PNA solution for 28 hours at 27°C. After incubation, these SAM-coated gold slides were rinsed vigorously with ethanol and water and dried under nitrogen. The thickness was measured by a Gaertner L-117 Null ellipsometer.

Computational Details:

Molecular dynamics simulations: Structures for the four single stranded PNA sequences T3-X-T3 (X=G,A,C,T) used in the experiments were constructed by extracting one of the strands from a double stranded fragment studied earlier[52]. Each structure was equilibrated using standard MD protocols and 500 structures extracted for each system for further

analysis. During the equilibration and production runs two atoms (C and N) which tether each nucleobase to the backbone were constrained. This procedure allowed the nucleobases to move while keeping the backbone fixed.

Electronic structure calculations: For each MD snapshot structure, the atomic coordinates of the three central bases (T-X-T) were extracted, and the dangling bonds were capped with hydrogens using VMD. Because it contains the differences in both energies and nearest neighbor couplings, this core segment is expected to capture the differences in charge transfer rates between the four T3-X-T3 systems. Higher order couplings are at least an order of magnitude smaller than nearest neighbor couplings[53,54]; hence, the differences induced in them by changing X are neglected. Using single point self-consistent field calculations the electronic structure of this core segment was calculated with the INDO/s method implemented in the CNDO program. The semiempirical INDO/s approach provides a useful balance between cost and performance, especially for electronic structures with a strong propensity for CT. This approach has been used widely to compute donor-acceptor couplings in DNA. The calculated molecular orbitals and energies were used as input for the NEGF method to calculate transport properties.

NEGF method: The NEGF formalism[55] allows one to calculate transport properties for a molecular device contacted on either side by metal reservoirs. The transmission coefficient is determined by summing over all possible pathways for charge transfer at energy E from one electrode to the other through the molecule: $T(E) = Tr[\mathbf{\Gamma_L G \Gamma_R G}^{+}]$. The broadening matrix: $\Gamma = i\,[\Sigma - \Sigma^{+}]$ is the imaginary part of the self-energy Σ. The key quantity here is the molecular Green's function G and is given by

$$G(E) = \frac{1}{(E\mathbf{I} - \mathbf{H} - \mathbf{\Sigma_L} - \mathbf{\Sigma_R})} \tag{5.1}$$

In equation 5.1, H is the Fock matrix from the INDO/s calculations. We assume that the core T-X-T is coupled to the contacts only through the carbon and nitrogen atoms of the T nucleobase rings and that the couplings between atomic orbitals are not affected by the contacts. Thus, the broadening matrix is: $\Gamma_{ii} = 0.1$ eV for all thymine; $\Gamma_{ii} = 0$ for all other i; and $\Gamma_{ij} = 0$ for $i \neq j$.

Here i and j are atomic orbital indices in the basis. We neglect the real part of the self-energy matrices and define it as purely imaginary. The effect of the peripheral thymine bases and linkers are included via the effective coupling represented by the broadening matrix. The magnitudes of the terms in the broadening matrix were deliberately chosen to be small (relative to diagonal terms of the Fock matrix) so that the contacts do not strongly perturb the molecular eigenstates. This choice allows any correlation of the calculated conductance values with experimentally determined charge transfer rate constants to become manifest. Using the expression for transmission and assuming a fixed value for the metal Fermi energy for all systems (T3-X-T3), the current for a small applied potential bias (100 mV) was calculated. The Fermi level was far enough from the molecular orbital energies (MOs), over the range of applied bias, that the current-voltage curves were linear and the conductance for each snapshot structure was computed.

The transmission coefficient (and the current) may be represented in the basis of molecular eigenstates, hence dissecting the transmission (or current) into contributions from each molecular orbital. In order to identify the MOs with the greatest contribution to the current (channels with the least resistance), the contribution of each orbital i was assigned a scoring factor:

$$SF_i = \sum_j \Gamma_{ij}^L G_{jj} \Gamma_{ji}^R G_{ii} \quad (5.2)$$

where the index j runs over all the MOs. When i=j the product represents a pure contribution from oribital i with broadening terms Γ_{ij}^L and Γ_{ji}^R When i≠j the product represents a contribution due to the coupling of orbital i with orbital j. Each term in the sum can be positive or negative depending on the sign of the coupling elements of Γ_{ij}^L and Γ_{ij}^R.

5.4 Results

Ellipsometry Studies: Ellipsometry was used to determine the film thickness by measuring the change in light polarization upon reflection from the SAM-coated gold surface. The thickness determination requires knowledge of the refractive index of the SAM. As discussed previously,[38] we used a refractive index of 1.6. Any difference between the actual refractive index of a PNA SAM and 1.6 will cause a systematic error in the calculated thickness value. The PNA SAM thicknesses, which have been obtained in this way, are reported in Table 5.1. The length of the ss PNA and ds PNA molecules are estimated to be 3.35 nm and 3.28 nm respectively, which is determined by adding characteristic lengths for the cysteine (4 Å), the ferrocene (5 Å), and each PNA base (3.5 Å or 3.4 Å).[56]

Table 5.1 Ellipsometric thickness of ss-PNA and ds-PNA SAMs:

Molecule	Thickness (nm)	Molecule	Thickness (nm)
Cys-T3-Bk-T3-Fc	2.2 ± 0.2		
Cys-T3-C-T3-Fc	2.3 ± 0.1	Cys-T3-T-T3-Fc A3-A-A3-Lys	2.5 ± 0.2
Cys-T3-T-T3-Fc	2.3 ± 0.1	Cys-T3-A-T3-Fc A3-T-A3-Lys	2.8 ± 0.6
Cys-T3-A-T3-Fc	2.5 ± 0.1	Cys-T3-C-T3-Fc A3-G-A3-Lys	3.4 ± 0.2
Cys-T3-G-T3-Fc	2.4 ± 0.1	Cys-T3-G-T3-Fc A3-C-A3-Lys	3.5 ± 0.2

The ellipsometric thicknesses for the ss PNA SAMs were less than the calculated length of the molecules, i.e. 3.35 nm. As described in our previous work,[38] this phenomenon seems to reflect a SAM with a certain percentage of molecules lying flat on a gold surface and a second population of standing up molecules. A comparison of the measured SAM thickness to the 3.35 nm molecular length implies that ~ 7-9.5 % of the molecules are 'lying-down'.

In the case of double-stranded PNA molecules, the thickness values were higher than the single-stranded molecule, which indicates that the ds SAMs were more uniform and compact than ss SAMs. The difference between the measured thickness value and the calculated length of ds-PNA molecule could arise from molecules at a certain tilt angle on the surface or from a mixture of "standing-up" and "lying-down" molecules. About 25% of the electrochemistry experiments of the double-stranded PNA SAMs did not show any evidence of a faster species, whereas the rest experiments showed a very small percentage (≤ 3%) of faster species (*vide supra*).

Electrochemical Characterization: For each type of ss PNA SAM the voltammetry indicates the presence of two different redox species. One species had a fast CT rate

which is presumably caused by molecules that were 'lying-down' on the gold surface, so that direct CT from the ferrocene/ ferrocenium to the gold electrode is rapid. The second species had a much slower CT which presumably is the response of 'standing-up' molecules, where CT occurs through the PNA molecules; as reported earlier.[38] For each of the ss PNA SAMs the percentage of 'lying-down' molecules was found to be 8-10% of the total coverage. To quantify the slow rate constant species, the 'lying-down' molecules were electrochemically destroyed, using the protocol described previously.[38] In this method the ferrocenium of the 'lying-down' phase is preferentially reacted with Cl^-, so that it becomes electrochemically silent. Subsequently, the CT rates were measured for 'standing-up' molecules. (see reference 38 for detail on this procedure).

In the case of double-stranded PNA SAM, 75% of the voltammetry experiments showed the presence of a small percentage of molecules ($\leq$ 3%) which had a faster CT rate and the other 25% of the electrode sample showed no clear evidence of faster species. If the voltammetry experiment showed the presence of faster species, then it was destroyed by using the same protocol that was developed for the single-stranded PNA SAMs.

The PNA duplex was formed by adding the complementary single strand into ss-PNA in which the ferrocene redox probe and the cysteine are covalently attached. If the duplex formation with the complementary strand is less than 100%, then the sample will have both ds-PNA and a small amount of ss-PNA. The incubation temperature for ds-monolayer preparation was 27°C. Higher temperature incubation for the ds-monolayer preparation was avoided so that the duplex molecules would remain intact. Our previous ss-T-PNA study indicated that at this low temperature incubation ss-T-PNA forms a

significant amount of "lying-down" phase,[38] consequently cyclic voltammetry could show a weak signal for faster species. Because the amount of 'lying-down' phase was typically not present or occurred in small amounts, no effort was made to distinguish between these two possibilities.

Electrochemical Results for Different PNA molecules: The results of a voltammetry study of the ss Cys-T3-G-T3-Fc and Duplex Cys-(A-T)7-Fc SAMs are shown in Figure 5.2. As the CT event becomes slow with respect to the potential scan rate the voltammetric peak maxima shift. These voltammetric peak shifts were fit by the predicted shift from Marcus theory to determine the standard heterogeneous electron transfer rate constant. Panels A and C show three representative voltammograms for two different PNA SAMs. These voltammograms show that as the scan speed increases the voltammetric peak shifts, indicating that CT was slower than the scan speed of voltammetry. Panels B and D plot the dependence of the oxidation peak potential on the scan speed and compare it to the prediction of the Marcus theory model, in which the standard electrochemical rate constant k^0 was used as an adjustable parameter. Ferrocene's reorganization energy has been well characterized by several research groups, and it is reported to lie between 0.7 eV and 0.96 eV.[41] In this study, the ferrocene reorganization energy was taken as 0.8 eV.[57] A 25% change in its reorganization energy does not change the quality of fitting. The voltammograms and fitting curves of other PNA SAMs are shown in the supporting information.

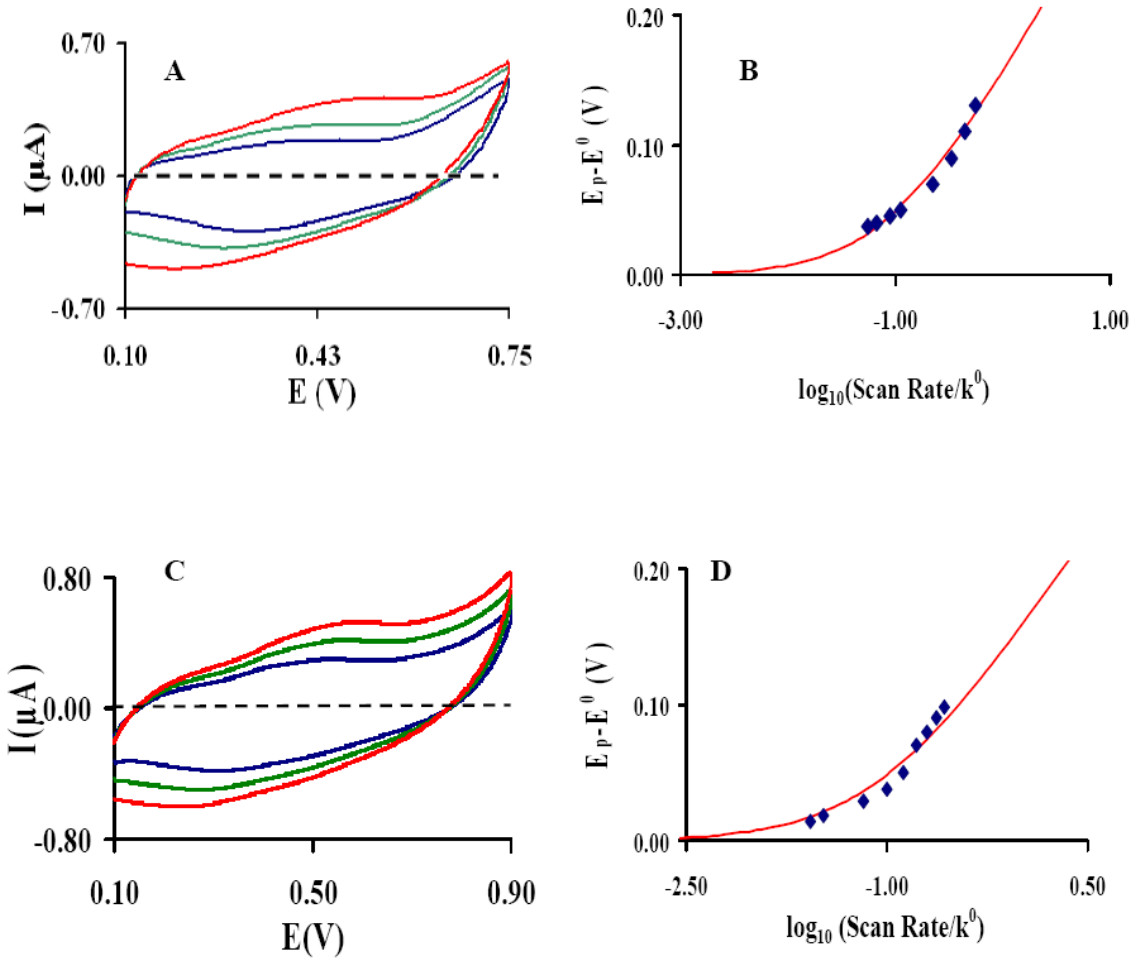

Figure 5.2 (A) and (C) Cyclic voltammograms are shown for Cys-T3-G-T3-Fc SAM at scan rates 6 mV/s (blue), 10 mV/s (green) and 20 mV/s (red) and for Duplex Cys-(A-T)7-Fc SAM at scan rates 20 mV/s (blue), 30 mV/s (green) and 40 mV/s (red). (B) and (D) Fitting curves are plotted for the determination of CT rate of Cys-T3-G-T3-Fc and Duplex Cys (A-T)7-Fc SAMs. The diamond symbols represent the experimentally determined points and the solid line represents the best fit theoretical curve.

The CT rate constants for five different ss-PNA and four different ds-PNA molecules are reported in Table 5.2. In the case of ss-PNA molecules, Cys-T3-G-T3-Fc and Cys-T3-A-T3-Fc have k^0's that are four times and two times faster than that of Cys-T7-Fc respectively; in contrast the Cys-T3-Bk-T3-Fc was more than three times slower. The CT rate constant of Cys-T3-C-T3-

Table 5.2 Charge Transfer Rate Constants and Electrochemical Coverage's for ss-PNA and ds-PNA SAMs.

Molecule	k^0 (s^{-1})	Coverage ($pmol/cm^2$)	No of Trials
Cys-T3-Bk-T3-Fc	< 0.005	~100	5
Cys-T3-C-T3-Fc	0.014 ± 0.003	91 ± 28	6
Cys-T3-T-T3-Fc	0.018 ± 0.002	83 ± 13	4
Cys-T3-A-T3-Fc	0.041 ± 0.010	96 ± 28	4
Cys-T3-G-T3-Fc	0.076 ± 0.013	87 ± 26	5
Cys-T3-T-T3-Fc A3-A-A3-Lys	0.25 ± 0.05	109 ± 38	11
Cys-T3-A-T3-Fc A3-T-A3-Lys	0.32 ± 0.06	68 ± 45	5
Cys-T3-C-T3-Fc A3-G-A3-Lys	0.67 ± 0.16	74 ± 21	7
Cys-T3-G-T3-Fc A3-C-A3-Lys	0.59 ± 0.13	115 ± 49	6

Fc was comparable to Cys-T7-Fc, albeit slightly smaller. Comparison of Cys-T3-G-T3-Fc and Cys-T3-Bk-T3-Fc reveals a more than fifteen-fold difference in k^0.

For ds-PNA SAMs, the k^0 rate constants are an order of magnitude faster than the single-stranded cases. The CT rate constants were approximately two times higher when the fourth base pairs were G-C rather than A-T. Interestingly, the results in Table 5.2 show that the CT rate constants were not altered significantly by altering the fourth base pair sequence from T-A to A-T or from C-G to G-C, *i.e.* interstrand nucleobase switching.

Computational Results for ss-PNA: The conductance for the ensemble of 500 T-X-T structures was found to show a skewed distribution where the maximum conductance observed was about two orders of magnitude higher than the average values while the minimum conductance was several orders of magnitude lower than the average values. Table 5.3 reports the mean, median and maximum conductance values that were obtained for each system. The trends are similar for the three measures. In agreement with the experimental trends, the purine (X=G,A) substituted systems show much higher conductances than the pyrimidine (X= C,T) substituted systems.

Table 5.3 Comparison of calculated conductances with experimental charge transfer rates for the four T3-X-T3 systems

Molecule	k^0 (s^{-1}) measured	Average Conductance		Max Conductance ($10^{-10}\ \Omega^{-1}$)
		Mean ($10^{-12}\ \Omega^{-1}$)	Median ($10^{-12}\ \Omega^{-1}$)	
Cys-T3-C-T3-Fc	0.014 ± 0.003	0.77	0.30	0.11
Cys-T3-T-T3-Fc	0.018 ± 0.002	0.42	0.28	0.04
Cys-T3-A-T3-Fc	0.041 ± 0.010	4.25	1.66	0.59
Cys-T3-G-T3-Fc	0.076 ± 0.013	5.91	3.08	1.10

If the coupling of the molecule to the electrode and the ferrocene is perturbative, as assumed in the calculations, then a linear relationship between the conductance (near zero bias) and the charge transfer rate can be derived for coherent charge transfer via the superexchange mechanism[58]. Figure 5.3 shows plots of the charge transfer rate vs. conductance for each of the four systems along with linear best fits to the data. For each of the three calculated conductance measures good correlations are evident, demonstrating that the calculations reproduce the experimental trends.

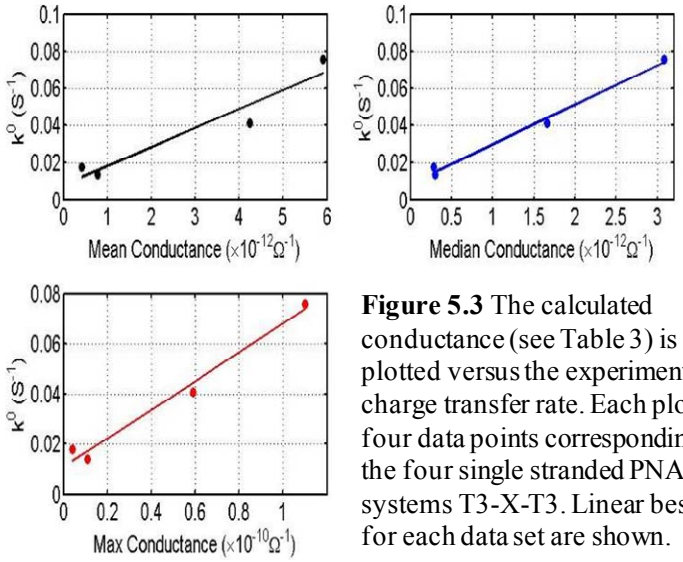

Figure 5.3 The calculated conductance (see Table 3) is plotted versus the experimental charge transfer rate. Each plot has four data points corresponding to the four single stranded PNA systems T3-X-T3. Linear best fits for each data set are shown.

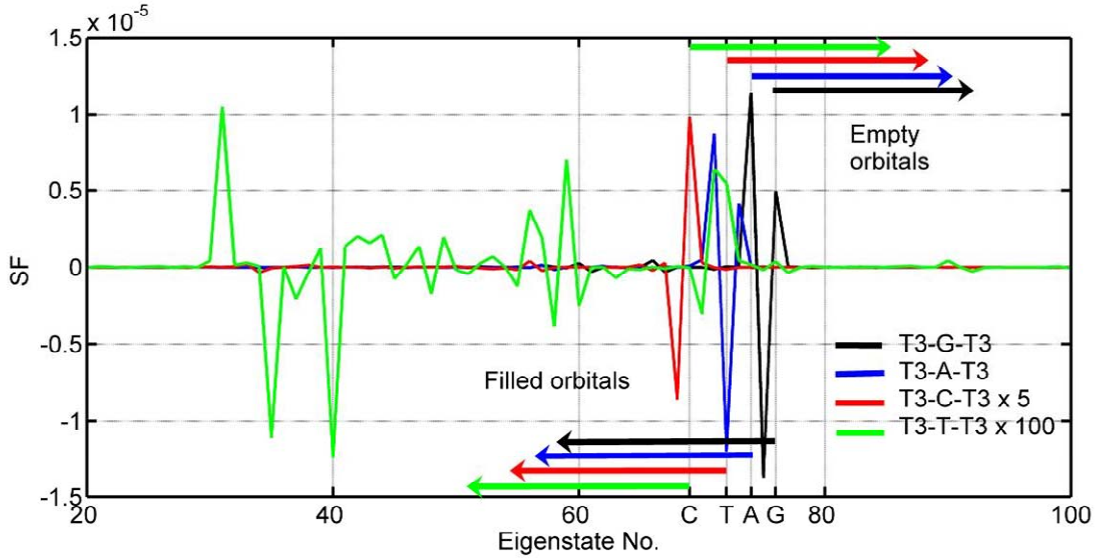

Figure 5.4 Plots of the scoring function (Eqn 5.2) for each molecular orbital. The data correspond to maximum conductance structures for the four T-X-T systems. The relative trends are similar for the average and minimum conductance structures.

The correlation between the HOMO energy of the nucleobase X and the conductance was also investigated. The results show that the average HOMO energy is strongly correlated with the trends in conductance for the four systems (correlation coeff = 0.99). Within each system the correlation between these variables is quite weak,

however. Preliminary investigations suggest that this affect results from variations in the coupling strengths that result from fluctuations in the local geometries of the base pairs. These findings will be reported on elsewhere[59].

Further evidence for the dependence of conduction on the interaction between the nucleobases comes from an analysis of the geometries and molecular orbitals for the MD structures which showed maximum, minimum and average conductance values for each of the four T-X-T systems. In all the four subsystems the structures with minimum conductance showed structural deformations which disrupted the stacking interactions of the central base with one of the neighboring T bases, whereas the maximum and average conduction structures show better stacking geometries, with the former showing the closest interbase distance. The contributions of molecular orbitals (filled and empty) to the conductance was defined by using the scoring function defined in Eqn 5.2. Figure 5.4 shows a plot of each molecular orbital's contribution to the conduction for maximum conductance structures for the four T-X-T systems. For all four systems the strongest contributions come from the filled states, *i.e.* hole transfer dominates. This result is expected because the Fermi level (or tunneling energy) lies closer to the filled molecular states than the empty states. The contribution of each orbital can be positive or negative depending on the sign of its couplings to other molecular orbitals introduced due to interactions with contacts at both. For all cases the frontier orbitals HOMO, HOMO-1 and HOMO-2 contribute significantly. Except for the T3-T-T3 case the contribution of the frontier orbitals is more than an order of magnitude larger than from the rest. A visualization of the frontier orbitals reveals that the HOMO, HOMO-1 and HOMO-2 orbitals are highly localized on each of three bases. In all systems except T-T-T the

HOMO invariably sits on the central base X=G,A,C. with the HOMO-1 and HOMO-2 lying on the terminal Ts. For T-T-T the HOMO, HOMO-1, and HOMO-2 lie on the top, central and bottom Ts respectively. For all systems the orbitals which lie further below and show significant contributions are delocalized with the strongest contributions coming from the most delocalized cases. Such contributions dominate in the T-T-T system where the degree of delocalization is rather high.

5.5 Discussion

The findings described above indicate that the nucleobases play an important role in determining the charge transfer rate through the PNA SAMs. For the ss-PNA SAMs, the k^0 values range from 0.014 s^{-1} to 0.067 s^{-1}, revealing a dependence on the nucleobase identity. The trend in the rate constants for the different single stranded molecules correlates with the oxidation potential of the nucleobase, as reported by Seidel et al.;[60] hence G has the highest rate and the nucleobases C and T have the lowest rates. In order to further confirm the role of nucleobases, Cys-T3-Bk-T3-Fc, in which the fourth residue does not have a nucleobase, was studied. The CT rate constant of Cys-T3-Bk-T3-Fc was much slower than the other PNA oligomers. Although it was too slow to be measured accurately; its rate was less than 0.005 s^{-1}. The importance of the nucleobases in determining the charge transfer rate constant is evident from the duplex PNA molecule studies also. The CT rate constant of the duplex Cys-(T-A)7-Fc was fourteen times higher than the Cys-T7-Fc, and the rate constant increased by another factor of two when the fourth base pair of the duplex was replaced by a G-C base pair. This factor of two is consistent with the increase observed between ss-oligomers of Cys-T3-A-T3-Fc and Cys-T3-G-T3-Fc. Interestingly the CT rates do not change significantly upon switching the

nucleobases between the two strands. To better quantify and understand the dependence of the rate constant on the nucleobase we use a nonadiabatic picture for the electron transfer.

In the nonadiabatic limit, the CT rate is given by the Fermi Golden Rule expression,[57,61-70]

$$k^0 = \frac{2\pi}{\hbar}|V|^2 \, FCWDS \tag{5.3}$$

where FCWDS is Franck-Condon weighted density of state, which accounts for the effect of nuclear coordinates on the rate constant. When the Gibbs energy (ΔG) is smaller than the reorganization energy (λ) and the high-frequency vibrational modes of the donor and acceptor are not a significant part of the reorganization, the FCWDS may be written as

$$FCWDS = \frac{1}{\sqrt{4\pi\lambda k_B T}} \exp\left[-\frac{(\lambda + \Delta G)^2}{4\lambda k_B T} \right] \tag{5.4}$$

The reorganization energy, λ, consists of two components: an inner sphere contribution that is associated with the internal coordinates of the redox species, λ_{in}, and an outer sphere component, λ_{out}, which is dominated by the solvent polarization. For ferrocene/ ferrocenium redox couple, a frequently used approximation is to consider only the dominant λ_{out} term.

For charge transfer at an electrode, a range of electronic states in the solid are available. At a particular electronic energy ε in the electrode, the Gibbs energy of reaction is given by

$$\Delta G = (\varepsilon_F - \varepsilon) + e\eta \tag{5.5}$$

where η is the overpotential and ε_F is the Fermi level of the electrode. Substitution of eq 5.5 into eq 5.4 generates an expression of FCWDS at this energy. To obtain an expression

for the rate constant one must integrate over all the available energy state. For the case of reduction, one finds

$$k_{\mathrm{Re}d} = \frac{2\pi}{\hbar}|V|^2 \frac{1}{\sqrt{4\pi\lambda k_B T}} \int_{-\infty}^{\infty} \rho(\varepsilon) \times \exp\left[-\frac{(\lambda + (\varepsilon_F - \varepsilon) + e\eta)^2}{4\lambda k_B T} \right] f(\varepsilon) d\varepsilon \tag{5.6}$$

where ρ(ε) in the density of electronic states of the electrode and f(ε) is the Fermi-Dirac distribution law which is given by eq. 5.7

$$f(\varepsilon) = \frac{1}{1 + \exp[(\varepsilon - \varepsilon_F)/k_B T}} \tag{5.7}$$

In the present study, overpotential (η)=0, and eq. 5.6 can be expressed as

$$k_{\mathrm{Re}d} = \frac{2\pi}{\hbar}|V|^2 \frac{1}{\sqrt{4\pi\lambda k_B T}} \int_{-\infty}^{\infty} \rho(\varepsilon) \times \exp\left[-\frac{(\lambda + (\varepsilon_F - \varepsilon))^2}{4\lambda k_B T} \right] f(\varepsilon) d\varepsilon \tag{5.8}$$

The present study, the different systems discussed here have the same ferrocene reorganization energy (λ), ε_F, and ρ(ε). Hence, the different systems will have the same FCWDS, but will differ because of changes in the electronic coupling $|V|$ along the PNA strand.

A McConnell-like Picture: For the superexchange mechanism,[71] the initial and final diabatic states mix by virtue of their interactions with higher energy electronic configurations, e.g., obtained by promotion of an electron (hole) from the donor (acceptor) to an empty (filled) orbital of the intervening molecules. For the case of identical mediating sites and only nearest neighbor interactions, the electronic coupling $|V|$ is given by

$$V = \left(\frac{h_{DB} h_{BA}}{\Delta} \right) \left(\frac{h}{\Delta} \right)^{N-1} \tag{5.9}$$

where h_{DB} (h_{BA}) is the interaction energy between the donor (acceptor) and the terminal superexchange orbital of the intervening structure, Δ is the energy difference between the diabatic transition state and the superexchange configurations involving the promoted electron (hole), and h is the exchange coupling between the N adjacent bridge sites. For the current situation in which a single site in the center of the oligonucleotide strand differs, the expression for $|V|$ becomes

$$V = \left(\frac{h_{FcT} h_{TAu}}{\Delta_T^2} \right) \left(\frac{h_{TT}}{\Delta_T} \right)^4 \left(\frac{h_{TX} h_{XT}}{\Delta_X} \right) \tag{5.10}$$

where h_{TAu} and h_{FcT} are the exchange couplings between the gold-cysteine and the thymine-ferrocene respectively. The thymine-thymine (AT-AT) coupling is h_{TT} and the unique base couplings are h_{TX}. The energy differences Δ_T and Δ_X are the energy differences between the tunneling energy and the thymine (AT) and fourth nucleobase (fourth base pairs) superexchange states, respectively. Because this study only varies the fourth residue, we postulate that only h_{TX} and Δ_X are different for the different systems.

In the simplest approximation, we assume that h_{TX} does not vary significantly with the nature of the fourth base and that any changes result from a shift in the energy. Because |V| is proportional to $1/\Delta_X$, the rate constant is proportional to $(1/\Delta_X)^2$, and a plot of k^0 versus $(1/\Delta_X)^2$ should be linear. To estimate Δ_X, the oxidation potential of the different nucleobases are taken from the report of Seidel et al.[60] Assuming CT in ss PNA is hole mediated charge transfer and the oxidation potential for the nucleobases in DNA and PNA are the same; Δ_X for G, A, T, C will be 0.8, 1.27, 1.42 and 1.45 eV respectively.

Figure 5.5 plots the charge transfer rate constant versus $(1/\Delta_X)^2$ for the different systems. Panel A illustrates how the energy gap to the unique base (fourth base) changes

through the series. Panel B shows plots of the rate constants for the single stranded (left axis) and the duplexes (right axis) as a function of one over the energy gap squared. The rate constants k^0_{ss} for the single-stranded oligomers are the blue diamond symbols and a best fit line is drawn in blue. The plot show that the CT rate constant decreases, as the energy difference between fourth nucleobase and the tunneling energy increases, which is consistent with a superexchange mechanism.

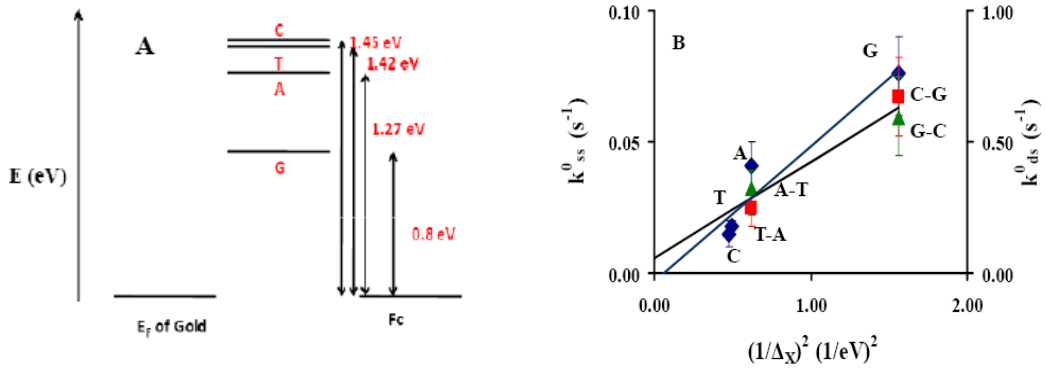

Figure 5.5 (A) Tunneling barrier/ oxidation potential of different bases with respect to ferrocene. (B) Charge transfer rate of the different PNA molecules are plotted versus $(1/\Delta_X)^2$. Blue diamond symbols represent experimentally determined points for ss-PNA SAMs and the blue straight line is the best fit straight line between the experimentally determined results. The red square and green triangle symbols represent experimentally determined points for ds-PNA SAMs and the black straight line represents a best fit straight line between experimentally determined results.

For the duplexes, the rate constants are more than ten times higher than the corresponding single stranded PNA SAMs (note the change in scale for the ordinates in Figure 5.5). The rate constants k^0_{ds} for the ds-PNA SAMs are represented by the red squares and green triangles. The green triangles are the duplexes in which the ferrocene is covalently tethered to the same strand as the nucleobase with the lowest oxidation potential, and the red squares are the duplexes in which the ferrocene is covalently tethered to the complimentary strand of the nucleobase with the lowest oxidation

potential. Little difference exists for the rate constants in the two cases. The analysis assumes that the lowest oxidation potential of the two nucleobases in the base pair is the relevant one to consider; the opposite assumption leads to a very poor correlation of the rate constant with the oxidation potential. The black line shows a best fit to these data. The good linear correlation is consistent with a superexchange mechanism; however the much higher rates for the duplexes suggest that the coupling between base pairs for ds-PNA SAMs must be better than that for ss-PNA SAMs.

Computational results for ss-PNA: The calculations of conductance for the four ss-PNA systems: T3-X-T3 (X=G,A,C,T) correlate well with the trends in experimentally measured charge transfer rates. We find that the trend in the energy of the molecular HOMO correlates well with the average conductance value for the four systems, however the couplings between base pairs plays an important role and their values can be linked to thermal fluctuations of the interbase geometry. In addition, the analysis shows that the conductance is dominated by contributions from filled orbitals, i.e. by hole transport. The frontier orbitals in particular give contributions which are orders of magnitude higher than the rest for the X=G,A,C systems. A visualization of MOs shows that the frontier orbitals are highly localized on single bases. Contributions from orbitals further away from the Fermi energy can be significant if they are delocalized.

The conductance (g) and charge transfer rate (k^0) can be related by eq 11.[58]

$$g \approx \frac{8e^2}{\pi^2 \Gamma_D^{(L)} \Gamma_A^{(R)} FCWDS} k^0 \qquad (5.11)$$

where FCWDS is given by eq. 5.4. In Figure 5.3, the computed mean conductance values are plotted against experimentally observed charge transfer rates for ss-PNA SAMs. From the slope of the conductance versus charge transfer rate plot, the broadening matrix

(Γ) can be calculated. Ferrocene reorganization energy is taken as 0.8 eV[38,57] and assuming ΔG=0, Γ value is estimated to be 0.133 eV. This Γ value is very consistent with the assumption made in the theoretical calculations.

5.6 Conclusions

In this work, 7-mer ss PNAs and ds-PNAs were self-assembled on a gold electrode. The fourth residues of the 7-mer PNA oligomers were varied to investigate the CT mechanism. The CT rate of ss-PNA and ds-PNA oligomers were found to be base sequence dependent. For the ds-PNA oligomers switching of the nucleobases between strands had little impact on the CT rates. It is important to distinguish the current finding from earlier reports that the stacked DNA bases form a "л-way" for rapid radical cation migration.[72] Our studies do not show that the ss-PNA is a molecular wire, rather our previous study of short chain ss-T-PNA showed that the CT rate exponentially decayed with increasing number of nucleobases.[38] In this study, the CT through the PNA molecule which does not have one nucleobase (Cys-T3-Bk-T3-Fc) did not stop, but its transfer rate became very slow. Computational studies show that the electron transfer proceeds through hole mediated coupling between base pairs and this finding supports the observed correlation between the electron transfer rate constant and the oxidation potential of the base at site four. These findings clearly indicate that the energy barrier through which charge tunnels is controlled by the nature of nucleobase or base pairs.

5.7 Acknowledgements

We acknowledge support from the U.S National Science Foundation (CHE 0628169).

5.8 References and Notes:

(1) Schwartz, D. K. *Annu. Rev. Phys. Chem.* **2001**, *52*, 107-137.

(2) Ulman, A. *Chem. Rev.* **1996**, *96*, 1533-1554.

(3) Jortner, J.; Ratner, M. A. *Molecular Electronics;* Blackwell: London. 1997.

(4) Kumar, A.; Biebuyck, H. A.; Whitesides, G. M. *Langmuir* **1994**, *10*, 1498-1511.

(5) Revell, D. J.; Knight, J. R.; Blyth, D. J.; Haines, A. H.; Russell, D. A. *Langmuir* **1998**, *14*, 4517-4524.

(6) Bain, C. D.; Evans, S. D. *Chem. Br.* **1995**, *31*, 46.

(7) Donhauser, Z. J.; Mantooth, B. A.; Kelly, K. F.; Bumm, L. A.; Monnell, J. D.; Stapleton, J. J.; Jr, D. W. P.; Rawlett, A. M.; Allara, D. L.; Tour, J. M.; Weiss, P. S. *Science* **2001**, *292*, 2303-2307.

(8) Prime, K. L.; Whitesides, G. M. *Science* **1991**, *252*, 1164-1167.

(9) Degama, A. A. S. *Theor. Chim. Acta.* **1985**, *68*, 159.

(10) Evenson, J. W.; Karplus, M. *Science* **1993**, *262*, 1247-1249.

(11) Gehlen, J. N.; Daizadeh, I.; Stuchebrukhov, A. A.; Marcus, R. A. *Inorg. Chim. Acta* **1996**, *243*, 271-282.

(12) Goldman, C. *Phys. Rev. A* **1991**, *43*, 4500.

(13) Harden, M. M. *J. Chem. Phys.* **1961**, *35*, 508-515.

(14) Joachim, C.; Ratner, M. A. *Nanotechnology* **2004**, *15*, 1065.

(15) Magoga, M.; Joachim, C. *Phys. Rev. B* **1997**, *56*, 4722.

(16) Priyadarshy, S.; Risser, S. M.; Beratan, D. N. *J. Phys. Chem.* **1996**, *100*, 17678-17682.

(17) Ratner, M. A. *J. Phys. Chem.* **1990**, *94*, 4877-4883.

(18) Reimers, J. R.; Hush, N. S. *J. Photochem. Photobiol. A* **1994**, *82*, 31-46.

(19) Remacle, F.; Levine, R. D. *J. Phys. Chem. B* **2001**, *105*, 2153-2162.

(20) Berlin, Y. A.; Burin, A. L.; Ratner, M. A. *Chem. Phys.* **2002**, *275*, 61-74.

(21) Berlin, Y. A.; Hutchison, G. R.; Rempala, P.; Ratner, M. A.; Michl, J. *J. Phys. Chem. A* **2003**, *107*, 3970-3980.

(22) Giese, B. *Annu. Rev. Biochem.* **2002**, *71*, 51-70.

(23) Jortner, J.; Bixon, M.; Langenbacher, T.; Michel-Beyerle, M. E. *Proc. Natl. Acad. Sci.* **1998**, *95*, 12759.

(24) Li, X. Q.; Zhang, H.; Yan, Y. *J. Phys. Chem. A* **2001**, *105*, 9563-9567.

(25) Schuster, G. B. *Long-Range Charge Transfer in DNA I*; Top. Curr. Chem. Vols 236 and 237; Springer: New York, 2004.

(26) Casero, E.; Darder, M.; Diaz, D. J.; Pariente, F.; Martin-Gago, J. A.; Abruna, H.; Lorenzo, E. *Langmuir* **2003**, *19*, 6230-6235.

(27) Herne, T. M.; Tarlov, M. J. *J. Am. Chem. Soc.* **1997**, *119*, 8916-8920.

(28) Zhang, R. Y.; Pang, D. W.; Zhang, Z. L.; Yan, J. W.; Yao, J. L.; Tian, Z. Q.; Mao, B. W.; Sun, S. G. *J. Phys. Chem. B* **2002**, *106*, 11233-11239.

(29) Hartwich, G.; Caruana, D. J.; de Lumley-Woodyear, T.; Wu, Y.; Campbell, C. N.; Heller, A. *J. Am. Chem. Soc.* **1999**, *121*, 10803-10812.

(30) Chahma, M.; Lee, J. S.; Kraatz, H.-B. *J. Electroanal. Chem.* **2004**, *567*, 283-287.

(31) Anne, A.; Demaille, C. *J. Am. Chem. Soc.* **2006**, *128*, 542-557.

(32) Egholm, M.; Buchardt, O.; Christensen, L.; Behrens, C.; Freier, S. M.; Driver, D. A.; Berg, R. H.; Kim, S. K.; Norden, B.; Nielsen, P. E. *Nature* **1993**, *365*, 566-568.

(33) Egholm, M.; Nielsen, P. E.; Buchardt, O.; Berg, R. H. *J. Am. Chem. Soc.* **1992**, *114*, 9677-9678.

(34) Petersson, B.; Nielsen, B. B.; Rasmussen, H.; Larsen, I. K.; Gajhede, M.; Nielsen, P. E.; Kastrup, J. S. *J. Am. Chem. Soc.* **2005**, *127*, 1424-1430.

(35) Rasmussen, H.; Kastrup, J. S.; Nielsen, J. N.; Nielsen, J. M.; Nielsen, P. E. *Nature Struct. Biol.* **1997**, *4*, 98-101.

(36) Rasmussen, H.; Liljefors, T.; Petersson, B.; Nielsen, P. E.; Kastrup, J. S. *J. Biomol. Struct. Dyn.* **2004**, *21*, 495-502.

(37) Wittung, P.; Eriksson, M.; Lyng, R.; Nielsen, P. E.; Norden, B. *J. Am. Chem. Soc.* **1995**, *117*, 10167-10173.

(38) Paul, A.; Watson, R. M.; Lund, P.; Xing, Y.; Burke, K.; He, Y.; Borguet, E.; Achim, C.; Waldeck, D. H. *J. Phys. Chem. C* **2008**, *112*, 7233-7240.

(39) Carter, M. T.; Rowe, G. K.; Richardson, J. N.; Tender, L. M.; Terrill, R. H.; Murray, R. W. *J. Am. Chem. Soc.* **1995**, *117*, 2896-2899.

(40) Slowinski, K.; Chamberlain, R. V.; Miller, C. J.; Majda, M. *J. Am. Chem. Soc.* **1997**, *119*, 11910-11919.

(41) Smalley, J. F.; Feldberg, S. W.; Chidsey, C. E. D.; Linford, M. R.; Newton, M. D.; Liu, Y.-P. *J. Phys. Chem.* **1995**, *99*, 13141-13149.

(42) Sumner, J. J.; Weber, K. S.; Hockett, L. A.; Creager, S. E. *J. Phys. Chem. B* **2000**, *104*, 7449-7454.

(43) Weber, K.; Hockett, L.; Creager, S. *J. Phys. Chem. B* **1997**, *101*, 8286-8291.

(44) Sek, S.; Sepiol, A.; Tolak, A.; Misicka, A.; Bilewicz, R. *J. Phys. Chem. B* **2004**, *108*, 8102-8105.

(45) Tao, N. *J. Mater. Chem.* **2005**, *15*, 3260 - 3263.

(46) Anderson, G. W.; McGregor, A. C. *J. Am. Chem. Soc.* **1957**, *79*, 6180-6183.

(47) McKay, F. C.; Albertson, N. F. *J. Am. Chem. Soc.* **1957**, *79*, 4686-4690.

(48) Nielsen, P. E. *Peptide Nucleic Acids: Protocols and Applications;* Horizon Bioscience: Wymondham UK, 2004.

(49) Sawyer, D. T.; Sobkowiak, A.; Roberts, J. L. *Experimental Electrochemistry for Chemists;* Wiley, New York, 1995.

(50) Azzam, R. M. A.; Bashara, N. M. *Ellipsometry and Polarized Light;* North- Holland publishing Co.: Amsterdam, 1977.

(51) Tompkins, H. G. *A User's Guide to Ellipsometry; Academic Press Inc: New York 1993.*

(52) Hatcher, E.; Balaeff, A.; Keinan, S.; Venkatramani, R.; Beratan, D. N. *J. Am. Chem. Soc.* **2008**, *130*, 11752-11761.

(53) Mehrez, H.; Anantram, M. P. *Phys. Rev. B* **2005**, *71*, 115405-5.

(54) Rösch, N.; Voityuk, A. A. In *Long-Range Charge Transfer in DNA II* 2004, p 37-72.

(55) Datta, S. *Quantum Transport: Atom to Transistor;* Cambridge, 2005.

(56) *The length of Cysteine, Ferrocene and each PNA base has been calculated by CAChe software. Geometry has been optimized by PM3 method.*

(57) Napper, A. M.; Liu, H.; Waldeck, D. H. *J. Phys. Chem. B* **2001**, *105*, 7699-7707.

(58) Nitzan, A. *J. Phys. Chem. A* **2001**, *105*, 2677-2679.

(59) Venkatramani, R.; Balaeff, A.; Paul, A.; Bezer, S.; Davis, K.; Watson, R. M.; Achim, C.; Waldeck, D. H.; Beratan, D. N., *Manuscript in preparation*.

(60) Seidel, C. A. M.; Schulz, A.; Sauer, M. H. M. *J. Phys. Chem.* **1996**, *100*, 5541-5553.

(61) Barbara, P. F.; Meyer, T. J.; Ratner, M. A. *J. Phys. Chem.* **1996**, *100*, 13148-13168.

(62) Bard, A. J.; Faulkner, L. R. *Electrochemical Methods; Fundamental and Applications;* Wiley: New York, 1980.

(63) Chidsey, C. E. D. *Science* **1991**, *251*, 919-922.

(64) Finklea, H. O. *In Electroanalytical Chemistry; Bard, A. J., Rubinstein, I., Eds.;* Marcel Dekker Inc.: New York, 1996, vol 19, p 109.

(65) Khoshtariya, D. E.; Dolidze, T. D.; Zusman, L. D.; Waldeck, D. H. *J. Phys. Chem. A* **2001**, *105*, 1818-1829.

(66) Marcus, R. A. *J. Chem. Phys.* **1956**, *24*, 966-978.

(67) Marcus, R. A. *J. Chem. Phys.* **1965**, *43*, 679-701.

(68) Miller, C. J. *Physical Electrochemistry: Principles, Methods and Applications.* Rubinstein, I, Ed.; Marcel Dekker Inc.: New York, 1995, p 27.

(69) Wei, J.; Liu, H.; Dick, A. R.; Yamamoto, H.; He, Y.; Waldeck, D. H. *J. Am. Chem. Soc.* **2002**, *124*, 9591-9599.

(70) Zimmt, M. B.; Waldeck, D. H. *J. Phys. Chem. A* **2003**, *107*, 3580-3597.

(71) McConnell, H. M. *J. Chem. Phys.* **1961**, *35*, 508-515.

(72) O'Neill, M. A.; Barton, J. K. *J. Am. Chem. Soc.* **2004**, *126*, 11471-11483.

5.9 Supporting Information

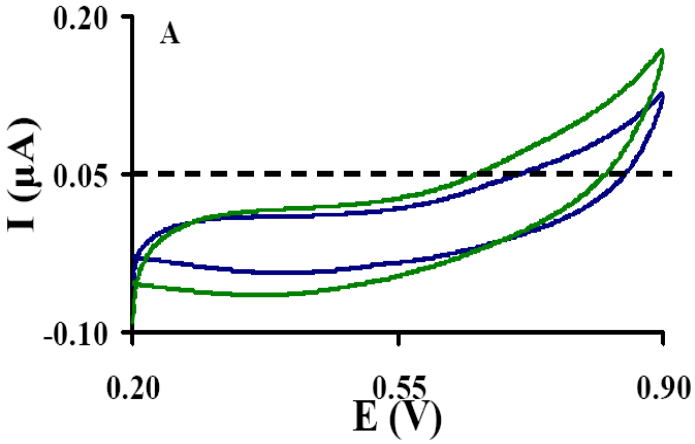

Figure 5.6 (A) Two cyclic voltammograms are shown for Cys-T3-Bk-T3-Fc SAM at scan rates 1 mV/s (Blue) and 2 mV/s (Green).

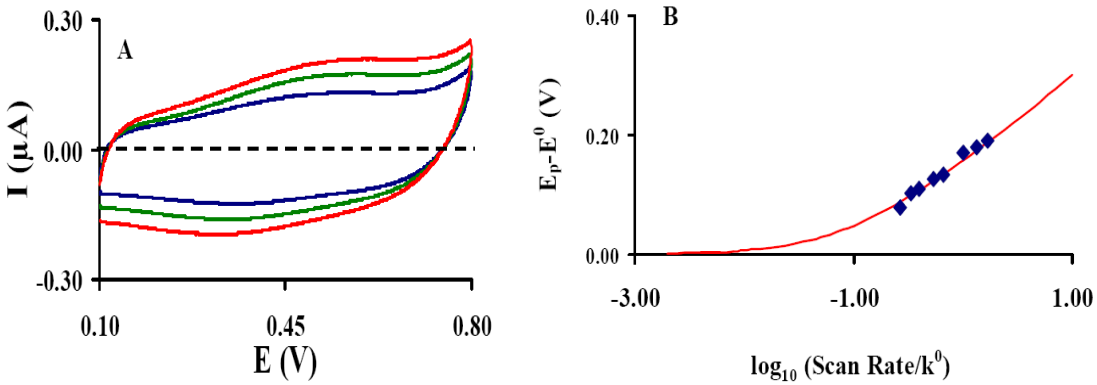

Figure 5.7 (A) Three cyclic voltammograms are shown for Cys-T3-C-T3-Fc SAM at scan rates 6 mV/s (Blue), 8 mV/s (Green) and 10 mV/s (Red). (B) A fitting Curve is plotted for the determination of electron transfer rate of Cys-T3-C-T3-Fc SAM.

Cyclic voltammograms and fitting curve for Cys-T7-Fc SAM are shown in Chapter 3 (Figure 3.13)

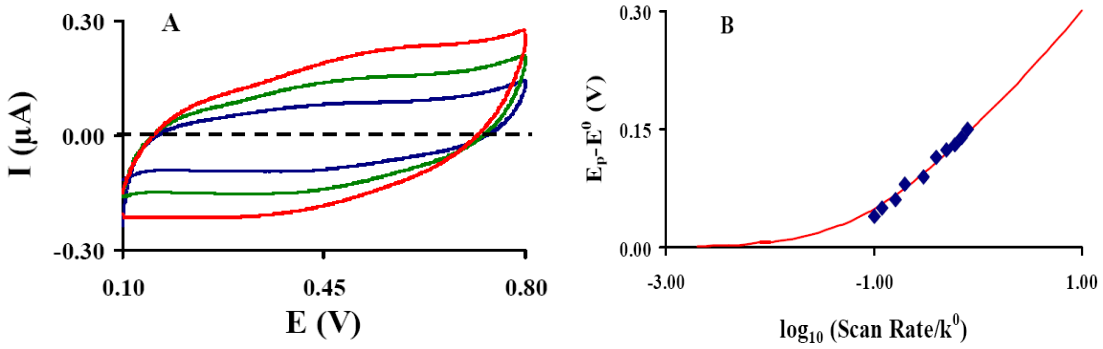

Figure 5.8 (A) Three cyclic voltammograms are shown for Cys-T3-A-T3-Fc SAM at scan rate 5 mV/s (Blue), 10 mV/s (Green) and 20 mV/s (Red). (B) A fitting Curve is plotted for the determination of electron transfer rate of Cys-T3-A-T3-Fc SAM.

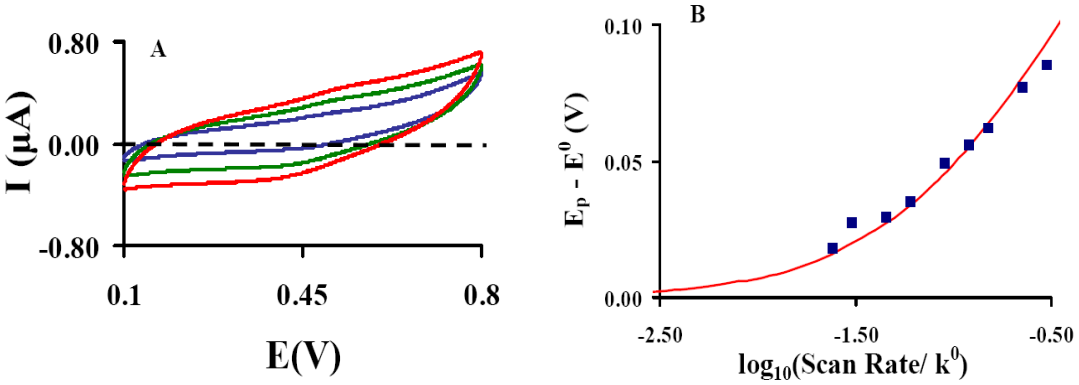

Figure 5.9 (A) Three cyclic voltammograms are shown for Duplex Cys-T3-A-T3-Fc:Lys-A3-T-A3 SAM at scan rate 10 mV/s (Blue), 20 mV/s (Green) and 30 mV/s (Red). (B) A fitting Curve is plotted for the determination of electron transfer rate of Duplex Cys-T3-A-T3-Fc:Lys-A3-T-A3 SAM.

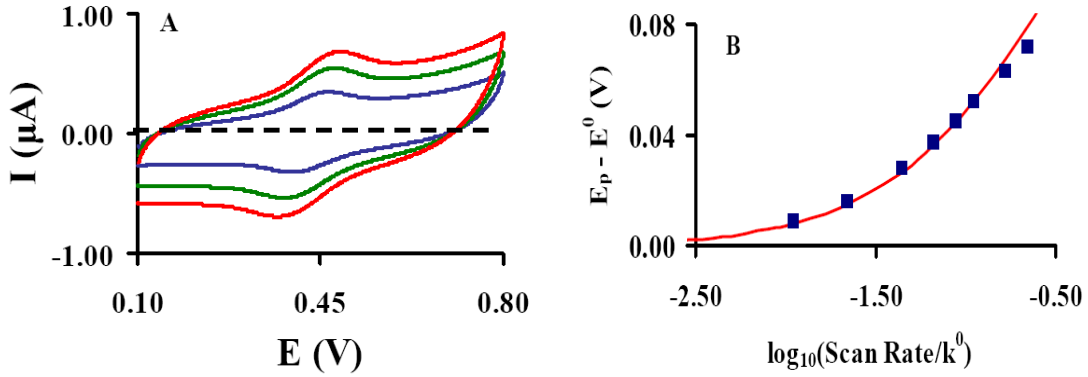

Figure 5.10 (A) Three cyclic voltammograms are shown for Duplex Cys-T3-G-T3-Fc:Lys-A3-C-A3 SAM at scan rate 10 mV/s (Blue), 20 mV/s (Green) and 30 mV/s (Red). (B) A fitting Curve is plotted for the determination of electron transfer rate of Duplex Cys-T3-G-T3-Fc:Lys-A3-C-A3 SAM.

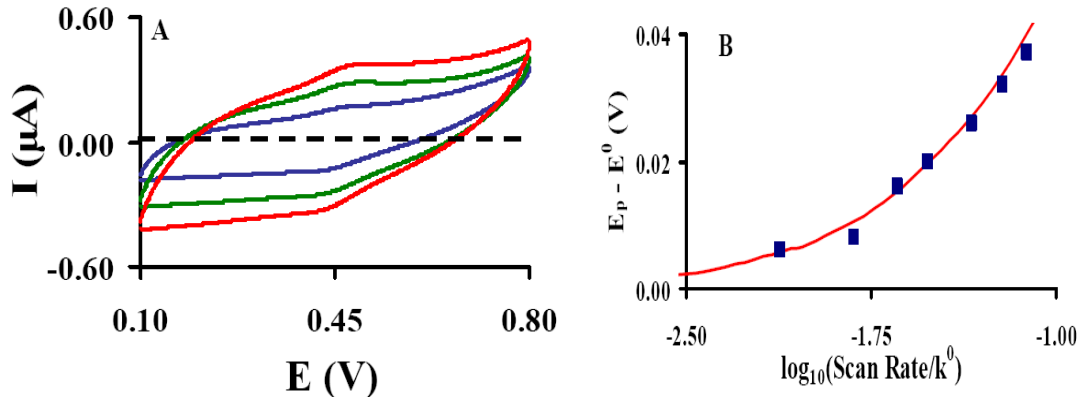

Figure 5.11: (A) Three cyclic voltammograms are shown for Duplex Cys-T3-C-T3-Fc:Lys-A3-G-A3 SAM at scan rate 10 mV/s (Blue), 20 mV/s (Green), and 30 mV/s (Red). (B) A fitting Curve is plotted for the determination of electron transfer rate of Duplex Cys-T3-C-T3-Fc:Lys-A3-G-A3 SAM.

Chapter 6 Conclusion

This thesis consists of two parts. The first part describes the work done on understanding the effect of molecular chirality on charge transfer (CT) in self-assembled scaffold monolayers (SAMs). The second part of the thesis investigated charge transfer through peptide nucleic acid (PNA) SAMs.

In chapter 2, a chiral scaffold molecule, having a porphyrin moiety was assembled on gold electrodes. The effect of molecular chirality has been studied by exciting the porphyrin using circular polarized light and measuring the photocurrent. The photocurrent displayed an asymmetry when the chiral monolayer was irradiated by left and right circular polarized light. The average asymmetry factor obtained for a right-handed monolayer was 0.004 ± 0.002 and that for a left-handed monolayer was -0.005 ± 0.001. Two mechanisms were proposed for the observed asymmetry. These two mechanisms are (1) electronic helicities of the excited porphyrins and (2) induced circular dichroism from the packing of the films. From a technological point of view, this study indicates that chiral selectivity can be used as a new control parameter for current devices.

Chapter 3, 4, and 5 discuss CT through PNA SAMs. In chapter 3, the distance dependent CT through short chain single stranded thymine containing PNA molecules (Cys-(T)n-Fc) has been studied by preparing PNA SAMs on gold electrodes. The distance was varied by changing the number of thymine nucleobases. The study showed that the monolayer consists of two different populations, namely a fast "lying-down" phase in which CT occur through space between the gold electrode and the redox probe and a second slow "standing-up" phase in which CT occur through PNA oligomers. The

redox active moiety of fast "lying-down" phase was chemically destroyed by reacting it with Cl^-. The CT rate of the "standing-up" phase decreased exponentially with increasing distance which is consistent with super-exchange mediated tunneling mechanism. The decay constant (β) was found to be 0.86 ± 0.04 $Å^{-1}$. This value is similar to that obtained for alkanethiol or peptides.

In chapter 4, three different types of PNA SAMs were studied on gold electrodes. The three types of molecules were single stranded thymine containing PNA (ss-Cys-(T)n-Fc), single stranded adenine containing PNA (ss-Cys-(A)n-Fc), and double stranded adenine-thymine containing PNA (ds-Cys-(A-T)n-Fc). It was observed that for short chain molecules, the CT rate decreased exponentially with distance, but at longer distance the distance dependence become very weak (≤ 0.1 $Å^{-1}$). This weak decay at long distance is attributed to CT mechanism switchover from tunneling to "hopping". The experimental transition point between these two mechanisms is found to be in good agreement with Tight-Binding model proposed earlier.

Chapter 5 discusses the role of nucleobase on the CT through PNA SAMs. SAMs of seven nucleobases or base pairs containing single stranded and double stranded PNA molecules were studied on gold electrodes. The fourth nucleotides were varied with all possible combinations. This study demonstrated that CT through PNA is base sequence dependent although the CT rate through ds-PNA had no impact upon switching nucleobases between strands. This study also showed that by changing only the fourth nucleobase, the CT rate of PNA can be varied by more than 100 times.

In summary this thesis finds three important conclusions regarding the flow of charge through PNA and organic scaffold monolayers which can be used further for

technological development. First of all, chirality is an important property that can be used to control the flow of charge. Second, the CT rate of PNA decreased exponentially with increasing distance for short chain oligomers but the distance dependence becomes weak at longer distance. This observation indicates that CT at shorter distance follows super-exchange mediated tunneling mechanism and at longer distance CT follows a "hopping" mechanism. Third, the nucleobase sequence primarily determines the CT rate through PNA molecules and the nucleobase sequence can be used to manipulate the flow of charge through the molecular bridge.